



Structural and Optical Characterization of ZnSe-based Microdisk Resonators

Vom Fachbereich Physik / Elektrotechnik der Universität Bremen
zur Erlangung des akademischen Grades Doktor der Naturwissenschaften (Dr. rer. nat.)
genehmigte Dissertation

von
Wilken Seemann

Erstgutachter: Prof. Dr. Jürgen Gutowski

Zweitgutachter: PD Dr. Alexander Pawlis

Datum der Abgabe: 01.12.2021

**Datum des
Promotionskolloquiums:** 21.12.2021

Abstract

Microdisk resonators offer small mode volumes due to their size. This is paired with strong containment of light in whispering gallery modes by total internal reflection at the disk edge. Therefore, they are commonly investigated as platforms for low-threshold lasing emission. Additionally, microdisks can be applied in technologies like quantum cryptography and quantum computing, as they have been shown to support single-photon emission, and spins embedded in them might be used as qubit storage. In all these applications, it is advantageous that the disks can be integrated into chip structures, e.g., for photonic circuitry.

The improvement of resonator quality, i.e., the minimization of losses reducing the intensity of propagating modes, is an important factor determining the device performance. For this purpose, the roughness of the microdisk edge is a central element, as modes propagate near the edge of the disk and are contained by total internal reflection at this boundary. In this thesis, microdisks containing a quantum well/barrier structure from II-VI semiconductors are analyzed. The resonators are fabricated in two different geometries: Free-standing microdisks that are partly under-etched, and supported microdisks that are in contact with the substrate over their whole bottom facet.

Stimulated emission into whispering gallery modes is observed in free-standing microdisks with different diameters between 2.8 and 3.8 μm . The optical quality and the edge roughness of the same microdisk are correlated to show the influence of imperfect boundaries on the modes propagating in the resonator. The optical quality of the resonators is assessed based on the quality factor of the modes observed in micro-photoluminescence measurements. For the evaluation of the edge roughness, their deformation function $r(\varphi)$ is extracted from scanning electron microscopy images in a process developed in this thesis. Theoretical calculations of resonances in the deformed microdisks, based on the boundary element method and using the deformation functions as input, confirm the experimental results. Both, the use of experimentally obtained deformation functions in theoretical calculations and the correlation of a structural and optical characterization of the same microdisk, have not been reported before.

In order to reduce the degradation of the mode intensity under continuous excitation that is observed in free-standing microdisks, supported resonators with a large range of diameters (from 1.0 up to 5.0 μm) are fabricated using a technique that is new to the II-VI material system. The resulting microdisks show an improved structural quality. Whispering gallery resonances can be observed on their deep-level emission band. This serves as a proof of principle that microresonators fabricated with this technique satisfy the prerequisites for applications in lasing and the quantum technologies mentioned above.

Contents

1	Introduction	1
2	Background	5
2.1	II-VI Semiconductors	5
2.1.1	Crystal Structure and Growth	5
2.1.2	Band Structure and Light Emission	6
2.2	Microdisk Resonators and Whispering Gallery Modes	9
2.2.1	Semiconductor Heterostructures	9
2.2.2	Optical (Micro-)Resonators	10
2.2.3	Total Internal Reflection	12
2.2.4	Whispering Gallery Mode Resonators	13
2.3	Theoretical Calculation of Resonances in Microdisk Resonators	15
2.3.1	Finite-Difference Time-Domain Method	15
2.3.2	Boundary-Element Method	18
3	State of the Art	19
3.1	Applications of ZnSe-based Epitaxial Semiconductor Structures	19
3.2	Microdisk Resonators	20
3.2.1	ZnSe-based Microdisk Resonators	20
3.2.2	Semiconductor Microdisk Resonators Based on other Materials	22
3.2.3	Theoretical Analysis of non-ideal Microdisk Resonators and the Role of Edge Roughness	25
4	Experimental Methods	29
4.1	Growth and Processing of Microdisks	29
4.2	Structural characterization using Scanning Electron Microscopy	31
4.2.1	Operational Principles of the SEM	32
4.2.2	Extraction of deformation functions from SEM images	33
4.3	Micro-Photoluminescence Measurements	38
4.4	FDTD simulations using <i>Meep</i>	40
5	Results and Discussion	43
5.1	Free-standing Microdisk Resonators	43
5.1.1	Experimental Observation of Stimulated Emission into Whispering Gallery Modes	43
5.1.2	Theoretical Confirmation	50
5.1.3	Deformation of the Resonators	54
5.2	Free-standing Microdisk Resonators with δ -type Halogen Impurities	57
5.2.1	Modes under Optical Excitation	57
5.2.2	Degradation of Mode Intensity under Continuous Excitation	69
5.3	Supported Microdisk Resonators with δ -type Halogen Impurities	72
5.3.1	Advantages and Drawbacks of the Supported Geometry	72
5.3.2	Near Band Edge Emission at Low Temperatures	73
5.3.3	Defect Emission Whispering Gallery Modes at Room Temperature	94
5.3.4	Deformation of the Resonators	99

6 Conclusion and Outlook	103
A References	107
B List of Publications	121
C Acknowledgements	123
D Curriculum Vitae	125

1. Introduction

II-VI semiconductors are commonly analyzed as emitters in the blue-green spectral range due to their large bandgap energies. Moreover, they exhibit large oscillator strengths and exciton binding energies and can be grown on commercially available GaAs substrates. Research on these materials led to the development of ZnSe-based LEDs [1]. The first semiconductor laser diode with blue-green emission has been presented in 1991 [2]. However, such emitters often suffered from degradation when in operation, as nonradiative recombination heats the structure, causing the formation and growth of dislocations, which in turn increase the fraction of nonradiative recombination. This effect limits the device lifetime to a maximum of a few hundred hours [3].

Today, lasing semiconductor structures are commercially available across the whole spectral range, the short-wavelength region is usually covered by III-nitride semiconductors [4]. Given these developments, research interest on ZnSe-based emitters has shifted towards effects like strong light-matter interaction [5], single photon emission and their entanglement, which can be employed for secure communication in quantum cryptography [6] or quantum information processing [7].

A basic building block for the realization and analysis of such effects are microcavities, which are used to trap light on a small scale. They can - for example - provide the containment needed to reach the strong-coupling regime between the cavity photons and the excitation of the active region [8]. This is defined by the observation that a distinction between the excitons and photons is not possible, quasi-particles called polaritons arise. In the weak-coupling regime, microcavities can enhance or suppress the emission from the active region in dependence on its wavelength, this is known as the Purcell effect [9]. Furthermore, such resonators can be used to amplify nonlinear optical processes, including second-harmonic generation or parametric down-conversion of photons [10, 11].

Microcavities can be fabricated based on distributed Bragg reflectors that provide high reflectivity and therefore enable the creation of resonators with small dimensions and cavity volumes [12]. Similarly, high reflectivities for wavelengths in a small interval can be realized by a periodic variation of the refractive index in photonic crystals [13].

In comparison to those cavities, microdisks, i.e., disks with a diameter in the order of a few micrometers, are easy to fabricate. Light can travel continuously along the border of these structures in so-called whispering gallery modes (WGMs), which is why microdisks are described as traveling-wave resonators. The photons are contained by total internal reflection; the small dimension of the microdisk results in low mode volumes. Additionally, microdisk resonators offer in-plane emission, which is usually parallel to the surface of the substrate. This is useful for the integration of the resonators into chip structures.

ZnSe-based microdisks have been reported to support low-threshold lasing [14] and single-photon emission [15]. Furthermore, a system employing the spin of a single atom bound to a fluorine donor in a ZnSe-based microdisk was shown to be a promising candidate for the storage of qubits [16].

The containment of light in microdisks strongly relies on their smooth edges, as roughness can cause scattering of the propagating waves outside the resonator and disturb the total internal reflection. This is observable in experiments when the optical properties of samples grown and structured by different fabrication techniques - resulting in different roughnesses - are compared [17, 18].

Microdisks are commonly fabricated in the ‘free-standing’ geometry, where the central region of the disk is resting on a pedestal and its outer parts, in which the resonant modes mainly propagate, are suspended in air or vacuum. Such structures often suffer from thermal problems due to the limited heat sink into the substrate [19]. To circumvent this issue, microdisks can be fabricated in a ‘supported’ geometry. Here, the whole bottom facet of the disk is in contact with the substrate. A problem that can arise in these resonators is the coupling of light into the substrate, as the refractive index contrast at the bottom facet is reduced. This is especially true in the outer disk regions that contain fields with high intensities when modes are propagating in the disk [19].

In this work, microdisk resonators that were fabricated based on ZnSe and doped with halogen atoms in the group of Alexander Pawlis, Forschungszentrum Jülich, are optically characterized by micro-photoluminescence (μ PL) and structurally by scanning electron microscopy (SEM). For the latter analysis, an algorithm extracting the disk boundary from microscopy images was developed. This, for the first time, enables an assessment of edge roughness and optical quality of the same resonator and therefore allows a direct comparison of different microdisks fabricated in the same process. As expected from the discussion above, a correlation between the edge roughness and optical quality of the resonators, based on the quality factor of the observed WGMs, is found. Theoretical calculations of the resonances in the deformed microdisks, done by Jan Wiersig, Universität Magdeburg, confirm the experimental results.

Additionally, an introduction and first characterization of microdisks in the above mentioned supported geometry is presented. These disks were fabricated with a technique new to the II-VI material system that promises better thermal contact to the substrate and enhanced integratability into chip structures. Reproducible whispering gallery resonances are observed on the deep level emission, showing a high quality of the fabricated resonators. The structural quality of the microdisks is confirmed by the analysis of SEM images. Therefore, this work presents a new method to assess the edge roughness of microdisk

resonators (in both free-standing and supported geometries) and analyses the effect of edge roughness on the optical properties of microdisk resonators.

The thesis is structured as follows:

In section 2, the basic physics behind the analyzed structures is discussed, including an introduction to the ZnSe material system and microdisk resonators.

Section 3 is a summary and review of previous work by other researchers on microdisks and their applications. This provides the context to the results presented here and explains how this work advances the understanding of microdisk resonators.

In section 4, the fabrication of the analyzed microdisks and the methods used for their analysis are presented in detail.

This is followed by section 5, in which the obtained results are shown and discussed. Each of the three subsections is dedicated to the discussion of a different microdisk structure.

Finally, in section 6 all results are summarized and conclusions are drawn. Additionally, an outlook on further experimental work is given that could continue the analysis discussed in section 5.

2. Background

This section provides a description of the basic physical principals needed to understand the discussion of the results presented in this work.

It starts with the properties of II-VI semiconductors, with a special emphasis on ZnSe and ternary compounds derived from it. These materials are the basis for the fabrication of the analyzed samples and microdisks. In the second part, an introduction of the microdisk structures that are analyzed in this work and the underlying physics of their emission is given. Special focus is put on the formation of WGMs. The section closes with the description of the basics of different methods for the calculation of WGM resonances in microdisks employed in this work.

2.1. II-VI Semiconductors

II-VI Semiconductors consist of elements from the 2nd and 6th group (including subgroups) of the periodic table of elements, e.g., ZnSe or CdS. These materials are applied as emitters in the blue spectral range due to their large exciton binding energy and oscillator strength [1,2], as will be discussed in more detail in Section 3.1. Here, their basic material properties are introduced, which need to be understood for the growth of the ZnSe-based structures with tailored emission properties analyzed in this work.

2.1.1. Crystal Structure and Growth

II-VI semiconductors can crystallize in both the zinc-blende and the wurtzite structure, some compounds form in the rock-salt crystal structure.

In both the zinc-blende and the rock-salt structure, the two different elements each form a face-centered cubic (fcc) sublattice. Therefore, the whole crystal can be described as a fcc structure with a diatomic base and a side length a of the unit cell. The difference of the two structures is found in the way the atoms are coordinated, for zinc-blende the sublattices are shifted diagonally into the fcc unit cell by $\frac{a}{4}$. The shift is $\frac{a}{2}$ along one of the crystal axes for rock-salt, resulting in a three-dimensional checker board pattern.

A wurtzite II-VI crystal consists of two interpenetrating hexagonal close-packed sublattices. Here, each atom has four nearest neighbors of the opposite type, identical to the zinc-blende structure; six nearest neighbors of opposing atom type can be found in the rock-salt structure. The main difference between the zinc-blende and the wurtzite structures is found in the stacking order of the atomic layers, which is repeated every two layers for wurtzite and every three layers for zinc-blende.

For the semiconductors that are most relevant to the structures analyzed in this work, it

is found that zinc-blende is the thermodynamically stable phase of ZnSe, for CdSe this is the wurtzite structure, and MgSe usually grows in the rock-salt structure. Different crystal structures are possible for II-VI materials when growth parameters are chosen accordingly, e.g., ZnSe can be grown in the wurtzite structure at growth temperatures $T > 1425$ °C [20].

In the fabrication of semiconductor structures for light emission, often ternary alloys are used, an example being $\text{Zn}_{(1-x)}\text{Mg}_x\text{Se}$, denoting an alloy where the group II metal atoms are a mixture of Zn (with a fraction of $1 - x$) and Mg atoms. Since these materials typically need to be combined in a layered growth, all materials should grow in the same crystal structure and with similar lattice constant a . The samples analyzed in this work are fabricated in the zinc-blende structure. Ternary $\text{Zn}_{(1-x)}\text{Mg}_x\text{Se}$ can be fabricated with a magnesium fraction of up to 40 % ($x = 0.4$) [21]. In ternary $\text{Zn}_{(1-y)}\text{Cd}_y\text{Se}$, the wurtzite structure can be found even for low values of y [22]. This needs to be avoided in the fabrication of the samples discussed in this work.

The lattice constants of ternary alloys can be calculated using Vegard's law [23], this shows a linear variation of a with x , as can be seen for $\text{Zn}_{(1-x)}\text{Mg}_x\text{Se}$ in Equation 2.1:

$$a_{\text{Zn}_{(1-x)}\text{Mg}_x\text{Se}}(x) = xa_{\text{MgSe}} + (1 - x)a_{\text{ZnSe}}. \quad (2.1)$$

As mentioned above, the growth of layered materials, e.g., using molecular beam epitaxy (see Section 4.1), requires low differences Δa in their lattice constants to ensure defect-free two-dimensional growth. This can be seen in the fact that with lattice mismatches as low as $\Delta a = 5$ %, the resulting strain can lead to island growth on a wetting layer (so-called Stranski-Krastanov-type growth) [24].

As an overview, Figure 2.1 shows the bandgap energies E_g of different II-VI materials that are used in the structures analyzed in this work as a function of their lattice constant a . The bandgap energies will be discussed in the following section. GaAs, which is commonly used as growth substrate for zinc-blende ZnSe-based materials due to its low lattice mismatch with ZnSe ($\Delta a = 0.25$ %), is included in this figure as a reference.

2.1.2. Band Structure and Light Emission

Light emission from semiconductors is usually due to radiative recombination, where, in the most simple case, an excited electron directly recombines from the conduction band into the valence band. The excess energy is emitted as a photon. Therefore, the main factor determining the wavelength of light that is emitted from a semiconductor under optical or electrical excitation is the energetic difference between the valence band maximum and conduction band minimum (bandgap energy) of the material. As discussed

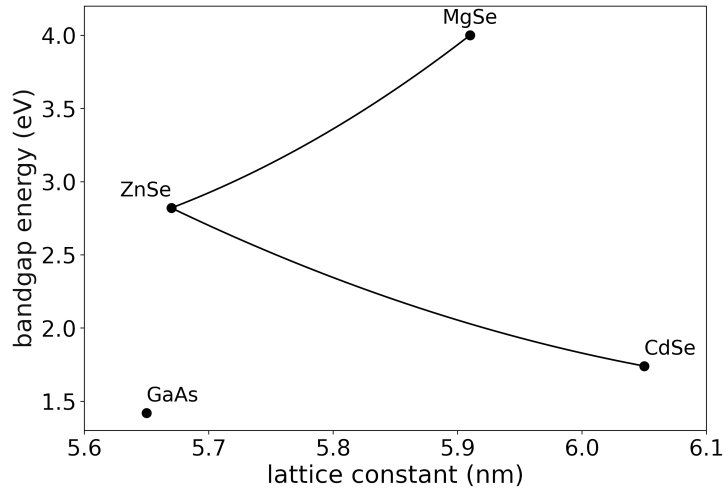


Figure 2.1: Lattice constant and bandgap energy for II-VI materials used in this work and GaAs at room temperature. Data from [25–27].

above, these energies are given in Figure 2.1 for different II-VI semiconductors.

It is important to note that the bandgap is direct for ZnSe and CdSe as well as for ZnMgSe in the zinc-blende crystal structure [21]. This means that the momentum for holes at the valence band maximum and electrons at the conduction band minimum is equal. In the case of the materials mentioned above, this is found at the Γ -point ($\vec{k} = 0$). In direct-bandgap materials, the rate of radiative recombinations is significantly higher opposed to indirect-bandgap materials, since the transition of the electron from the conduction band to the valence band does conserve momentum without the need for additional phonons. Optical excitation of these materials is more effective because of the same reason.

The bandgap energy of ternary alloys can be calculated using Vegard’s law [23], but a bowing parameter b must be introduced [26, 27]. This is shown in Equation 2.2 for a $\text{Zn}_{(1-x)}\text{Mg}_x\text{Se}$ alloy:

$$E_{g,\text{Zn}_{(1-x)}\text{Mg}_x\text{Se}}(x) = xE_{g,\text{MgSe}} + (1-x)E_{g,\text{ZnSe}} - x(1-x)b \quad (2.2)$$

Experimentally, a bowing parameter of 0.4 eV was observed for $\text{Zn}_{(1-x)}\text{Mg}_x\text{Se}$ [26], and $b = 0.47$ eV for $\text{Zn}_{(1-y)}\text{Cd}_y\text{Se}$ [27].

Using this information, a combination of two ternary alloys can be found with similar lattice parameters (leading to high growth quality) but different bandgap energy. This is useful for so-called double heterostructures, which are the basis for efficient emission from semiconductor structures and will be introduced in Section 2.2.1.

When an electron is excited into the conduction band, it can bind to the hole created in the valence band due to their Coulomb interaction. The resulting quasi-particle (a

bound electron-hole-pair) is called exciton. In inorganic semiconductors, these excitons are usually weakly bound (Wannier excitons) and can freely move through the crystal. A comparably high binding energy E_X^B between the electron and hole is observed in II-VI materials due to their strong Coulomb interaction, e.g., 20 meV in ZnSe [28]. This is favorable for emitting semiconductor structures, as the excitons have a higher chance of recombining (radiatively) instead of disspating. The emission energy of a material can be further influenced by restricting the charge carriers or excitons in one or more spacial dimensions, this will be discussed in Section 2.2.1.

Additionally, the emission of light from a semiconductor can be influenced by defects in the crystal lattice creating electronic states in the bandgap of the material. If these states are close to the center of the gap (deep states), recombination across them leads to emission of photons with energies significantly below the bandgap energy, the deep-level emission (DLE).

Shallow states in the bandgap, separated into donors (states near the conduction band edge being filled at $T = 0$) and acceptors (states near the valence band edge being empty at $T = 0$), are usually introduced intentionally during the growth process (doping). This is done because these states will lead to a larger amount of free charge carriers in the material at room temperature, improving its conductivity.

Excitons can bind to these impurities of the crystal, resulting in a reduction of their recombination energy by the binding energy to that specific defect.

In this work, the optically active regions of the used microdisk structures are doped with halogen (fluorine and chlorine) atoms. They can not only be used to provide shallow donor states and trap excitons, but can additionally be applied in the storage of qubits, as will be discussed in Section 3.1.

The bandgap of semiconductors usually decreases with rising temperatures, since the increased movement of atoms leads to a higher average distance between them, thus, the binding energy is reduced. This can be described using the Varshni equation [29]:

$$E_g(T) = E_g(T = 0) - \alpha \frac{T^2}{T + \beta}. \quad (2.3)$$

$E_g(T = 0)$ is the bandgap at zero temperature and α and β are empirical fit parameters. β correlates with the material-specific Debye temperature, a measure for the phonon frequencies occurring in the material, which can be used to estimate the heat capacity and electrical conductivity of a crystal.

2.2. Microdisk Resonators and Whispering Gallery Modes

Here, the so-called double heterostructure, which is the base for emission from the structures analyzed in this work, is introduced. This is followed by a discussion of the working principals for optical resonators in general. Total internal reflection, the basic physical process for the microdisk resonator, and the formation of whispering gallery modes will be detailed at the end of this section.

2.2.1. Semiconductor Heterostructures

For efficiently emitting semiconductor structures the exciting (optical or electrical) energy should be converted into light by recombination of free carriers or excitons in a relatively small volume. A ‘trapping’ or injection of the electrons and holes into a region of interest can be achieved using a double heterostructure. In this architecture, two semiconductors with different bandgap energies are combined by epitaxial growth [30], e.g., ZnCdSe and ZnMgSe. For efficient emission, the semiconductor with the smaller bandgap is encapsulated between two layers of the second material. The resulting course of the valence and conduction bands is schematically shown in Figure 2.2. Free electrons and holes or excitons ‘created’ by excitation of the barriers made from material A (larger bandgap) will move to the energetically favorable position in the center region made from material B (smaller bandgap) and recombine there.

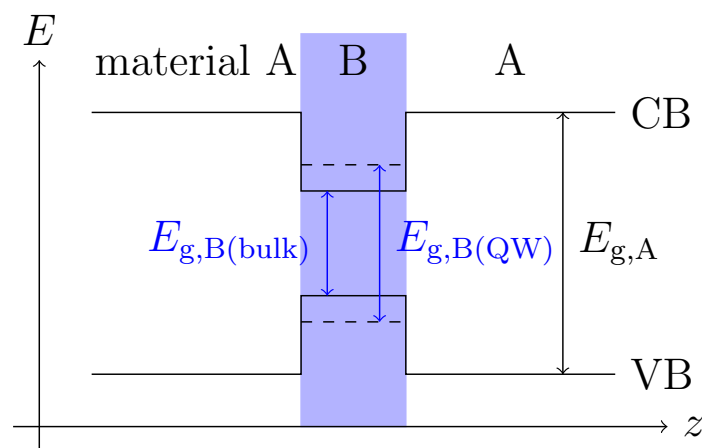


Figure 2.2: Sketch of the course of valence band maximum (VB) and conduction band minimum (CB) as a function of position along the growth direction in a double heterostructure. The black arrow indicates the bandgap energy for the barrier material A ($E_{g,A}$); the blue arrows indicate bandgap energies in the central region in bulk ($E_{g,B(\text{bulk})}$) and including the confinement energy found in a QW structure ($E_{g,B(\text{QW})}$).

If the width of the central region is on the order of the de-Broglie wavelength of the carriers (typically up to a few tens of nanometers [31]), the central region is a so-called quantum well (QW). Due to the quantum mechanical confinement effect, the energies of carriers in the QW are increased by a confinement energy which is larger for QWs with lower width. This can be used to tune the emission energy of the QW by varying its width [32].

In this work, ZnMgSe barriers are used to encapsulate QWs fabricated from ZnCdSe or ZnSe. This results in efficient emission from the analyzed structures, the difference in bandgap energy additionally reduces the reabsorption of emitted photons, which plays an important role for the generation of laser light in the structure, as will be seen in the discussion of optical resonators below.

2.2.2. Optical (Micro-)Resonators

The simplest possible form of an optical resonator is the so-called Fabry-Pérot structure that consists of two opposing mirrors between which light can be reflected back-and-forth, effectively ‘trapping’ the photons. Here, standing waves, the so-called modes of the resonator, can form. For this, the wavelength λ must be a multiple of the halved resonator length L . If the resonator is filled with a medium with a refractive index n_r , its m -th mode can therefore be calculated as

$$\lambda_m = \frac{n_r L m}{2}. \quad (2.4)$$

Such resonating structures are employed in the generation of light by stimulated emission, i.e., in lasers. This requires an ‘active medium’ in the resonator from which light can be emitted, usually using the transition between two electronic states in the material. The electrons are excited into a higher-energetic state by an external energy source (pump), and upon relaxation to their ground state the energetic difference is emitted as a photon. This light travels through the resonator and can stimulate the relaxation of other excited electrons, sending out further photons with identical wavelength, propagation direction, and phase. This process of stimulated emission competes with the absorption of photons by electrons in the ground state. This is why ‘population inversion’, i.e., a larger population of the excited state than the ground state, is needed for the generation of laser light. To achieve this, a three- or four-level system is needed, because sustained population inversion is not possible in a two-level system (if both states are populated equally, stimulated emission and absorption occur with equal probabilities). This can be provided by the double heterostructure, electrons are absorbed in the barriers and relax to the QW before recombining. In order to obtain a good coupling to the resonant photons, the active material should be placed in a maximum of the field of the standing waves.

In this work, the QW in ZnSe-based double heterostructures will be used as active materials. A laser will excite electrons across the bandgap (mostly) in the barrier, relaxation to and subsequent recombination in the QW leads to the emission of light from the sample. A good overlap between the field of the resonator mode and the active region is ensured by the use of symmetrical heterostructures: With identical barrier thicknesses on both sides, the QW is positioned close to the center of the structure along the z axis.

In the emission spectrum of a resonator, modes will appear at the resonant wavelengths λ_m , as photons of this wavelength can travel through the resonator several times and thus stimulate further emission. If the pumping power is increased, the system can switch from predominantly spontaneous to stimulated emission, this takes place at the lasing threshold. This change is accompanied by a drop of the linewidth of the observable modes due to the monochromacy of stimulated emission. Additionally, the onset of lasing can be observed in the emission intensity. In the regime of spontaneous emission, a linear correlation between the excitation power and the light output can be observed. This is because the number of excited electrons is proportional to the number of emitted photons. At the lasing threshold, a sharp increase of the emission intensity as a function of the pumping power is found, caused by the increase in efficiency. If the pumping power is increased further, this input-output characteristic returns to its previous linear slope, forming an 's-shape'. This happens when the transition to stimulated emission is complete and the efficiency of light emission is independent of pumping power again.

Resonators with sizes in the order of the wavelength of light are called microresonators or microcavities, this includes the microdisks analyzed in this work. These types of structures are interesting for various applications, as their small volume leads to low energy requirements in operation. Furthermore, the free spectral range between two modes is inversely proportional to L , making single modes more easily distinguishable and addressable in microresonators.

The optical quality of resonators is usually assessed based on the losses that are observed for resonating modes. In Fabry-Pérot structures, these can be due to imperfect mirrors through which a part of the light can be transmitted. Generally, scattering of light out of the resonator, absorption, and leakage of mode intensity into surrounding materials are the main contributions to losses.

This can be quantified if an exponential decrease of the oscillating electric field E over time with an attenuation constant Γ is assumed:

$$E(t) \propto \cos(\omega t)e^{-\frac{1}{2}\Gamma t}. \quad (2.5)$$

In this case the energy density u is given by

$$u(t) = (E(t))^2 \propto \left(e^{-\frac{1}{2}\Gamma t}\right)^2 = e^{-\Gamma t}. \quad (2.6)$$

The reduction of the energy density over time in the structure can be calculated:

$$-\frac{du(t)}{dt} = \Gamma u(t). \quad (2.7)$$

This can be used to define the quality factor (Q -factor) of the resonator as the ratio between the energy density in the structure and the losses per optical period of length T :

$$Q = 2\pi \frac{u(t)}{-\frac{du(t)}{dt} \cdot T} = \frac{2\pi}{\Gamma \cdot T} = \frac{\omega}{\Gamma}. \quad (2.8)$$

A Fourier transformation shows that this is equivalent to a definition of Q as the ratio between the resonant wavelength λ_m and the full width at half-maximum (FWHM, δ_{λ_m}) of this mode.

$$Q = \frac{\lambda_m}{\delta_{\lambda_m}} \quad (2.9)$$

This additionally shows that losses in the resonator lead to a broadening of the emission line.

2.2.3. Total Internal Reflection

When light reaches an interface between two media with different refractive indices $n_1 > n_2$, transmission and reflection of the light can occur. The law of reflection states that the reflection angle α_r is equal to the incident angle α_i . The transmission angle α_t is larger if the light is transmitted into a medium with lower n , according to Snell's law:

$$n_1 \sin \alpha_i = n_2 \sin \alpha_t \quad (2.10)$$

This situation is illustrated in Figure 2.3.

Since the angles α_i and α_t have a fixed interrelation, an increase of α_i will result in an increase of α_t . At a certain value of $\alpha_i = \alpha_{\text{tot}}$, α_t will be 90° , meaning that no transmission is possible for $\alpha_i \leq \alpha_{\text{tot}}$; this phenomenon is known as total internal reflection.

Here, the complete intensity of the light is reflected, only a small field whose intensity decays exponentially with the distance from the interface is found in the medium with

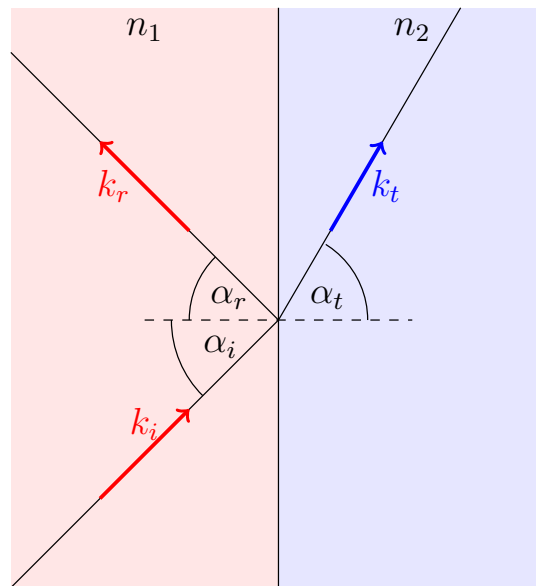


Figure 2.3: Reflection (direction of propagation \vec{k}_r) and transmission (\vec{k}_t) of an incident beam of light (\vec{k}_i) at an interface between different refractive indices $n_1 > n_2$. Angles (to the interface normal) are given for all three beams using the same subscripts.

lower refractive index. This so-called evanescent field can be coupled into a material with sufficiently high n that is brought in close proximity to the interface. This is known as the optical tunneling effect ‘frustrating’ the total internal reflection.

Total internal reflection can be used to fabricate optical resonators by bending their walls, curving the path of the light until it describes a circle. Optical tunneling provides a possible way of coupling light into and out of these resonators via waveguides in their vicinity. These type of resonators will be discussed in the following section.

2.2.4. Whispering Gallery Mode Resonators

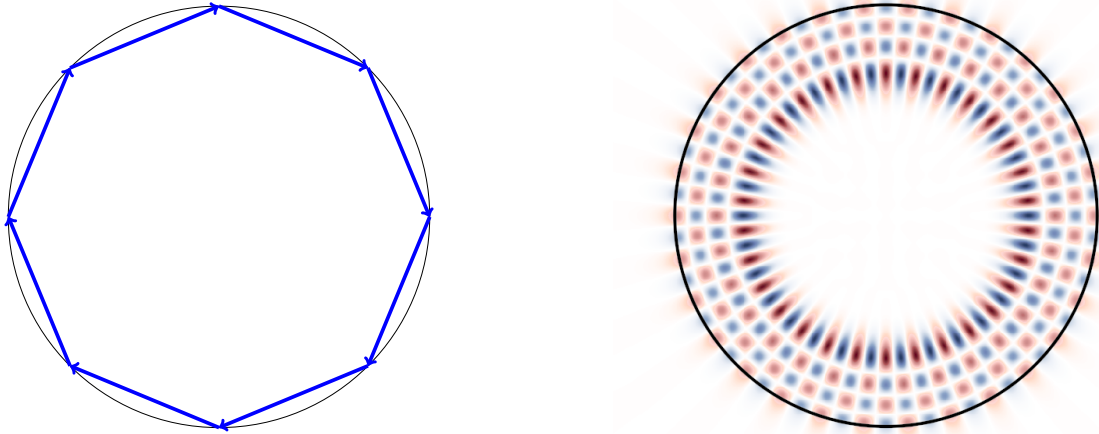
The so-called Whispering Gallery Modes (WGMs) are named after the 34 m-diameter ‘whispering gallery’ in St. Paul’s cathedral in London, England. The namesake of this dome is an interesting acoustical effect that can be observed in it: A whisper of a person standing in the gallery can be heard by a person on the opposite side, if the whispering person does not speak in the diagonal direction of the listening person, but turns their mouth in parallel to the wall. In this case, the whisper undergoes total reflection along the wall and eventually reaches the listener with strongly reduced losses. Similar ‘acoustic

whispering galleries' can be observed in other round structures as well, e.g., in the Temple of Heaven in Beijing.

This phenomenon was first explained by Lord Rayleigh, who observed that the sound mainly travels close to the border of the gallery. He assumed that the sound waves Ψ are characterized by Bessel functions J_n in the radial direction and an azimuthal oscillation which is shown in Equation 2.11 for polar coordinates (r, φ) with propagation velocity a and wave vector $k = \frac{2\pi}{\lambda}$ [33]. The distribution of the sound waves can be measured experimentally [34].

$$\Psi_n = J_n(kr) \cos(kat - n\varphi) \quad (2.11)$$

Optical WGMs can be observed in round (circular or spherical) resonators. This was demonstrated in microspheres [35] as well as 2D structures, like the microdisks analyzed in this work [36], as well as in microrings [37].



(a) Ray-optical representation of the formation of a WGM.

(b) Electric field corresponding to a WGM in a microdisk resonator.

Figure 2.4: Whispering Gallery Mode resonances in a microdisk resonator in ray- and wave-optics.

The above-mentioned total internal reflection acts as the mechanism of the containment of light in these structures. This can be illustrated using ray optics, as seen for a microdisk in Figure 2.4a. Analogous to the acoustic waves discussed above, the fields in the disk that correspond to a resonance are described by radial Bessel functions and an oscillation in the azimuthal direction. This is observable in experiments. Especially the azimuthal oscillation can be imaged using a measurement of the near-field emission of the disk [38,39].

An exemplary field distribution for a mode in a microdisk can be seen in Figure 2.4b. In this image, a mode of higher radial order is shown. The occurrence of such resonances is usually interpreted as a sign of high quality of the microdisk [40]. It is notable that ray-optics (compare Figure 2.4a) cannot explain the different radial orders of modes that are experimentally observable.

Roughness of the microdisk edge, sometimes denoted as its side facet, can play an important role for these types of resonators, because scattering at an imperfect boundary can lead to scattering losses [18, 41]. It is important to note that random edge roughness lifts the degeneracy of modes propagating in the resonator in clockwise and counter-clockwise direction [42]. This results in two modes which occur at very similar spectral positions, which can lead to an increase in the width of the mode if the two modes are too close to be observed individually. As this influences the Q -factor, this effect is known as ‘ Q -spoiling’. A further discussion of the influence of random edge roughness of microdisks - including previous experimental and theoretical results - can be found in Section 3.2.3.

2.3. Theoretical Calculation of Resonances in Microdisk Resonators

The spectral position, i.e., the wavelength or photon energy, of WGMs in microdisks can be calculated using different approaches. Two methods were used to obtain the results presented in this work. The author himself calculated resonances in perfectly circular microdisks using a finite-difference time-domain (FDTD) formalism. Further theoretical calculations were performed by professor Jan Wiersig at the University of Magdeburg. These are based on the boundary element method and take the roughness of the disk edges into account.

Generally, the propagation of light in microdisks is often treated as a two-dimensional problem, as their thickness is on the order of (few) 100 nm. An effective refractive index is often assumed for the structure, as the thickness of individual layers in z -direction is much smaller than the analyzed wavelengths.

WGMs can be calculated with a range of other methods, an introduction to them with a focus on random surface roughness can be found in Section 3.2.3.

2.3.1. Finite-Difference Time-Domain Method

The open-source software package *Meep* [43] was used in this work for FDTD simulations of microdisks.

In this method, space and time are discretized to a grid and time steps. The evolution of the electric E and magnetic H field in a given volume is calculated based on Maxwell’s

equations. Note that Maxwell's equations in 2.12 are shown in dimensionless units ($\epsilon_0, \mu_0, c = 1$), as *Meep* works in this system.

$$\begin{aligned}\frac{dB}{dt} &= -\nabla \times E - J_B - \sigma_B B \\ B &= \mu H \\ \frac{dD}{dt} &= \nabla \times H - J - \sigma_D D \\ D &= \epsilon E\end{aligned}\tag{2.12}$$

Here, D denotes the electric displacement field, and B the magnetic flux density. These variables are affected by the rotation of the magnetic or electric field, respectively, and by electric and magnetic-charge currents J/J_B as well as a reduction proportional to the electric / magnetic conductivity σ_D/σ_B .

The calculation of E and H is performed by using the 'Yee method' [44]: The values of the strength of the two fields are stored in slightly different grids (E at the corners, H in the centers of a two-dimensional grid of squares). Each grid spot then alternates between the calculation of new values for E and H as described by Equation 2.12 above.

FDTD calculations are typically limited by their computational expense. Thus, the resolution (pixels per unit length) and size of the analyzed system should be chosen to be as coarse as possible without reducing the accuracy of the simulation. Different options can be used for the boundary of the simulated area. This includes periodic boundary conditions or perfectly reflecting metallic borders with zero absorption, at which the fields are forced to be zero. In order to simulate the open boundary in this work, 'perfectly matched layers' (PMLs) are used as boundary condition, which perfectly absorb all incidenting fields. In order to avoid backscattering artifacts, the PMLs need to have a nonzero thickness. These PML boundary conditions are used to ensure that light which is emitted from the microdisk does not interfere with the resonating modes.

These simulations can be used to calculate resonant frequencies in microdisks, if the propagation of a short spectrally broad pulse in the resonator is analyzed. This is sketched in Figure 2.5.

Figure 2.5a illustrates the electric field in the resonator when the microdisk is excited by a pulse near the top. The field travels along the edge of the disk on both sides (clockwise and counter-clockwise propagation), interference patterns can be observed when both waves meet at the bottom of the resonator (Figure 2.5b). The further development of this system results in more complex patterns, as is indicated by Figure 2.5c. This is due to the fact that only fields that match resonances of the microdisk can continuously propagate in it. Other wavelengths that were included in the exciting pulse are emitted from the

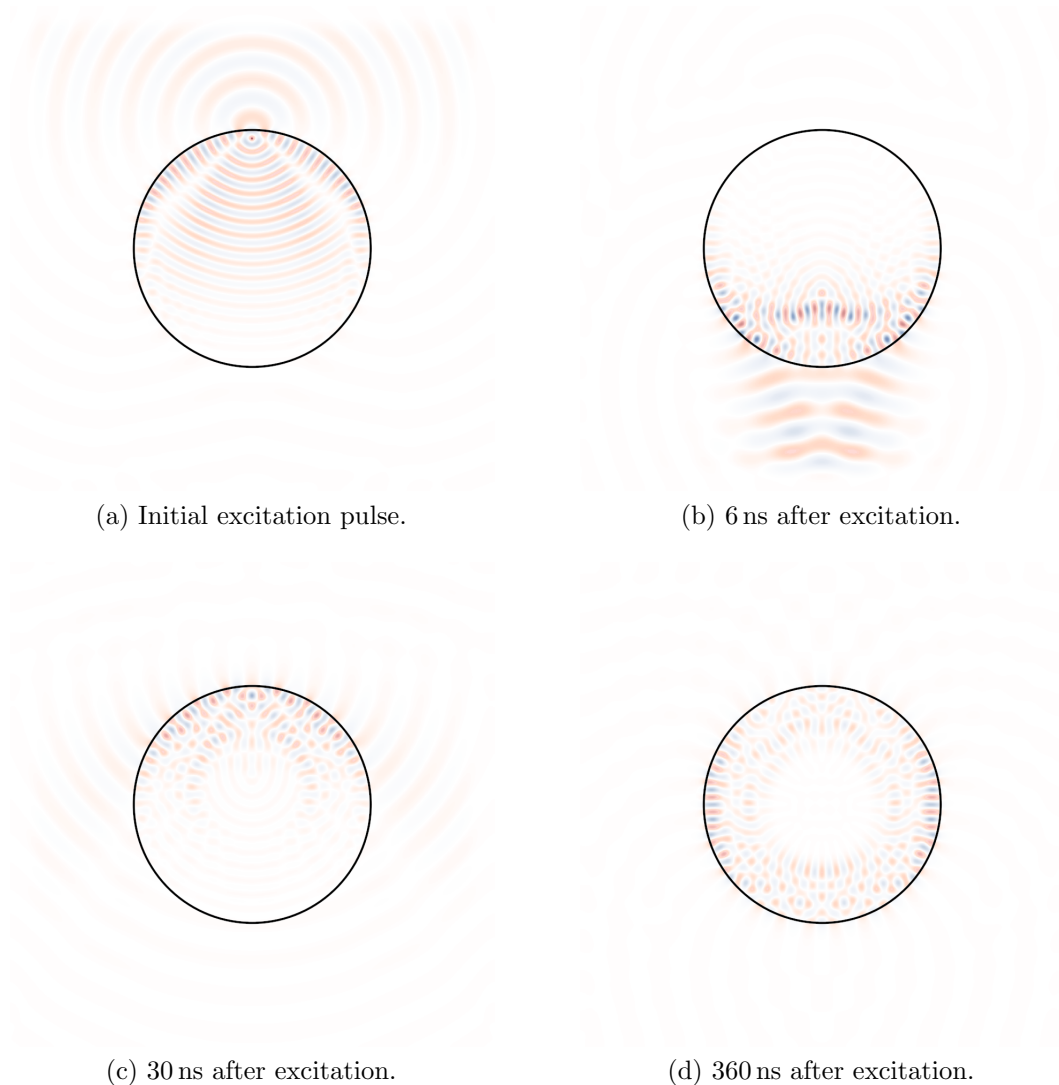


Figure 2.5: Exemplary illustration of the calculation of resonant modes in a microdisk ($d_{\text{disk}} = 2.86 \mu\text{m}$) using an FDTD simulation. The z -component of the electric field is shown for different time steps, as denoted in the individual captions.

resonator. Figure 2.5d shows the resulting simultaneous propagation of all modes that can be excited by the initial pulse.

At the point of excitation, the strength of the E field is recorded as a function of time. A Fourier transformation of this data then reveals the spectral position of the resonating modes as well as their spectral width that can be used to calculate the Q -factor. However, the width is not used in this work, as absorption in the resonator and edge roughness are both neglected in the FDTD calculations.

2.3.2. Boundary-Element Method

The boundary-element method was developed by Jan Wiersig for the calculation of resonances in cavities of arbitrary shape [45], it is therefore well suited for the analysis of deformed microdisks.

This ansatz replaces the two-dimensional Maxwell's equation problem (see Equation 2.12) known from the FDTD calculation above by a one-dimensional boundary integral equation using the Green's function formalism [46]. The boundary of the microdisk is then discretized.

In order to find resonances, the plane-wave scattering cross section σ of the structure is calculated. If σ is analyzed as a function of the wave number k , the modes can be seen as peaks. Both the spectral position and the width of the peaks are accessible in this method. Peaks with very thin or broad widths (very high or very low Q -factor) might not be detected with this method, as they might be located between two consecutive grid points or covered by noise, respectively. However, such resonances are not important in the analysis of lasing structures, as low- Q modes have a too low lifetime, and high- Q modes do not provide sufficient output power [45]. However, the assumption that very-high- Q WGMs are of no interest for lasing applications is under debate [47].

Spurious solutions can occur from these boundary integral equations, they assume a perfectly conducting boundary and equal material parameters on both sides of it [47, 48]. The number of these erroneous solutions can be reduced if the discretization of the boundary and k are selected appropriately [45].

3. State of the Art

In this section, previous research on emitters fabricated from ZnSe-based semiconductors and microdisk resonators in general will be presented and discussed. This starts with a discussion of possible applications of the ZnSe material system with a focus on microdisk resonators. Subsequently, the fabrication of microdisks is reviewed for different material systems and geometries. Finally, special focus is put on previous work regarding the influence of edge roughness on the optical properties of microdisks, which is one of the main topics of this work.

3.1. Applications of ZnSe-based Epitaxial Semiconductor Structures

ZnSe-based semiconductor structures are well suited for applications as emitters in the blue-green spectral region due to their large bandgap, high oscillator strength and large exciton binding energies, as discussed in Section 2.1. Light emitting diodes (LEDs) with luminescence in this spectral range were first reported in 1987 [1, 49] after epitaxial growth of *p*-type ZnSe was realized, about four years before the first LED based on GaN was demonstrated [50]. The first semiconductor lasing diode in the blue-green spectral range was fabricated based on a ZnSe QW structure reported by Haase et al. in 1991 [2], which further emphasized the suitability of this material system for emission at these wavelengths. However, these and similar devices showed significant degradation when in operation, limiting the device lifetime to a maximum of a few days [3]. This degradation was revealed to originate from point defects native to the material, nonradiative emission at them heats the lattice, which leads to the growth of dislocations, further reducing the emission from the structure [3, 51, 52].

From this it is evident that ZnSe is often not suited for applications that require high powers, e.g., conventional (edge emitting or VCSEL) laser diodes. Nonetheless, the good emission properties of this material class can still be applied in devices that do not require large operating powers or currents, e.g., for the emission of single photons. Single photon emission has been reported from excitons bound to nitrogen acceptors in ZnSe/ZnMgSSe QW structures [15]. This was also found for recombination of excitons bound to isolated fluorine donors in ZnSe/ZnMgSe QWs [53], these structures are similar to those analyzed in this work. Photons emitted from two (spatially) separate structures were entangled [54, 55], this process is the basis for secure communication via quantum cryptography [6]. Similar experiments have shown that the spin of a single electron bound to such a donor can function as an optically accessible qubit [16, 53, 56]. This opens the door for the application of these structures in quantum computing.

As both of these applications require a high optical quantum efficiency, placing these structures into resonators with low losses is necessary [53]. These should be integratable into chip structures, which is why ZnSe-based microdisks resonators appear well suited for these devices. Microdisks and their applications will be discussed in the following.

3.2. Microdisk Resonators

As discussed in Section 2.2.4, microdisks are easy to fabricate in both the ‘free-standing’, i.e., underetched and resting on a pedestal, and ‘supported’, i.e., in complete contact with the substrate, geometry. Additionally, they provide resonances with low losses due to the confinement by total internal reflection. Because of this, microdisk resonators have been explored in many different material systems, mainly as a platform for low threshold lasers. This research is discussed in the following, with an emphasis on the ZnSe material system used in the experiments presented in this work.

3.2.1. ZnSe-based Microdisk Resonators

The first observation of lasing in a microdisk fabricated from II-VI semiconductors was reported by Hovinen et al. in 1993 [57]. In their work, three $\text{Zn}_{0.8}\text{Cd}_{0.2}\text{Se}$ quantum wells were grown embedded in $\text{ZnS}_{0.07}\text{Se}_{0.93}$ barriers and underetched to form a free-standing resonator. Under optical pumping a threshold excitation density of $100 \frac{\text{kW}}{\text{cm}^2}$ was presented for a disk with a diameter of $7 \mu\text{m}$ at room temperature.

A significant reduction of the laser threshold was achieved using fluorine-doped ZnSe quantum wells embedded in $\text{Zn}_{0.9}\text{Mg}_{0.1}\text{Se}$ barriers. At 5 K, a lasing threshold of $15 \frac{\text{W}}{\text{cm}^2}$ was reported for a disk with a diameter of $3 \mu\text{m}$ [14], while a similar disk with $d_{\text{disk}} = 6 \mu\text{m}$ exhibited a slightly higher threshold of $100 \frac{\text{W}}{\text{cm}^2}$ [58]. PL spectra with rising excitation density of the latter disk can be seen in Figure 3.1. As noted in the figure, high Q -factors were observed for these disks (2500 for $d_{\text{disk}} = 3 \mu\text{m}$, 3100 for $d_{\text{disk}} = 6 \mu\text{m}$), indicating low losses which contribute to the reduction of lasing threshold. Raman analysis of the free-standing disks used in these experiments showed that they are free of extended defects [59] and that the strain exerted on the ZnSe:F QW by the ZnMgSe barriers and the GaAs post remaining from the substrate is released homogeneously along the radius of the microdisk [60].

A different ZnSe-based design of the active region is used in [61] where a CdSe QW was embedded in thin layers of ZnSe. By varying the thickness of the QW between 1 and 6 monolayers, the emission wavelength of this structure could be tuned over the whole spectral range. The formation of quantum dots via island growth due to the different

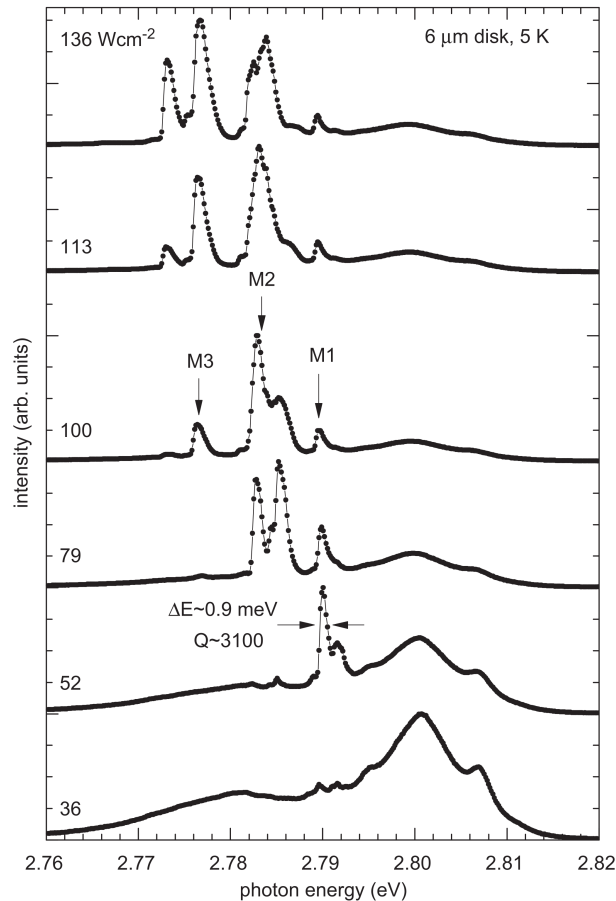


Figure 3.1: PL spectra of a free-standing microdisk with a diameter of $6\ \mu\text{m}$ at different excitation densities. Lasing WGMs labeled M1, M2 and M3 are seen growing from the background emission. From [58].

lattice constants of QW and barrier was avoided by an additional ZnMgSe cladding whose composition was adjusted depending on the thickness of the CdSe layer [32]. WGMs with a Q -factor of about 700 were observed in the emission from disks in this configuration. However, lasing was not observed, this is likely due to the low volume of the gain material (few monolayers).

In [62], it was shown that the light emitted from ZnSe-based free-standing microdisks can couple into a partly-underetched adjacent ZnSe-based waveguide fabricated together with the resonator in the same process. This opens a possible path towards the integration of microdisks as optical elements into electronic chip structures.

Renner et al. noted that the underetching of free-standing microdisks can introduce additional edge roughness, and that free-standing disks can bend out of plane [63, 64]. Both processes reduce the optical quality of the resonators. To avoid this, they introduced a different fabrication technique: Instead of the underetching step in the fabrication of free-standing disks, the microdisks were glued onto glass plates, and the whole substrate

was removed. This process was performed with microdisks containing CdSe quantum dots grown in a ZnSe barrier and $\text{Zn}_{0.93}\text{Mg}_{0.07}\text{S}_{0.14}\text{Se}_{0.86}$ cladding [63–65]. WGMs with Q -factors exceeding 2000 were observed at room temperature [63]. At 4 K, lasing was shown with a threshold of $640 \frac{\text{W}}{\text{cm}^2}$ in a disk with a diameter of $3 \mu\text{m}$ [65]. The analysis of the disks on a transparent glass substrate allowed for a measurement of the emission spectra as a function of the angle between the disk plane and the direction of detection. This revealed that WGMs can be observed with higher intensity when the detection is parallel to the disk plane [63]. An alteration of the resonator, namely cutting the disk into a ring, led to strong coupling between the cavity mode photon and quantum dot exciton with a Rabi splitting of 0.7 meV [8]. WGMs with Q -factors of 2000 were observed in these altered resonators, too.

Recently, a different fabrication technique for microdisks in direct contact with a substrate was suggested, based on colloidal CdSe/CdZnSeS quantum dots. These were deposited layer-by-layer via spin-coating onto a substrate pre-patterned with a mask which was later used to remove quantum dots outside of the disk perimeters. WGMs with Q -factors between 1300 and 1700 were reported for relatively large disks (diameters between 10 and $55 \mu\text{m}$) [66].

This shows that ‘supported’ resonators allow the formation of WGMs with low losses and high fields in the resonator. However, the removal from the substrate after growth in the method of Renner et al. [63] means that their fabrication process is not suitable for the integration of the microdisks into chip structures. The second process described above, the fabrication of disks by spin-coating, is applicable to a wide range of substrates, but the resulting disks exhibit very rough sidewalls and inhomogeneous top facets [66]. In this work, supported microdisks fabricated using a different process - grown epitaxially and remaining on their original substrate - will be analyzed. The details of this fabrication process are discussed in Section 4.1.

3.2.2. Semiconductor Microdisk Resonators Based on other Materials

Microdisk resonators have been fabricated not only based on ZnSe, but other semiconductors as well. In this section, the results obtained using those semiconductor microdisks are presented. Since much research has been done on these resonators in the past 30 years, the discussion in this section is limited to results relevant for the experiments that will be discussed in Section 5 of this work. This means that, for example, electrically driven microdisk emitters are not discussed here, for this and similar topics the reader is referred to the review articles mentioned below.

III-nitride Semiconductors

III-nitride semiconductors, i.e., compounds of a metal from the third main group in the periodic table (Al, In, Ga) and nitrogen, are of interest in research on emitters in the blue-green spectral region [40]. Currently, commercially available blue and white LEDs and laser diodes are often based on this material class; the Nobel Prize in 2014 was awarded for contributions to the development of these devices [4].

Consequently, a lot of research has been done on the fabrication of microdisk resonators from these materials. Therefore, the discussion in this section is limited to results relevant to the results presented in this thesis, i.e., to reports of optically pumped free-standing and supported microdisks and their edge roughness. For further details, an extensive review of III-nitride microdisk resonators can be found in [40].

GaN-based disks can be grown on sapphire (crystalline Al_2O_3), but the polarity of the wurtzite structure of III-nitrides leads to high anisotropy in wet etching processes [67]. Because of this, undercutting the structures is difficult. Supported microdisks fabricated by dry etching of the GaN-based material showed WGMs, but no lasing was observed. This is explained by the low refractive index contrast between the disk and substrate material, which causes losses by coupling of light into the substrate [68].

The introduction of a ‘sacrificial layer’ of InGaN that could be selectively etched led to an undercut of $\text{In}_{0.14}\text{Ga}_{0.86}\text{N}/\text{GaN}$ multi-QW structures. These free-standing disks exhibited Q -factors up to 4650 [67] and lasing at room temperature with a threshold of about $300 \frac{\text{W}}{\text{cm}^2}$ [69].

These disks can be grown on Si substrates as well [70], enabling the integration of the microdisks with other Si-based chip structures. However, the large lattice mismatch and differences in the thermal expansion between Si and GaN are difficult to overcome, and the small silicon post is not sufficient to dissipate heat created in nonradiative recombination processes [40]. Additionally, mask erosion in the photolithography used for the fabrication of these structures led to rough sidewalls, a combination of these drawbacks prevents lasing at room temperature [70]. However, room temperature lasing was reached in microdisks fabricated using microsphere lithography which yields significantly smoother disk edges. In this process aluminum [71] or silica [71–73] spheres were deposited on the III-nitride material after growth and acted as masks for the etching of the microdisks. A lasing threshold of about $10 \frac{\text{W}}{\text{cm}^2}$ was observed under pulsed excitation [71]. The influence of edge roughness on the optical properties of GaN-on-Si microdisks was studied in detail in [17, 18]; this is discussed in depth in Section 3.2.3. The use of quantum dots as gain medium - instead of (one or multiple) quantum wells - lead to a record Q -factor of 7300 and a low lasing threshold ($60 \frac{\text{W}}{\text{cm}^2}$) [74]. This is due to the narrow linewidth of the quantum dot emission and the reduced reabsorption of photons in the resonator [40].

GaN can be grown self-assembled in hexagonal microdisks, from which WGMs and lasing can be observed [75–77]. These disks are not underetched, and Q -factors around 700 and a lasing threshold of $300 \frac{\text{W}}{\text{cm}^2}$ were observed [75]. A major disadvantage of this ‘bottom-up’ synthesis (in contrast to the ‘top-down’ structuring of semiconductors grown epitaxially) is that the geometry and location of the resonators is hard to control [40].

Other III-V Semiconductors

The first experimental demonstration of a semiconductor microdisk laser in 1992 showed emission in the infrared spectral region from an InP/InGaAsP disk [36].

Based on III-arsenides [78, 79] and -phosphides [80], microdisk emitters in the infrared can be fabricated with applications in telecommunication networks. Q -factors above 10^5 were reported in such systems, commonly employing InAs quantum dots as active materials [78, 79]. The Q -factors are higher in these infrared systems because of their larger wavelengths, leading to a strong or complete reduction of reabsorption in the resonator [81]. A review of infrared lasers fabricated using III-V semiconductors can be found in [82].

In the context of this work, it is interesting to note that the influence of edge roughness on the properties of the emission has been studied in this material system [83], this is discussed in more detail in Section 3.2.3.

Zinc Oxide (ZnO)

ZnO is commonly researched as a material for UV optoelectronic applications due to its wide and direct bandgap and large exciton binding energy. Similar to the III-nitride materials discussed above, it grows in the hexagonal wurtzite crystal structure. Therefore, ZnO-based microdisks can be fabricated by both self-assembled bottom-up growth and top-down structuring; a review of resonators of both types can be found in [84].

Similar to III-nitrides, top-down structuring of ZnO is difficult due to a lack of selective etching processes for this material, especially in sub-micrometer dimensions [85]. Direct top-down structuring of ZnO thin films into microdisks has been reported, but no undercut was performed. The measured Q -factors were very low (125), and the patterned sample only showed a 17% reduction of lasing threshold compared to the as-grown ZnO film [86]. Liu et al. [87] proposed to grow a thin layer of ZnO on pre-patterned SiO₂ microdisks. They demonstrated lasing from such samples at a threshold of $0.3 \frac{\text{W}}{\text{cm}^2}$ for a large disk ($d_{\text{disk}} = 10 \mu\text{m}$). In ZnO disks grown on SiO₂, Q -factors as high as 4700 were observed [88]. The deposition of a SiO₂ capping layer, ‘sandwiching’ the ZnO film, improved the overlap between the gain material and the field of the mode, which led to enhanced emission [89]. Self-assembled hexagonal ZnO microdisks can be grown on different substrates, e.g., Si [90],

SiO₂ [91] or sapphire [92–94]. In these hexagonal structures the angles between the the surface normal and propagating light cannot become arbitrarily large for continuous total internal reflection. Because of this, the WGMs in these structures exhibit greater mode loss. Additionally, the disks are not free-standing which leads to a higher scattering loss into the substrate material [91]. This reduces the Q -factor in comparison to free-standing disks. Only a few publications, which achieved highly symmetric resonator shapes with low surface roughness, reported Q -factors in excess of 1000 [90, 92–94].

For applications of these resonators, it is notable that in some experiments the ZnO was excited via two photon absorption which proves that IR light sources can be used to optically pump ZnO disks [90, 95].

Silicon-based (Si, SiO₂ and Si₃N₄)

Si microdisks are usually fabricated as ‘cold’ cavities, i.e., without gain material, measured in transmission. This leads to high Q -factors on the order of 10^5 to 10^6 [96], because there is no absorbing material in the resonator. The losses in such resonators have been revealed to be dominated by scattering at the edge roughness [17, 18] which will be discussed in more detail in Section 3.2.3. Furthermore, it was reported that Si disks that were not underetched and therefore are in contact with the SiO₂ underlayer over their whole bottom region exhibited less thermal problems while maintaining a comparably high Q -factor [19, 97]. This can be explained with the large refractive index contrast between Si ($n = 5.30$ [98]) and SiO₂ ($n = 1.46$ [99], both at 500 nm). However, Si shows losses in the visible spectral range; this can be avoided by fabricating microdisks from silicon nitride (Si₃N₄), such disks support Q -factors above 10^6 [100, 101].

These microdisks can be combined with emitters as ‘active’ material, this is commonly done by encapsulating colloidal quantum dots in Si₃N₄ [102–104] or SiO₂ [105]. Q -factors in excess of 4000 have been reported in such systems for disks with diameters of 15 μm [103, 104]. Smaller disks exhibited lower values ($Q = 1150$ for $d_{\text{disk}} = 7 \mu\text{m}$) [103]. SiO₂ has demonstrated a higher stability when lasing in cw operation is reached in the resonator [105]. For these structures, embedding the emitters between a bottom layer and a cap of the Si-based material improves their emission, since a better optical confinement and overlap between the cavity mode and the position of the emitters is achieved [105].

3.2.3. Theoretical Analysis of non-ideal Microdisk Resonators and the Role of Edge Roughness

Roughness of the edges of microdisks has been shown to lead to scattering losses which reduce the Q -factor [68, 106, 107] and increase the lasing threshold [41]. In this section,

theoretical calculations of the spectral positions and Q -factors of modes in resonators affected by edge roughness are discussed. Experimental work that contributed to the analysis, e.g., by providing statistical information on the deformation of the microdisks, is included in this section as well. Here, the term ‘non-ideal’ microdisks is used to describe microdisks that are not ideally circular but deformed, as all ‘real’ microdisks are, e.g., due to imperfections on the sidewalls introduced by etching steps in the fabrication process. Only unintentionally deformed microdisks are discussed here, experimental and theoretical work has also been done on intentionally deformed disks to achieve directional emission [108]. This is not relevant for the results presented in this work, a review of this can be found in [47].

The theoretical calculation of resonances in microdisks is usually reduced to a two-dimensional problem by assuming an effective refractive index for the microdisk which can be justified by the small thickness of the disk along the z -axis [47]. This 2D problem can then be solved numerically using FDTD methods (see Section 2.3.1). Calculations based on this showed that both the resonant wavelengths and the Q -factors of WGMs scatter around the values found for ideally circular disks [109]. An important role in the reduction of the Q -factor for non-ideal microdisks is played by the splitting of the spectral position of clockwise and anti-clockwise propagating modes [42]. This leads to a ‘ Q spoiling’, where the two modes overlap and form one broader mode with a lower Q -factor. It was shown that the strength of this splitting strongly varies with the azimuthal order of the WGMs [110]. Other numerical calculations based on the scattering matrix technique found that surface roughnesses $\Delta r \leq \frac{\lambda}{30}$ can lead to a strong reduction of the Q -factor, especially for resonances with high Q -factors in the ideal case.

Deformed microdisks can also be studied using full-wave integral equation analyses which can be divided into volume and boundary integral-equations. The former is more computationally demanding, but has the advantage that refractive index changes of the microdisk along its radius (e.g., due to the post of free-standing disks) can be taken into account. These volume integral-equations were used to calculate the Q -factors and strength of splitting $\Delta\lambda$ between the clockwise and counter-clockwise propagating modes for free-standing microdisks fabricated from silicon [17]. A side-view SEM image of such a resonator can be seen in Figure 3.2a. For the calculation, the roughness of fabricated disks was extracted from SEM images as seen in Figure 3.2: The contrast in a top-view image (Figure 3.2b/c) was used to determine the deformation function $r(\varphi)$ (Figure 3.2d). Its autocorrelation was calculated and fitted with a Gaussian (Figure 3.2e). From that, the correlation length and standard deviation of the edge roughness were calculated which were then used as input parameters for the simulation. It was found that the Q -factor in these disks ($4.7 \cdot 10^5$ for a ‘cold’ disk with $d_{\text{disk}} = 5 \mu\text{m}$) is limited by surface roughness. It was shown that an

improved fabrication process could mitigate this and increase the Q -factor by one order of magnitude [18].

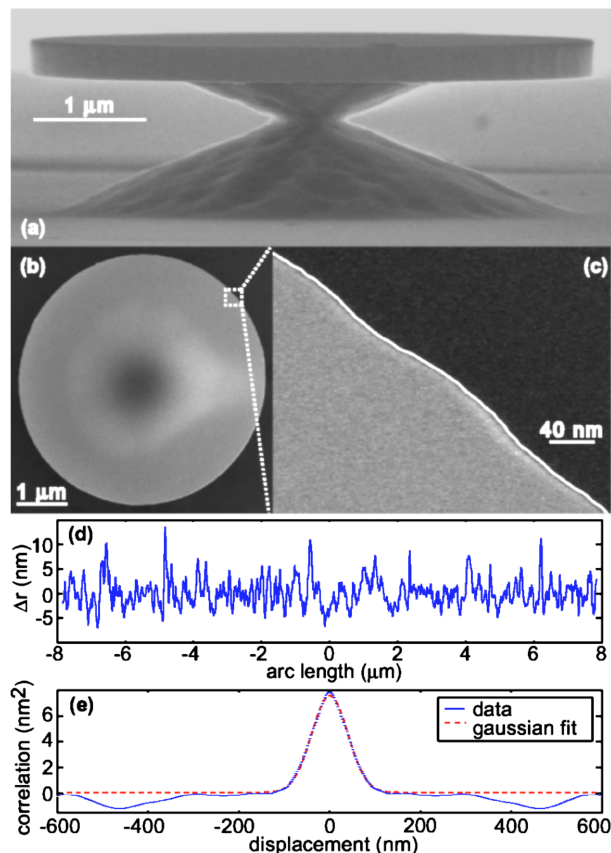


Figure 3.2: SEM analysis of a Si microdisk with a diameter of $5\ \mu\text{m}$. (a) side-view and (b) top-view images of the disk, (c) zoom into the top-view image with the extracted disk edge shown in white. (d) Plot of the extracted deformation function, (e) autocorrelation of the data in (d) and Gaussian fit. From [17].

A similar analysis process was applied for very smooth GaAs disks, whose edge roughness was too low to be observable in SEM [83]. Therefore, higher-resolution transmission electron microscopy (TEM) was used to extract the correlation length and amplitude of the edge roughness. The microdisks had to be removed from the substrate for this measurement, since samples need to be transparent to electrons in order to be suitable for TEM analysis. The mechanical removal of the disks from the substrate means that an optical and structural characterization of the same disk is not possible.

Boundary integral equations, like the boundary element method described in [45] which is used in this work (see Section 2.3.2), are less computationally demanding, but can only be applied to resonators with a uniform (effective) refractive index along their radial direction [47]. This method can be used to calculate resonances in deformed microdisks or the effect of the deformation on the mode propagation [111]. However, it is limited to

modes with low and middle Q -factors, because defect frequencies occur in the analysis along the ‘real’ resonances of the microdisk [47, 48]. These are eigenvalues of the 2D problem in which the border is assumed to be perfectly electrically conducting and the material parameters inside and outside are equal.

Recently, a perturbative approach for the calculation of resonances in deformed microdisks was introduced by Wiersig et al. [42]. Results obtained using this method agreed with the experimental data from the deformed Si disks analyzed in [17] (see Figure 3.2).

In this work, the edge roughness of free-standing and supported microdisks will be extracted from SEM images (for experimental details see Section 4.2.2). The deformation functions will be used as input parameters for theoretical calculations based on the boundary element method described in [45]. This is the first time that the deformation function measured for a disk is directly used as input for modeling of the WGMs that can propagate in this disk. This allows for a direct comparison of the theoretical calculations and the experimental characterization of the disk, including its ‘individual’ edge roughness. Additionally, these results will show that the boundary element method is sufficient to calculate WGMs in the microdisks analyzed here and is not impeded by the defect frequencies mentioned above.

4. Experimental Methods

In this section, the experimental setup and techniques needed to obtain the results presented in Section 5 will be presented and explained.

The section starts with the fabrication of microdisk resonators, which consists of a layerd growth and subsequent processing of the layers into microdisks. Both of these steps were performed in the group of Alexander Pawlis at the Peter-Grünberg-Institut, Forschungszentrum Jülich.

This is followed by the description of the structural characterization of microdisks via SEM. Special focus is put on the extraction of deformation functions of disks from SEM images.

The optical characterization of resonators was conducted using μ PL. The setups used for measurements at cryogenic and room temperatures are introduced here.

The main theoretical aspects of this work stem from calculations done by Jan Wiersig at the Universität Magdeburg with the boundary element method described in Section 2.3.2. Additional calculations were made by the author using a FDTD formalism via the open-source *Meep* software. Therefore, the use of this software is described at the end of this section.

4.1. Growth and Processing of Microdisks

All samples analyzed in this work were fabricated in the group of Alexander Pawlis at the Peter-Grünberg-Institute, Forschungszentrum Jülich.

The fabrication process starts with the growth of layers by molecular beam epitaxy (MBE), before the samples are structured into resonators of different geometries. For MBE growth, atoms or molecules are evaporated in an ultra high vacuum chamber. Due to the vacuum, the resulting material beams have a long mean free path and can travel to the substrate at which their effusion chambers are directed, without interaction with other species. The particles are then adsorbed on the substrate and can move on it. Finally, growth takes place when the adsorbates chemically bond to the substrate or other materials already deposited there. Using this growth method, a high control over the sample composition and layer thickness can be achieved, as the effusion cells can be opened and closed by shutters in a fraction of a second. Additionally, growth rates can be precisely monitored in situ, e.g., by electron scattering (RHEED). Besides that, low defect concentrations due to the slow growth in vacuum and a good crystal quality can be achieved.

Heteroepitaxial growth, i.e., the growth of a material on a substrate from a different material, is strongly influenced by the difference Δa between the lattice parameters of the

substrate and the growth material. This difference induces strain into the grown epilayer, which leads to island growth (as for example used in the fabrication of quantum dots), dislocations, or makes growth impossible, depending on the size of Δa .

The microdisks discussed in this work were grown on (100)-GaAs substrates. At first, an additional layer of GaAs was deposited, followed by a 10 nm-thick ZnSe buffer layer; these layers are introduced in order to improve the growth quality of the following layers. For microdisks in the supported geometry, an AlAs interlayer ($d_{\text{AlAs}} = 200$ nm) is added between the GaAs and ZnSe. On top of these layers two 30 – 40 nm-thick $\text{Zn}_{1-x}\text{Mg}_x\text{Se}$ barriers which embed a 4 nm-thick $\text{Zn}_{1-y}\text{Cd}_y\text{Se}$ QW (for supported disks $y = 0$) are fabricated. The QW was doped with halogens, fluorine was used in free-standing and Cl in supported microdisks. In some samples the doping profile is δ -type, meaning that only a small amount of halogen atoms were incorporated into the structure in the center of the QW by opening the respective shutter for a short amount of time. The growth parameters of all samples can be found in Table 4.1.

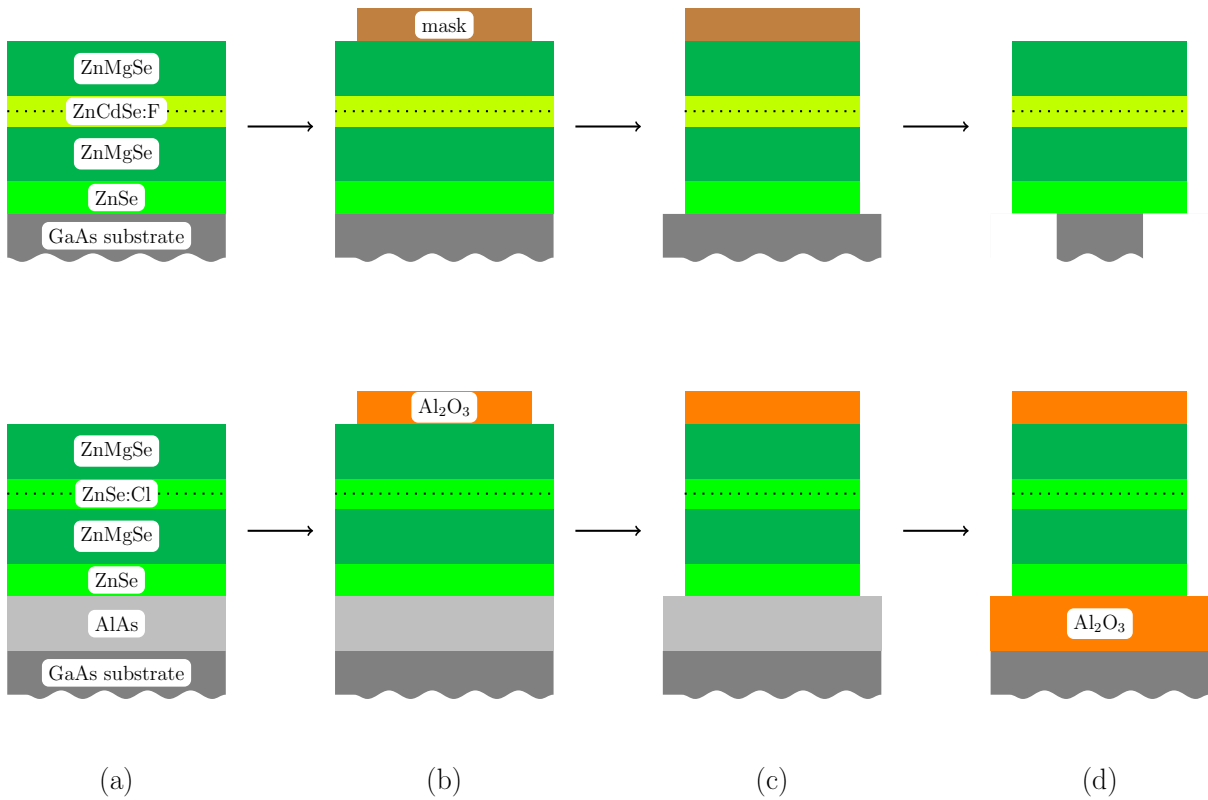


Figure 4.1: Illustration of the fabrication of free-standing (top row) and supported (bottom row) microdisks from MBE grown layerd structures. (a) as-grown layers (b) after e-beam lithography (c) after reactive ion etching of the ZnSe-based material (d) free-standing disks: after mask removal and underetching, supported disks: after oxidation of the AlAs layer.

The MBE grown layers are structured into microdisks of either the free-standing or supported geometry in a ‘top-down’ approach as illustrated in Figure 4.1. Starting from the as grown material (4.1a) the positions and diameters of microdisks were defined by masks fabricated using electron beam lithography (4.1b). A negative resist is used to form the mask for free-standing samples; this is transferred to an Al_2O_3 mask for microdisks to be fabricated in the supported geometry. This is done to ‘sandwich’ the ZnSe-based structure in Al_2O_3 after fabrication. Reactive ion etching was used to remove the excess ZnSe-based material and form the actual microdisks (4.1c). In the final fabrication step, free-standing disks were undercut by a wet-chemical etch of the GaAs substrate. For supported disks, the AlAs interlayer was oxidized to Al_2O_3 [112] (4.1d). This increases the refractive index contrast between the microdisk and the III-V semiconductor material below it, which increases the confinement of light in the structure due to lower scattering losses into the substrate [68,113]. Additionally, the aforementioned ‘sandwich’ is completed, from which an improvement of the overlap between the gain medium (QW) and the field of the resonating modes is expected [89,105].

The oxidation of an AlAs underlayer is a new approach to the fabrication of microdisks. A similar process has been used to control the growth position of quantum dots in III-V materials, known as the ‘buried stressor approach’ [114]. There, the strain induced by the partial underoxidation of a mesa structure ensures growth of a quantum dot in the middle of the mesa. Given that a uniform strain and refractive index contrast are desirable for our microdisks, they are fully underoxidized.

In this work, results obtained from the analysis of three different samples, named A, B, and C, are discussed in Sections 5.1, 5.2, and 5.3, respectively. Their geometries and compositions can be found in Table 4.1.

sample	geometry	d_{barrier}	x (Mg)	y (Cd)	QW dopant, concentration
A	free-standing	32 nm	16 %	21 %	F, $3 \cdot 10^{18} \text{ cm}^{-3}$
B	free-standing	30 nm	18 %	15 %	F (δ -type), $3 - 4 \cdot 10^{16} \text{ cm}^{-3}$
C	supported	36 nm	9 %	0 %	Cl (δ -type), $3 - 4 \cdot 10^{16} \text{ cm}^{-3}$

Table 4.1: Growth and fabrication parameters of the samples analyzed in this work, including barrier thickness d_{barrier} and Mg/Cd content in the barrier/QW.

4.2. Structural characterization using Scanning Electron Microscopy

A scanning electron microscope (SEM) was used by the author to take images of the analyzed samples in order to judge the success of various processing steps as well as to

obtain information about the structural properties of the disks (e.g., their radius r and deformation function $r(\varphi)$).

4.2.1. Operational Principles of the SEM

The SEM of a dual system scanning electron microscope with focused ion beam *Nova NanoSEM* from manufacturer *FEI* situated at the Institute of Solid State Physics at the University of Bremen was used for the structural characterization of the samples presented in this work. The operating principle of this setup is shown in Figure 4.2a. Electrons are emitted from a Schottky-type field emission gun (FEG) and accelerated in the field of an anode with a voltage of 2 kV. Electromagnetic lenses focus the electron beam into the deflection system and onto the sample surface, over which the beam is scanned.

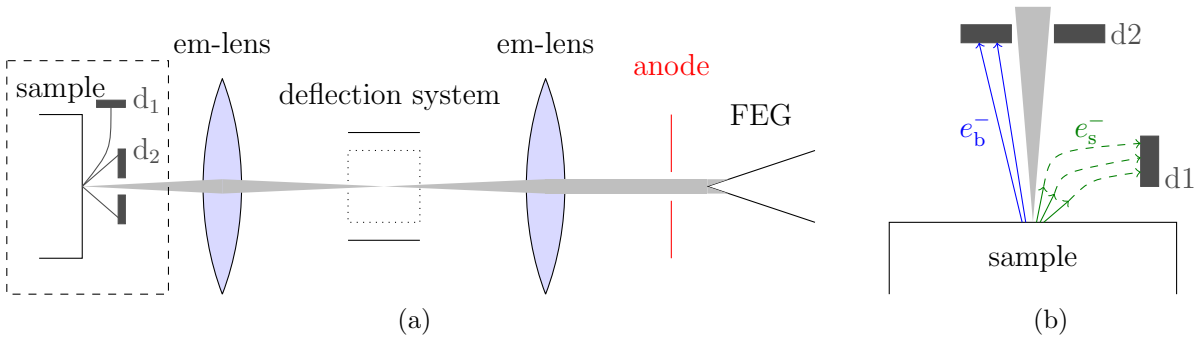


Figure 4.2: Sketch of (a) the setup and operating principle of a scanning electron microscope, illustrating the electron beam in light gray. Electromagnetic lenses are depicted here by classical lenses. Secondary electrons are collected in detector d1, backscattered electrons in detector d2. (b): Detailed sketch of the detection process. Backscattered electrons are shown in blue, high energy and therefore velocity brings them directly into the detector d2. Secondary electrons (green) have lower energy and are emitted in more directions. To increase the signal-to-noise ratio, an additional field can be applied to funnel secondary electrons into the detector d1 (indicated by dashed arrows).

The signal, which is used to create a gray-scale image of the sample, can be obtained by detecting either secondary or backscattered electrons as a function of the position of the beam on the sample. The two detection mechanisms are shown in Figure 4.2b.

Secondary electrons are generated when the incident ‘primary’ electrons transfer a part of their energy to electrons in the sample either by direct scattering or indirectly via the Auger process. During the latter, a tightly bound electron is removed from its orbital after scattering with a primary electron. The free orbital site is then filled by an electron stemming from a higher shell. The excess energy is transferred to a third electron (the

Auger electron) in the sample, which then has sufficient energy to escape from the crystal. The energy of secondary electrons is in the order of up to 50 eV which gives them a mean free path of only a few tenths of nanometers in the sample material. Therefore, secondary electrons can only escape the sample when they originate from an atom near the surface and images based on the detection of secondary electrons are very surface sensitive. This shows that the contrast of such images is mainly given by the morphology of the sample. Opposed to that, backscattered electrons are primary electrons that interact with the sample and are scattered back towards their origin. These electrons have significantly higher energy compared to secondary electrons (up to the primary electron energy of 2 keV). Because of that, this detection method is less sensitive to the morphology of the sample, the amount of backscattered electrons is more strongly dependent on the number of electrons in the sample. This gives this method a strong material contrast.

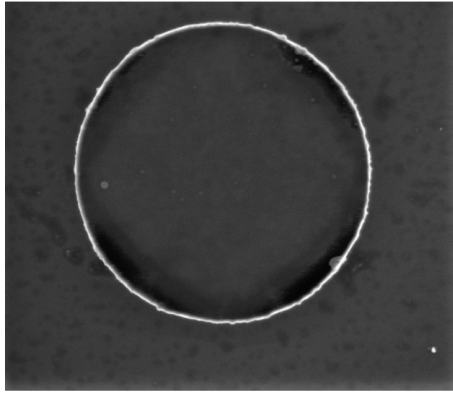
In this work, the SEM is used to analyze the morphology of samples and gather information on the structure of the examined resonators. Special focus was put on the roughness of the microdisk's edges which was determined in the form of a deformation function $r(\varphi)$ of the disk as described in Section 4.2.2. For these applications, the detection of secondary electrons was used and enabled the resolution of layers with a thickness below 100 nm as well as the extraction of structural parameters of resonators from the images with an estimated error of ± 0.2 nm.

4.2.2. Extraction of deformation functions from SEM images

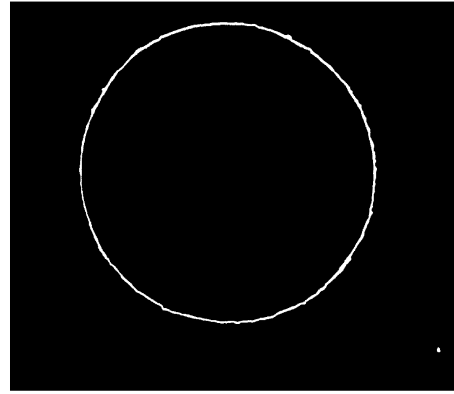
An algorithm was developed by the author to extract the deformation function $r(\varphi)$ of microdisks from top-view SEM images for both free-standing and supported structures. These deformation functions are then used as input parameters to model the WGMs propagating in the microdisks with the boundary element method. This represents the first time that microscopy of a microdisk resonator is used to extract the full deformation function, which is later used for theoretical calculations. Previous studies only extracted statistical information on the deformation of resonators from microscopic images [17, 83]. Additionally, information on disk roughness is for the first time correlated with optical measurements of the resonator quality of the same microdisk in this work.

The processes developed to extract $r(\varphi)$ are similar for both microdisk geometries, but require some adjustments, as the disks appear slightly different in the SEM images.

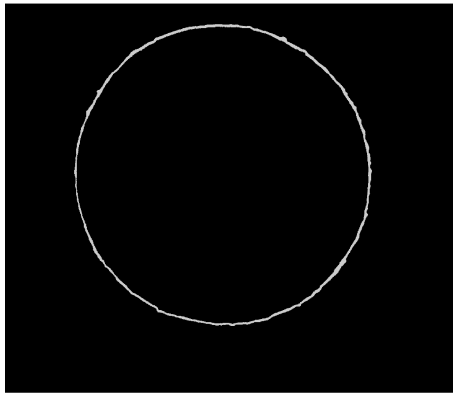
Figure 4.3a shows a typical top-view SEM image of a free-standing microdisk with a diameter of $3.8 \mu\text{m}$. The scale bar is not given in this image since it illustrates the raw SEM data with which the algorithm explained below works. However, the width of each pixel is known from the output of the SEM. In the secondary electron image, the edge



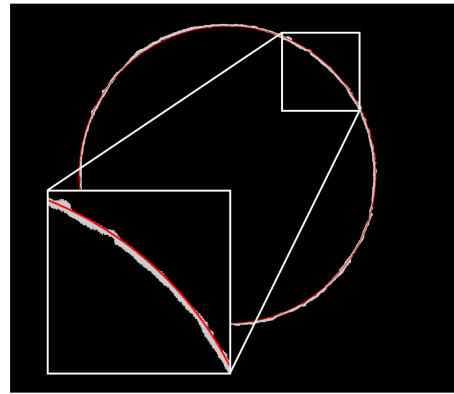
(a) Typical SEM image of a free-standing microdisk.



(b) Binary image created by thresholding.



(c) Disk edge selected from the binary image.



(d) Disk edge and fit with an ideal circle (red).

Figure 4.3: Illustration of the process of extracting the deformation function from a SEM image for a free-standing microdisk with a diameter of $3.8 \mu\text{m}$.

of the free-standing disk appears bright in comparison to the central region of the disk and the substrate, because more secondary electrons can escape from the sample where its local surface-to-volume ratio is high. This strong morphology contrast of secondary electron imaging was explained in Section 4.2.1, it plays a central role in the determination of the deformation function.

The first step of this process is to select a brightness threshold th and create a binary image based on pixel value ($px > th$ (possibly disk edge) or $px \leq th$ (not disk edge)). th is selected such that the edge of the disk visible in the binary image forms a complete circle, but is chosen to be as low as possible in order to avoid wrongly labeling parts of the disk or background as ‘possibly disk edge’. The binary image created from Figure 4.3a can be seen in Figure 4.3b. As can be seen in the bottom-right corner of this image, irregularities on the sample can be wrongly labeled as ‘possibly disk edge’. To circumvent this problem,

the largest connected area of ‘possibly disk edge’ pixels is defined as the disk edge and the other pixels are discarded (Figure 4.3c). In the final step, the disk edge is then fitted with an ideal circle as depicted in red in Figure 4.3d. The radius of this fitted circle is the average radius \bar{r} of the disk. The actual disk edge can be extracted from the image based on the scale given by the SEM and converted into the deformation function as described below.

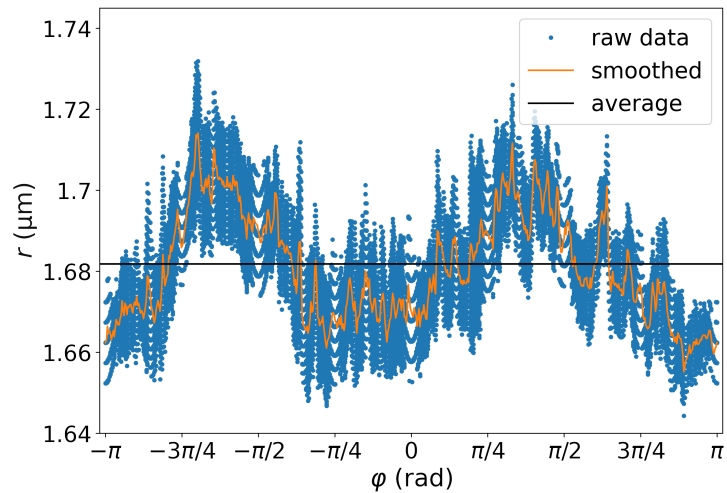


Figure 4.4: Deformation data extracted from the free-standing microdisk in Figure 4.3. The image shows the raw data (blue dots) as well as smoothed data (orange line) used as input for modeling with the boundary element method. The average radius of the disk is marked in black for comparison.

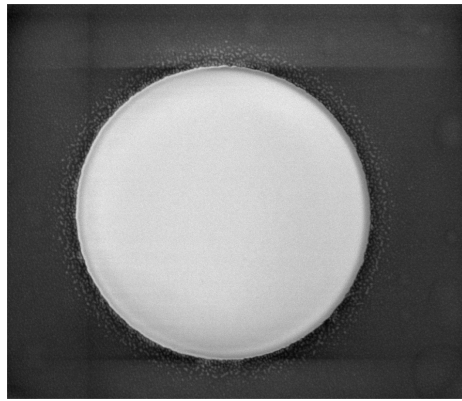
Figure 4.4 displays the raw data points of the disk edge extracted from the SEM image (Figure 4.3) in blue and the data after averaging into non-overlapping bins with a width of 0.01 rad (orange line) in polar coordinates ($r(\varphi)$). The average radius is marked in black for orientation but is not relevant for the calculation of $r(\varphi)$.

The raw data scatters strongly, because the edge of the free-standing microdisk cannot be clearly extracted from the top-view SEM data. This is why the data was smoothed by averaging into non-overlapping bins before it was used as input parameter for theoretical calculations with the boundary-element method (Section 2.3.2). From Figure 4.4 it can be seen that this smoothing step is justified, since all the features visible in the raw data are reproduced, e.g., the two close and narrow maxima of the radius between $\frac{\pi}{2}$ and $\frac{3\pi}{4}$.

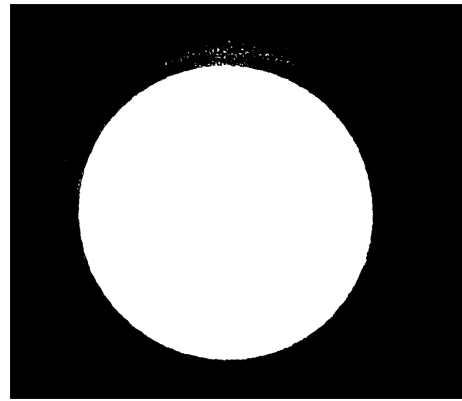
For the quantification of the microdisk’s edge roughness and deviation from an ideal circular shape, this data does not need to be smoothed. Therefore, the raw data was used in order to achieve the highest possible accuracy in these calculations.

Given that the raw data appears in several parallel running ‘lines’, it is obvious that not just one but several rows of pixels were labeled as ‘disk edge’ in the process described

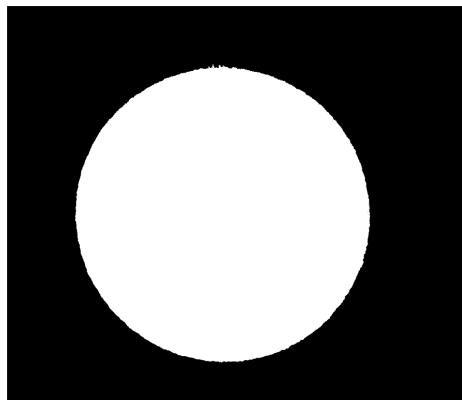
above. Averaging the data was chosen over the selection of one of the pixel rows (e.g., the outer- or innermost), since it is not clear from the SEM image where exactly the edge of the microdisk is positioned. Consequently, using only the outer or inner row of pixels could lead to a over- or underestimation of the radius, while also reducing the accuracy with which edge roughness is detected. Using the central row of this ‘disk edge’ labeled pixels would lead to similar results like the smoothing described above, but this likewise would reduce the accuracy of the process as only a single row of datapoints is more susceptible to noise. Additionally, the center row might be hard to determine.



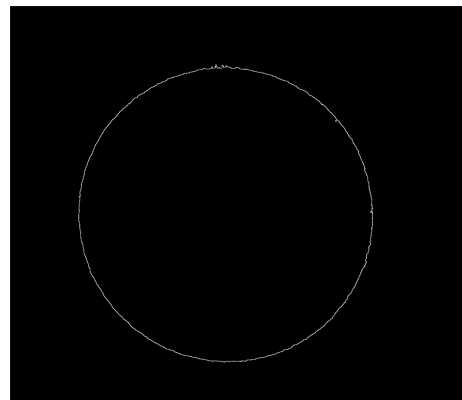
(a) Typical SEM image of a supported microdisk.



(b) Binary image created by thresholding.



(c) Image of the disk selected from the binary image.



(d) Disk edge extracted from the selected image.

Figure 4.5: Illustration of the process of extracting the deformation function from a SEM image for a supported microdisk with a diameter of $4.0 \mu\text{m}$.

The process of finding the disk edge in top-view SEM images of supported disks is similar to the process for free-standing disks shown in Figure 4.3, but requires some changes due to the different SEM depiction of these disks:

A typical SEM image of a supported disk can be seen in Figure 4.5a. The disk appears bright against the darker background of the oxidized AlAs underlayer. This contrast cannot be explained by the morphology of the sample, as the disk rests flat on the substrate. It is therefore based on the material, the ZnSe-based disk produces a higher number of secondary electrons compared to the Al_2O_3 . As described above, a material contrast is usually better observed in the backscattered electron detection setup. However, the secondary electron detection has a higher surface sensitivity, which is why it leads to a higher contrast for thin films like the disks analyzed here. Similar to the extraction algorithm for free-standing disks described above, a binary image is created via thresholding. Here th is chosen to be as low (dark) as possible, without mislabeling part of the disk as background. This leads to a binary background / disk image as seen in Figure 4.5b. Again, a selection step is necessary to separate the actual disk from noise in the image caused by irregularities on the substrate. For this, all ‘disk’-like pixels which are not part of the largest connected area of ‘disk’ pixels are eliminated. The result of this step is shown in Figure 4.5c. The edge of the disk is then found by deleting all the ‘disk’ labeled pixels whose 4 nearest neighbors and 4 diagonal next-nearest neighbors are ‘disk’ pixels, too. The result of this step is presented in Figure 4.5d. The extracted disk edge is very narrow and a distinction between a fit with an ideal circle and the measured disk edge data would not be possible in many parts of the image. Due to this, the fit is not included there.

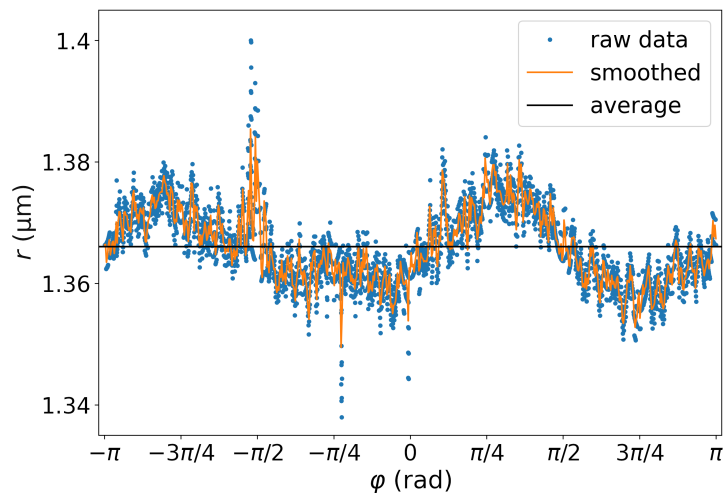


Figure 4.6: Deformation data extracted from the supported microdisk in Figure 4.5. The image shows the raw data (blue dots) as well as smoothed data (orange line), the average radius of the disk is marked in black for comparison.

Figure 4.6 displays raw data extracted from Figure 4.5d along with data smoothed by an averaging into non-overlapping bins with a width of 0.01 rad. Since the disk edge extracted from SEM images is narrower for supported disks in comparison to free-standing

resonators, the raw data scatters less. However, smoothing the data still leads to a clearer image of the edge of the disk and reduces the influence of noise, as can be seen near $\frac{-\pi}{2}$ and 0, while features of the deformation data are preserved. Since no boundary-element method calculations were performed on supported resonators, all roughness data presented for disks in this geometry was calculated based on the raw data (blue dots in Figure 4.6).

4.3. Micro-Photoluminescence Measurements

Micro-photoluminescence (μ PL) measurements are used in this work to gain information on the optical properties of the microdisks. The light emitted from them provides an insight into the optically excitable states in the materials. Additionally, the measurement of the WGMs that occur in the spectrum yields information on the optical properties of the fabricated microdisks. The μ PL measurements will reveal which modes of the disks exist in the emission range of their quantum well and measure their spectral, i.e., energetic, position and line width. The former can be used to determine the exact modes which travel inside the resonator by comparison with theoretical calculations. The latter is a measure for the optical quality of the resonator, determining how large losses in the resonators are. For μ PL experiments the sample is optically excited, typically with a laser with a small wavelength, i.e., a high photon energy. Exciting photons can be absorbed by electrons in the sample material, enabling them to jump to higher energy levels from their ground state. In semiconductor materials this typically means excitation across the bandgap. The exciting light source is usually not in resonance with the excitable states, excess energy is dissipated as heat. The free charge carriers created by this (electrons in the conduction band and holes in the valence band) can then move through the material, usually to energetically favorable spaces (e.g., the material with a smaller bandgap in a double heterostructure as described in Section 2.2.1), form excitons and/or be trapped at defects. When the electrons and holes recombine, the energetic difference can be emitted as a photon, the ‘luminescence’ of the sample. The energy of the emitted photon corresponds to the energetic difference between the excited and ground states. Therefore, this measurement can be used to obtain information on the bandgap as well as exciton or trapped carrier binding energies. Because the luminescence is detected after optical excitation of the sample, it is called photoluminescence. If the exciting light is focused onto a small spot on the sample in order to analyze small structures on it, this method is called micro-photoluminescence.

The μ PL setup used for low-temperature measurements in the working group of professor Jürgen Gutwoski at the University of Bremen is schematically shown in Figure 4.7. The setup that is employed in μ PL experiments at room temperature will be described at

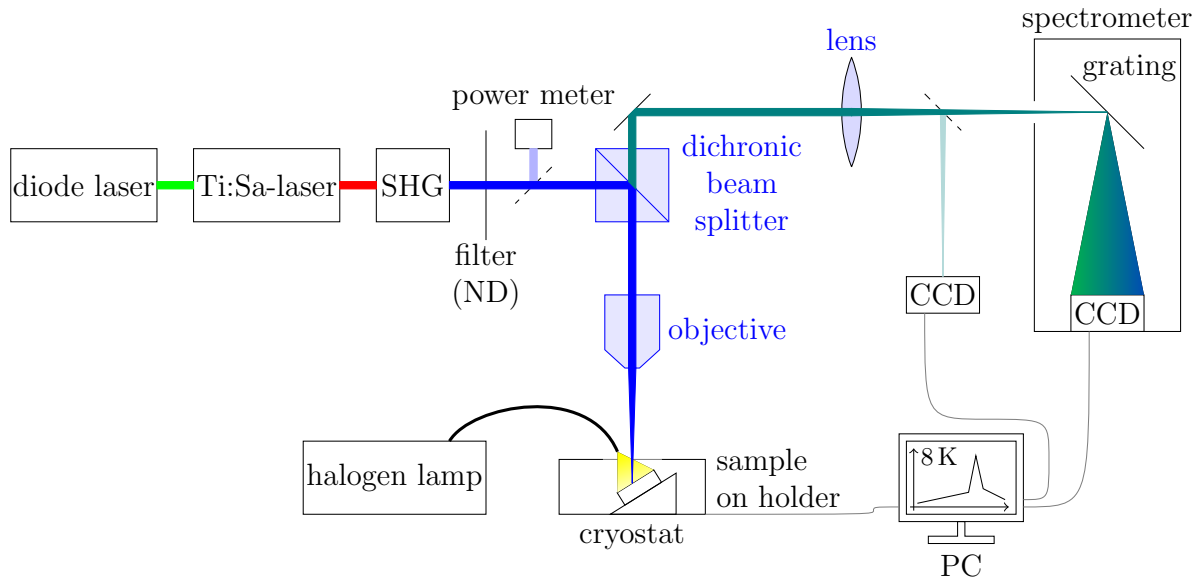


Figure 4.7: Schematic setup of the μ PL setup operated for the low-temperature μ PL measurements presented in this work. Filter (ND) denotes a neutral density filter wheel.

the end of this section. These experiments were conducted in the group of professor Martin Eickhoff, likewise at the University of Bremen, the setup was operated by Christian Tessarek, instructions for the measurements were given by author.

The low-temperature setup utilizes a *Spectra Physics Tsunami* Ti:Sa laser system, in which the *Millennia* green diode laser acts as the pump. The pulses emitted by the Ti:Sa laser are frequency-doubled using a BBO crystal, which is also part of the laser system. This leads to short (100 fs) pulses with a high repetition rate (81 MHz) in the blue to ultraviolet spectral region (usually with a central wavelength of about 380 nm and a FWHM of about 15 nm). These short pulses excite the sample. The intensity of the exciting laser is regulated by means of a neutral density filter wheel and measured using an *Ophir Orion-PD* powermeter.

A *Beck Optronik* reflective microscope objective with a 36-fold magnification, a numerical aperture of 0.5 and a working distance of 8.6 mm (*Model No 5004*) focuses the light onto the sample surface. A spot diameter of $5\ \mu\text{m}$ is technically feasible. The sample is placed inside a *CryoVac KONTI* He-flow cryostat, where it is kept in a vacuum and can be cooled to the boiling point of helium (4 K). The cryostat is mounted on piezoelectric stages from manufacturer *PI* that can be moved in increments of about 100 nm to allow for an exact positioning of the laser spot on the sample. Due to the fact that WGMs emit in-plane with the sample surface [36], more of their intensity can be observed if the sample is placed on a sample holder at an angle of 32° as shown in Figure 4.7. This angle is limited by the

working distance of the microscope objective, as it must be possible for the whole sample to be in focus during measurements.

The luminescence of the sample is collected by the microscope objective and reflected towards the detection setup by the dichronic *BrightLine FF409* beam splitter fabricated by *Semrock*. This beam splitter only reflects light with wavelengths above its transmission edge at 409 nm and therefore filters the backscattered laser light to allow for a better detection of the luminescence. Behind the beam splitter, the light is focused into the *HORIBA HR320* grating-based spectrometer, which is operated to obtain a wavelength-resolved image of the luminescence on a *Princeton Instruments (Model 7524-0003)* CCD sensor. This sensor has 2048 x 512 pixels, with a size of 13.5 μm x 13.5 μm each. It is cooled to -120°C by liquid nitrogen in order to reduce the noise caused by dark current. The combination of a grating with 1200 grooves per mm in the monochromator and the dimensions of the CCD array yield a resolution of about 0.02 nm.

Additionally, it is possible to insert a mirror into the beam path, deflecting the light onto a CCD array camera (*Basler aCA1300-20um*). A magnified image of the sample is obtained in this path that can be employed to control and adjust the position of the laser spot on the sample. Furthermore, with the use of a halogen lamp as a white light source illuminating the sample in the cryostat via a gooseneck, it is possible to navigate the sample with this image. The white light is not integrated into the beam path of the laser, but enters the cryostat at an angle, as this leads to a better illumination of the tilted sample.

For room temperature μPL measurements of supported microdisks presented in this work, the sample was excited using the 325 nm emission line of a *3552RG* He-Cd laser from *KIMMON*. This measurement is based on the same operation principle like the setup shown above, differences being that the sample was not placed in a cryostat under an angle, but was oriented perpendicular to the exciting laser beam under ambient conditions (room temperature and pressure). The positioning of the sample and detection of emission was performed utilizing the *Horbia LabRAM Evolution* optical spectroscopy setup which allows for measurements over a large spectral range (325 to 660 nm) with a resolution of 0.4 nm.

4.4. FDTD simulations using Meep

As discussed in Section 2.3.1, FDTD simulations to calculate the frequency of a mode propagating in a resonator rely on a broad excitation pulse. After the excitation has faded, the signal at a fixed point in the resonator is recorded and transformed into the frequency domain, where harmonics can be identified. In a second step, the electric field

corresponding to a single mode can be imaged. For this, a narrow excitation peak is created, which only excites the mode to be analyzed. After the excitation has faded, the remaining oscillating field can be recorded.

In this work, the open-source FDTD implementation *Meep Version 1.17* was used by the author in order to calculate the spectral positions of modes in an ideally circular microdisk and image their fields for a comparison with calculations performed by Jan Wiersig (Universität Magdeburg) that included the surface roughness of the analyzed resonators.

In order to obtain reliable results, a number of simulation parameters need to be chosen carefully. This includes the length of the space outside of the microdisk that is included in the simulations, as well as the depth of the absorbing boundary (to avoid artifacts from backscattering of fields emitted from the resonator, compare Section 2.3.1) around the simulated area. The spacing was chosen to be $1\ \mu\text{m}$ followed by perfectly matched layers (PML) with a thickness of $0.5\ \mu\text{m}$; these relatively small values were chosen in order to minimize the area that is simulated and therefore reduce the run time of the calculation. A series of calculations with larger spacing and PML thickness resulted in no change of the calculated mode energies.

Choosing the resolution of the simulation is a trade-off between accuracy and computational expense. 200 pixels per μm was used in the simulations presented in this work, corresponding to about 400 pixels per wavelength.

The spot of the excitation pulse and subsequent frequency extraction analysis should not be in a node of the field of a resonating mode. To avoid this, simulations were run with excitation and detection at different distances from the disk edge (due to the rotational symmetry of the disk, only the radial axis needs to be taken into account). The results presented in this work were obtained with excitation and detection at $r_{\text{disk}} - 0.25\ \mu\text{m}$.

Good results were observed from the frequency analysis if it ran over 500 time units, corresponding to about 1000 periods of the calculated WGM frequencies.

The average radius of the analyzed microdisk extracted from SEM images (see Section 4.2.2) was used as r_{disk} in this analysis. The (effective) refractive index of the microdisk was set to $n = 2.61$, which is the same value used in the calculations performed by Jan Wiersig.

5. Results and Discussion

In this section, the results obtained from the characterization of microdisk resonators with the methods described in Section 4 are presented and discussed.

The section starts with the analysis of free-standing microdisks with a fluorine-doped QW/barrier structure (sample A). These resonators enable stimulated emission into WGMs; the modes are theoretically confirmed by calculations mainly performed by Jan Wiersig from the Universität Magdeburg. Our analysis finds that the optical quality of the resonator correlates to its edge roughness.

Subsequently, the fluorine-dopant concentration is reduced to δ -type doping in the QW (sample B), which is interesting for several applications detailed in Section 3.1. The resulting disks are then characterized in micro-photoluminescence. In addition to WGMs that are similar to those observed for disks with high dopant concentrations, modes at low excitation densities appear on the low-energy side of the emission. For WGMs at high excitation densities, mode intensity degrades under continuous excitation.

In the final part of this section, microdisk resonators in the supported geometry (sample C) are discussed. Similar to free-standing δ -doped disks on sample B, modes are observed on the low-energy side of the emission at low excitation densities. A large number of WGMs is observed on the defect emission band at room temperature. The structural analysis based on SEM images demonstrates a good structural quality of the supported microdisks.

5.1. Free-standing Microdisk Resonators

Here, the results obtained from sample A (for an overview of all samples used for measurements in this work see Table 4.1 on page 31) are analyzed. Microdisks with a 4 nm $\text{Zn}_{0.79}\text{Cd}_{0.21}\text{Se:F}$ QW embedded in 34 nm thick $\text{Zn}_{0.84}\text{Mg}_{0.16}\text{Se}$ barriers as optically active materials were fabricated. The concentration of the fluorine embedded in the QW as dopant is $3 \cdot 10^{18} \text{ cm}^{-3}$. Under optical excitation, strong modes can be observed in their emission spectra, theoretical calculations confirm that these modes are WGMs. The analysis of SEM images reveals that microdisks with a lower edge roughness show higher Q -factors.

5.1.1. Experimental Observation of Stimulated Emission into Whispering Gallery Modes

Figure 5.1 shows a series of μPL spectra taken at cryogenic temperature (8 K) from a free-standing microdisk with a diameter of $3.8 \mu\text{m}$. The spectra were recorded while rising

the power of the exciting laser, the excitation density is given in the legend. A more saturated color in the plot corresponds to a higher excitation density.

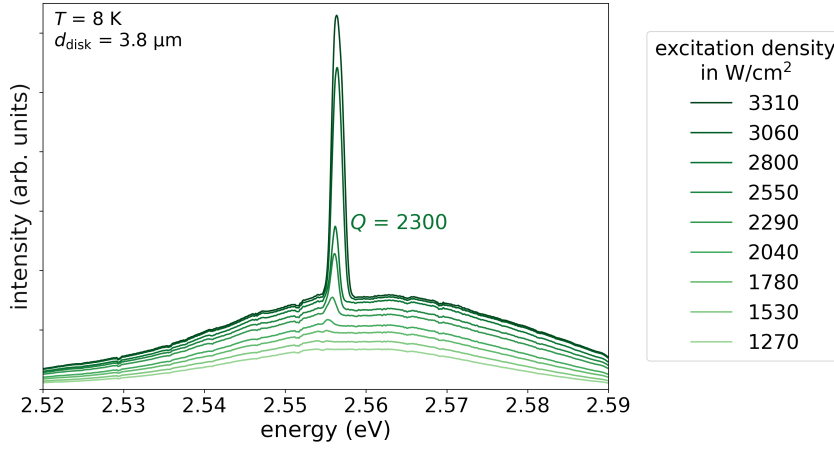


Figure 5.1: Series of μ PL spectra with rising excitation density of a free-standing microdisk with a diameter of $3.8 \mu\text{m}$. The Q -factor of the mode with highest Q is indicated in the figure.

These μ PL spectra exhibit a broad emission from the QW embedded in the microdisk between 2.53 eV and 2.59 eV . With rising excitation (above $2000 \frac{\text{W}}{\text{cm}^2}$), a single mode appears on the background band at about 2.557 eV .

The apparently strong increase of the intensity of the mode could be an indicator for the onset of lasing in the resonator. In order to get a better insight into the properties of the mode, it was fitted with a Gaussian to which a linear background was added, this evaluation provided values for the mode's intensity, spectral position, and width as a function of excitation density. From its width, the Q -factor of the mode was calculated for all measured spectra. The highest value that was obtained in this analysis is annotated in Figure 5.1, i.e., $Q = 2300$ for an excitation density of $2800 \frac{\text{W}}{\text{cm}^2}$. Figure 5.2 shows the integrated intensity of the mode plotted against the excitation density.

The integrated intensity of the mode in Figure 5.1 is very low at excitation densities lower than $2000 \frac{\text{W}}{\text{cm}^2}$. After that, a linear increase up to about $2800 \frac{\text{W}}{\text{cm}^2}$ can be seen. For this excitation density the highest Q -factor has been observed, as noted in the annotation in Figure 5.1. At excitation powers above this, the mode's intensity continues to increase with a greater slope compared to the linear increase found below $2800 \frac{\text{W}}{\text{cm}^2}$.

Such a threshold in the emission intensity can be a sign for the onset of lasing in the structure. For excitation densities higher than measured in this experiment, a reduction of the rate of intensity growth back to the linear increase would be expected, forming a 's-shape' in the input/output power characteristic. This could not be measured for this microdisk, because of degradation under strong and prolonged optical excitation. This

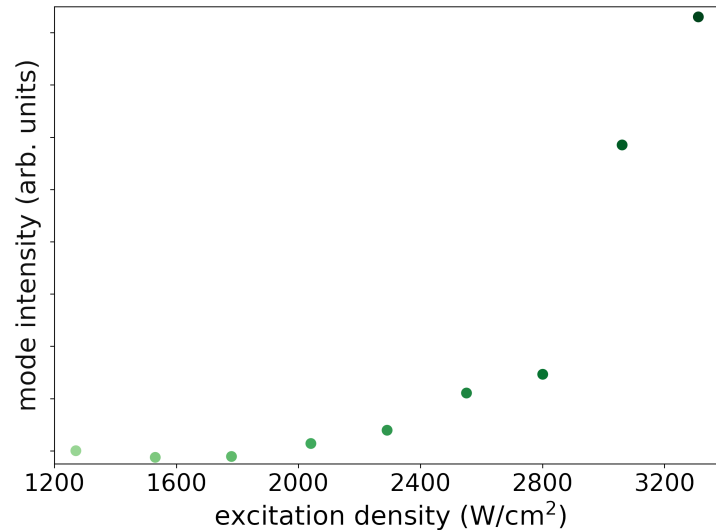


Figure 5.2: Integrated intensity of the mode observed in Figure 5.1 as a function of excitation density. The color scheme of the dots is identical to the scheme in Figure 5.1.

problem will be addressed in more detail in Section 5.2.2.

The nonlinear increase of intensity at the lasing threshold is also typically accompanied by a decrease in line width as stimulated emission outweighs spontaneous emission. Figure 5.3 shows the spectral position and FWHM of the mode as a function of excitation density.

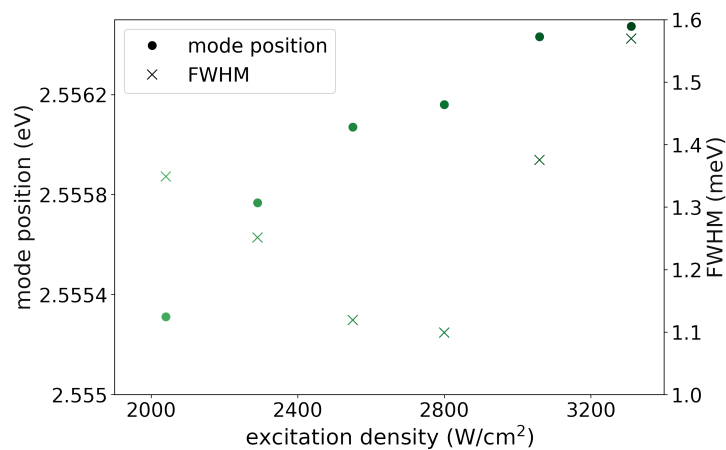


Figure 5.3: Spectral position (circles, left axis) and FWHM (crosses, right axis) of the mode observed in Figure 5.1 as a function of excitation density. The color scheme of the markers is identical to the scheme in Figure 5.1.

In Figure 5.3, a smaller range of excitation densities is shown compared to Figure 5.2. This is because the mode is practically non-existent below $2000 \frac{\text{W}}{\text{cm}^2}$ (compare the low integrated intensities in Figure 5.2), which is why the fitting algorithm cannot determine

reliable values for the position and width of the Gaussian above the background.

A continuous blue-shift of the mode with rising excitation density can be seen. In total, the mode shifts by about 1.1 meV between $2000 \frac{\text{W}}{\text{cm}^2}$ and $3400 \frac{\text{W}}{\text{cm}^2}$. The full width at half-maximum of the mode continuously decreases between $2000 \frac{\text{W}}{\text{cm}^2}$ and $2800 \frac{\text{W}}{\text{cm}^2}$. This is the range of excitation that shows a linear increase of mode intensity in Figure 5.2. At higher excitation densities the mode width strongly increases.

The blue-shift of the mode could be caused by a carrier induced change of the refractive index, which has been observed in ZnSe-based QW structures [115] and microdisks [65]. Similar effects have been reported in microdisks fabricated from other materials [86, 116]. The reduction of the FWHM and simultaneous increase of the mode intensity between $2000 \frac{\text{W}}{\text{cm}^2}$ and $2800 \frac{\text{W}}{\text{cm}^2}$ are a clear sign for the onset of stimulated emission into the mode. The strong increase in the FWHM of the disk above $2800 \frac{\text{W}}{\text{cm}^2}$ might be a first sign of the aforementioned degradation that the free-standing resonators exhibit under optical excitation with high power densities as will be discussed in detail in Section 5.2.2.

Similar modes to the one discussed here were observed in other measurements of disks of several sizes. In some measurements more than one mode could be observed at the same time. As an example for this, Figure 5.4 shows a μPL spectrum of another disk with a diameter of $3.8 \mu\text{m}$ under excitation with the highest excitation density used in Figure 5.1.

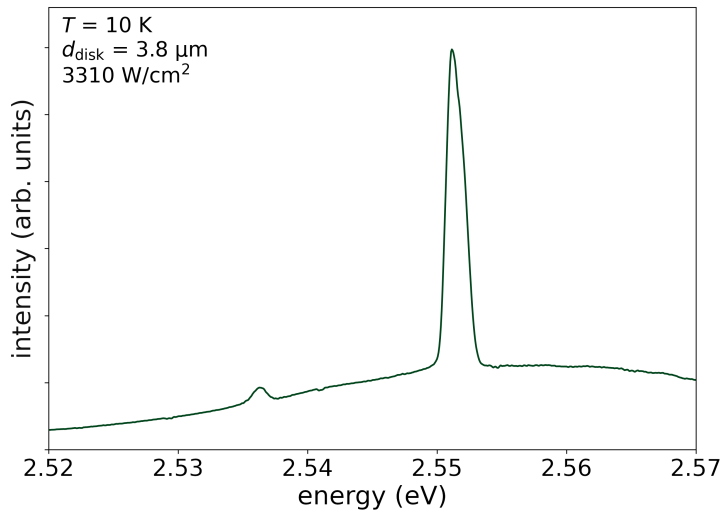


Figure 5.4: μPL spectrum of a free-standing microdisk with a diameter of $3.8 \mu\text{m}$. The excitation density is the same as the highest value used in 5.1, but a different disk is analyzed in this figure.

The spectrum is comparable to what can be observed in Figure 5.1 at the same excitation density (the size of the analyzed disk is the same). This spectrum is dominated by a

central mode between 2.55 and 2.56 eV, too. Additionally, a less intense mode can be seen on the low-energy side of the QW emission at about 2.538 eV.

In the following, measurements on disks of other sizes will be presented, starting with a diameter of 3.3 μm , see Figure 5.5.

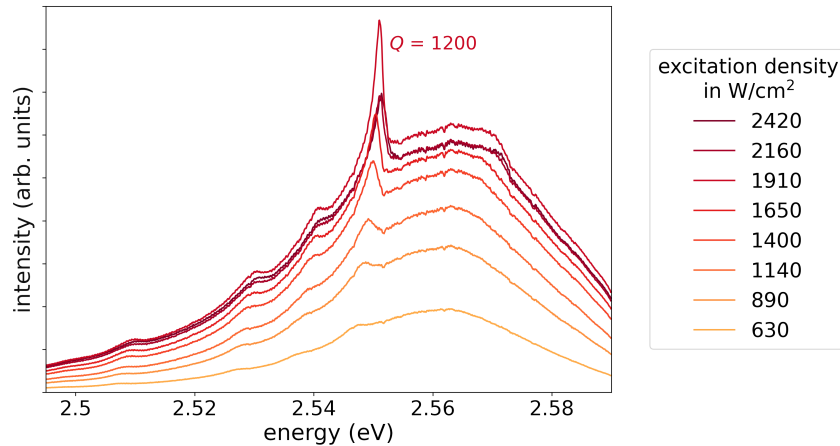


Figure 5.5: Series of μPL spectra with rising excitation density of a free-standing microdisk with a diameter of 3.3 μm . The Q -factor of the mode with highest Q is indicated in the figure.

A total of four modes can be found on the low-energy side of the QW emission. The mode closest to the center of the background QW emission (near 2.55 eV) shows clear growth. However, in contrast to Figure 5.1, the intensity of the mode is maximal at an excitation density of 1920 $\frac{\text{W}}{\text{cm}^2}$, at higher excitation the intensity is reduced. Additional smaller modes can be seen at 2.51 eV, 2.53 eV, and 2.54 eV.

In comparison to the microdisk with a diameter of 3.8 μm analyzed above, the smaller disk might exhibit stimulated emission at lower excitation densities, as less material needs to be excited. On the other hand, degradation could occur at lower excitation densities for the same reason. For the three modes that do not show a strong increase of intensity in this measurement, the material gain probably is too low at their spectral positions to support stimulated emission. In order to analyze this further, the mode near 2.55 eV was fitted with a Gaussian, as done for the analyses in Figures 5.2 and 5.3. The results can be seen in Figures 5.6 and 5.7.

Figure 5.6 shows the integrated mode intensity as a function of excitation density. A continuous increase of the intensity can be seen over the whole measurement range up to the maximum near 2000 $\frac{\text{W}}{\text{cm}^2}$, which was already mentioned in the discussion of the spectra above. After the mode intensity reaches its maximum, a clear reduction can be observed, followed by stagnation.

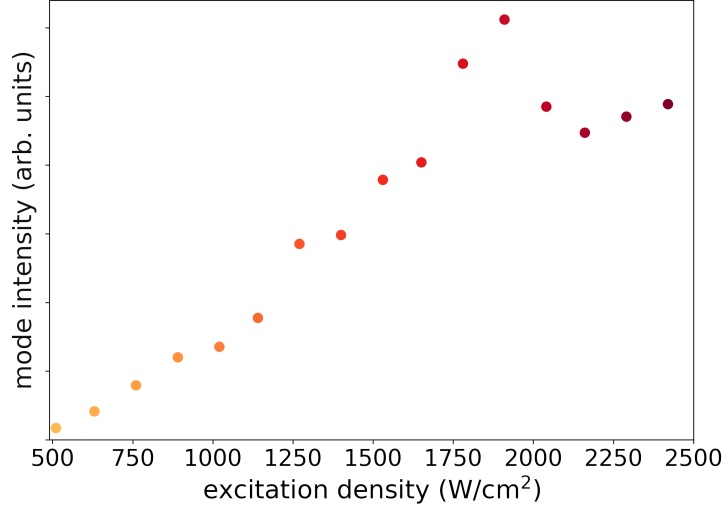


Figure 5.6: Integrated intensity of the most intense mode observed in Figure 5.5 as a function of excitation density. The color scheme of the dots is identical to the scheme in Figure 5.5.

This figure clearly demonstrates that modes can form in smaller disk resonators at lower excitation densities, as in Figure 5.1 ($3.8 \mu\text{m}$ diameter) the mode appears at $2000 \frac{\text{W}}{\text{cm}^2}$ while here ($d_{\text{disk}} = 3.3 \mu\text{m}$) the mode intensity reaches its maximum at this excitation density and degradation starts to set in.

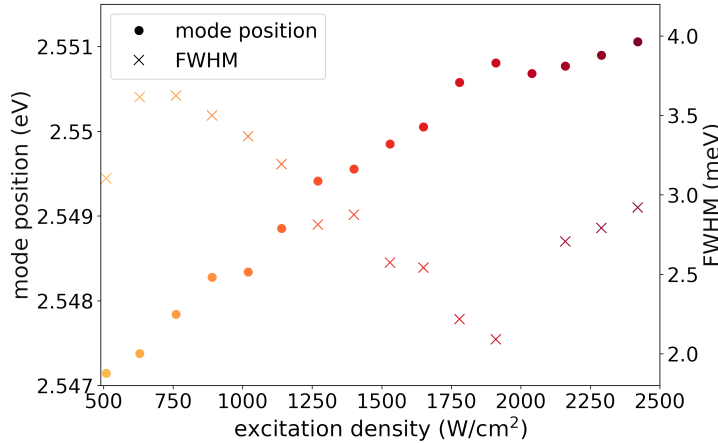


Figure 5.7: Spectral position (circles, left axis) and FWHM (crosses, right axis) of the most intense mode observed in Figure 5.5 as a function of excitation density. The color scheme of the markers is identical to the scheme in Figure 5.5.

Figure 5.7 shows the spectral position and FWHM of the strong mode seen in Figure 5.5. As for the disk with a larger diameter, a blue-shift over the whole measurement range can be seen here. However, the shift is more pronounced in this measurement, a total difference of about 4 meV in the spectral position between $500 \frac{\text{W}}{\text{cm}^2}$ and $2500 \frac{\text{W}}{\text{cm}^2}$ is observed.

The width of the mode displays a similar trend to what was seen in Figure 5.3, continuously lowering until $1920 \frac{\text{W}}{\text{cm}^2}$ and significantly increasing afterwards.

These results lead to a similar conclusion as for the disk characterized above (Figure 5.3): The onset of stimulated emission can be observed in this resonator, however, lasing does not occur, because the microdisk cannot withstand the required excitation densities and degrades above $2000 \frac{\text{W}}{\text{cm}^2}$.

Modes were observed in measurements on disks with a diameter of $2.8 \mu\text{m}$ as well, an example of that is shown in Figure 5.8.

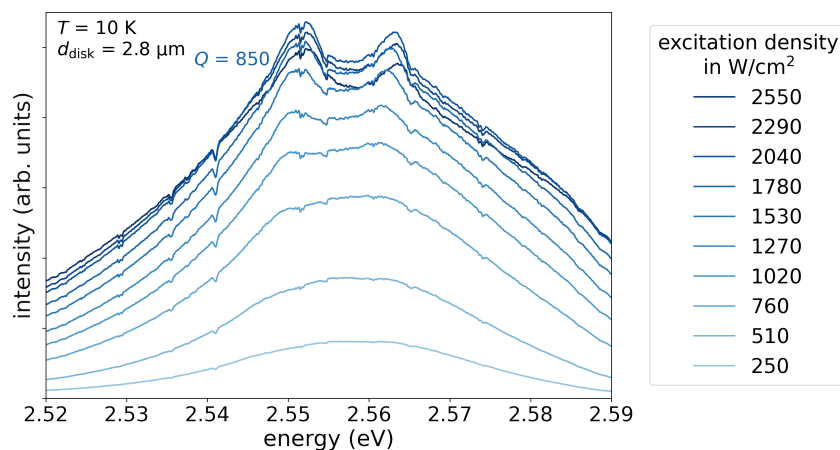


Figure 5.8: Series of μPL spectra with rising excitation density of a free-standing microdisk with a diameter of $2.8 \mu\text{m}$. The Q -factor of the mode with highest Q is indicated in the figure.

Two modes appear near the center of the QW emission. In comparison to the spectra in Figures 5.1 and 5.5 ($d_{\text{disk}} = 3.8 \mu\text{m}$ and $3.3 \mu\text{m}$, respectively) the modes do not ‘grow out’ of the QW emission, but do exhibit degradation similar to the most intense mode in Figure 5.5. Therefore, no clear sign of strong stimulated emission in the resonator is found in this measurement.

The highest Q -factor observed in this measurement is 850, which is significantly lower than the Q values found in experiments on larger disks. In general, the spectra analyzed in this section reveal a trend of lower Q -factors for smaller disks. This will be discussed further in Section 5.1.3 in context with the edge roughness of the microdisks.

As an interim conclusion, modes were measured from microdisk resonators of different sizes. This allows for a comparison that can be seen in Figure 5.9, where spectral positions of modes from several μPL measurements are depicted. This figure also shows theoretical mode positions calculated by Jan Wiersig, which are discussed in Section 5.1.2.

Every row of datapoints represents a measurement of μ PL spectra as seen above, e.g., in Figure 5.1, and the corresponding theoretical data. Different disk sizes (diameters 3.8, 3.3, and 2.8 μm) are separated by black lines and marked by annotations on the left. It is apparent that, although the QW emission typically was present between 2.5 eV and 2.6 eV, modes were found only between 2.5 eV and 2.57 eV, i.e., mainly on the low-energy side of the emission. A large number of modes occurs in the range between 2.54 eV and 2.56 eV. The mode spacing varies between the disk sizes without a clear trend, as the spacing is smallest for the disks with a diameter of 3.3 μm . Additionally, the measured spectral positions are not always equidistant, this can be seen most clearly in the data from the disk with a diameter of 3.3 μm , which corresponds to the spectra shown in Figure 5.5.

The fact that modes can only be observed on a part of the background emission is explained by two factors: Firstly, the modes can only form if there are sufficient emitters at or near their spectral position who can contribute to stimulated emission. This leads to the higher number of modes, and especially modes from which signs of stimulated emission can be observed, towards the center of the QW emission. The second factor is reabsorption in the resonator, which reduces the number of photons that can stimulate emission. Since photons with a higher energy are more easily absorbed, modes form preferably on the low-energy side of the spectrum.

The irregular mode spacing can be explained with the fact that the observed WGMs are of different radial order. WGMs of the same radial order would be evenly spaced. However, in the spectra analyzed here, WGMs of different orders ‘overlap’ to form a complex mode spectrum. This will be confirmed by the theoretical analysis in the following section.

5.1.2. Theoretical Confirmation

Theoretical calculations of the spectral position, width, and field of WGMs in the optically analyzed microdisks based on the boundary element method (see Section 2.3.2) were performed by Jan Wiersig (Universität Magdeburg). The deformation functions extracted from SEM measurements were used as input for these calculations in order to take the deformation of the resonators into account. The effective refractive index of the microdisks was calculated independently from the vertical structure of the resonator and the dispersion of the individual materials. Absorption in the material is taken into account by adding an imaginary part of 10^{-4} to the refractive index.

In deformed microdisks, the spectral position of clockwise and counter-clockwise propagating modes is not degenerate, as would be the case in ideally circular disks [42]. However, the calculations showed that in the resonators analyzed here, this difference is too small to be resolved experimentally, it is masked by the width of the modes. Because of this, the

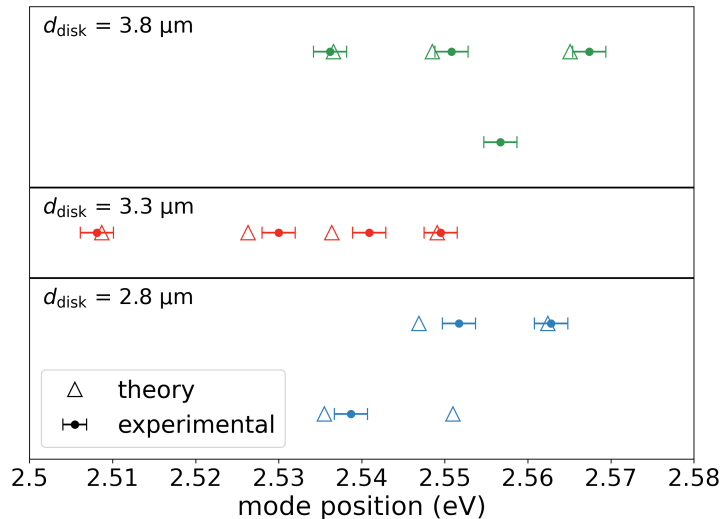


Figure 5.9: Comparison of spectral positions of modes observed experimentally (dots) and calculated theoretically by Jan Wiersig (Universität Magdeburg) (triangles). Different rows show data from different disks, the color of the markers indicates the disk diameter which is also annotated on the left-hand side.

width of the experimentally observed mode can be significantly larger than the individual width of the two differently propagating modes, an effect known as ‘ Q spoiling’. To take this into account, the theoretical estimate of the position and Q -factor of the modes were calculated from the overlapping clockwise and counter-clockwise propagating modes.

Figure 5.9 shows a comparison of the experimentally obtained and theoretically calculated spectral positions of WGMs. Every row of datapoints corresponds to results from a single microdisk, different disk diameters are separated by black lines and marked by annotations on the left-hand side of the figure. The experimental results were discussed in the conclusion of the previous section. It is apparent that the calculated mode positions agree with the experimental results in most cases if the uncertainties are taken into account. The non-equidistant modes observed experimentally from the disk with a diameter of $3.3\mu\text{m}$ are reproduced by the theoretical calculations. As discussed above, the mode spacing is explained by the fact that the observed modes are of different radial order; the observation of these different ‘families’ shows a high quality of the resonators [40]. However, the mode spacing seems to be larger in the theoretical results compared to the experiment. Since the size of the resonator is known through the deformation functions extracted from SEM images, this probably due to the calculated effective refractive index of the microdisks.

The theoretically obtained Q -factor is on the same order of magnitude as the experimentally observed values for Q for all measurements, the largest deviations are smaller

than a factor of two. This agreement might in part be caused by the aforementioned imaginary part of the refractive index that is set to 10^{-4} as a ‘fitting parameter’ to reproduce the experimental values. However, the agreement for all individual disks shows that similar losses can be assumed for all modes. These are well reproduced by the theoretical model. In further calculations, it was found that having an ideal circular disk with smooth edges would approximately double the Q -factor observed in the experiments. The generally good reproduction of the experimental results by the theoretical calculations supports the assumption that the modes observed in μ PL measurements are WGMs.

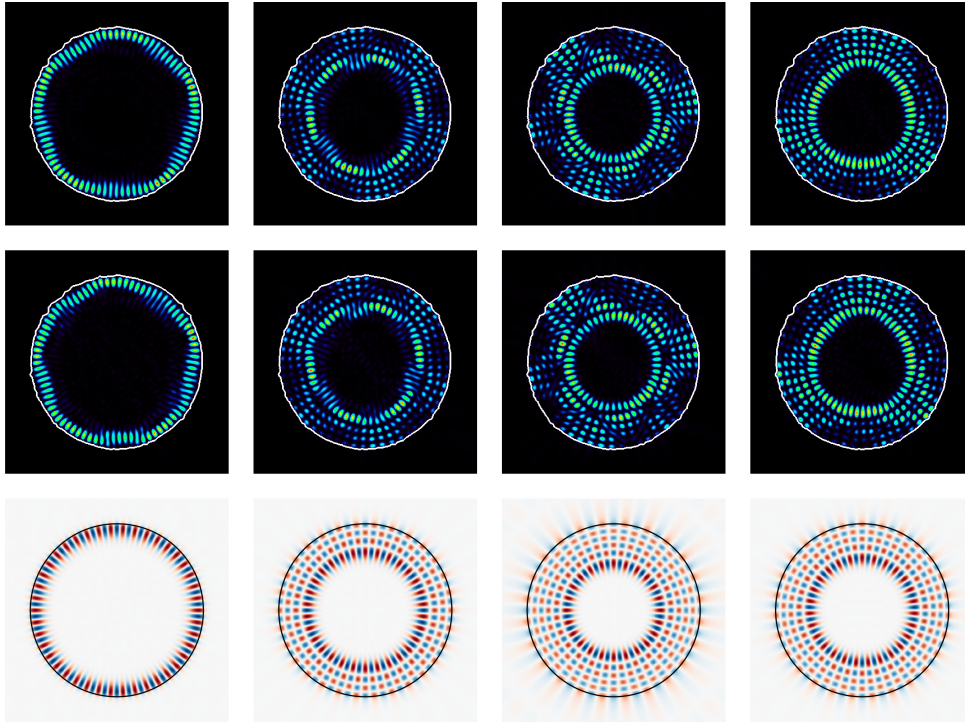


Figure 5.10: Comparison of theoretically calculated electric fields of the modes shown in Figure 5.5. Top two rows show calculations performed by Jan Wiersig (Universität Magdeburg) based on the deformation function of the disk (top row shows clockwise, middle row counter-clockwise propagating modes). Bottom row shows *MEEP* calculations ignoring the deformation of the disks, i.e., assuming ideal circular disks.

The electric field in the resonator corresponding to each of the four modes observed in Figure 5.5 ($d_{\text{disk}} = 3.3 \mu\text{m}$) was calculated using the boundary element method for the clockwise and counter-clockwise propagating modes. The results are displayed in the top (clockwise) and middle (counter-clockwise) row of Figure 5.10. The modes are sorted by their spectral position from 2.51 eV (left) to 2.55 eV (right). These calculations were performed by Jan Wiersig (Universität Magdeburg).

Additionally, FDTD simulations of an ideal circular disk with the same (average) radius

were performed by the author himself using the *MEEP* software, as described in Section 4.4. The results from these calculations are used to analyze the influence of the edge roughness on the spectral position of resonating modes and their fields. Images of the electric field corresponding to modes in the same spectral region as the experimentally observed modes are shown in the bottom row of Figure 5.10. Note that for ideal circular disks clockwise and counter-clockwise propagating modes are degenerate in their field and spectral position.

The fields in each column of Figure 5.10, corresponding to an experimentally observed WGM, appear similar. The same is true for the calculated spectral position of the modes. Table 5.1 compares the number of nodes in radial and azimuthal direction as well as the spectral positions for both calculations.

boundary element method			<i>MEEP</i> software		
position (eV)	number of nodes		position (eV)	number of nodes	
	radial	azimuthal		radial	azimuthal
2.5115	0	82	2.5104	0	84
2.5365	3	58	2.5418	3	60
2.5425	5	46	2.5540	5	48
2.5495	4	52	2.5556	4	54

Table 5.1: Comparison of the spectral position and electric field of the modes observed in the spectra in Figure 5.5 as calculated using the boundary element method (based on deformed microdisks, performed by Jan Wiersig) and *MEEP* software (neglecting edge roughness).

In this table, a good agreement between both theoretical models can be seen, with deviations in the mode position averaging 6.0 meV. The fields that were calculated corresponding to the WGMs also show similarities, as the number of radial nodes is equal for all analyzed modes and the number of azimuthal nodes that can be observed in the *MEEP* calculation is equal to the number of azimuthal nodes found using the boundary element method plus two in all cases. However, the number of nodes is not a good quantum number for WGMs in deformed microdisks. Therefore, it cannot be used to identify the resonating modes and can only give an insight into how the field qualitatively compares with the simulation of an ideal microdisk. This can be seen in Figure 5.10, as it can be hard to define the number of nodes close to the edge in the top two rows.

The changes in the fields caused by edge roughness in the top two rows in Figure 5.10 are clearly visible and evident even towards the middle of the disk, far away from the deformed edge. This demonstrates that the deformation has an effect on the field inside the microdisk. However, the spectral position of the resonances is not strongly influenced by the edge roughness, as both models produce similar values for it. This is in agreement

with theoretical studies on resonances in randomly deformed microdisks [109].

5.1.3. Deformation of the Resonators

The deformation functions of several free-standing microdisks were extracted from SEM images as described in Section 4.2.2 in order to analyze the structural quality of the resonators. This included all disks that were discussed in the previous sections and which are included in the comparison in Figure 5.9, as their data is needed for the theoretical analysis described above.

The resulting deformation functions $r(\varphi)$ were fitted with a circle of radius \bar{r} . This is the average of the deformation function and was assumed to be the radius of the disk if its edge was an ideal circle.

The deviation of the disk edge from its ideal radius \bar{r} was calculated based on the deviation of all n datapoints r_i of $r(\varphi)$ from \bar{r} . Averaging gives the standard deviation

$$\Delta r = \frac{1}{n} \sum_i \sqrt{(\bar{r} - r_i)^2}. \quad (5.1)$$

From this absolute deviation, a relative deviation of the disk from its ideal radius can be calculated as $\frac{\Delta r}{\bar{r}}$. This ratio is important, because deviations from the ideal radius with the same absolute value Δr lead to a stronger change of the curvature of the disk edge if the radius \bar{r} is smaller. Therefore, $\frac{\Delta r}{\bar{r}}$ is used as a measure of how strongly the deformation of the edge disturbs a mode propagating in the microdisk.

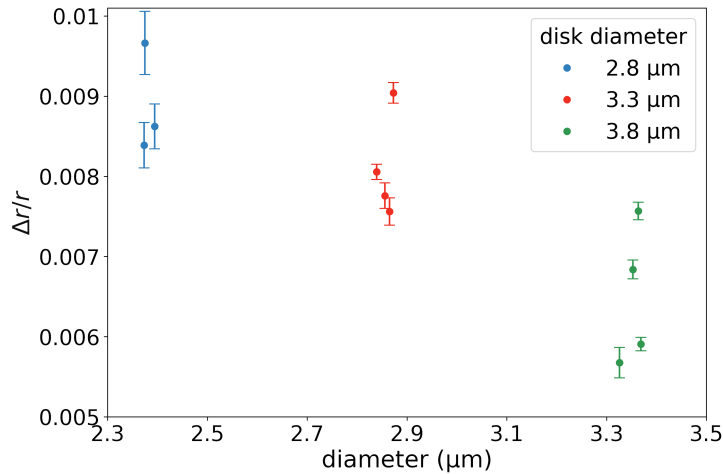


Figure 5.11: Relative deviation of the disk edge from the ideal radius for several free-standing disks as a function of its average diameter.

Figure 5.11 shows the relative deviation from the ideal radius as a function of the diameter

($d = 2 \cdot \bar{r}$) for eleven disks of three different sizes. From the figure it is obvious that the relative deviation from \bar{r} is lower for larger disks, ranging between 1 and 0.5% for all analyzed resonators. It can also be seen that the diameters of the disks that were measured in SEM are lower than the ones given in the legend. The latter are the values that were intended during growth and processing of the disks.

These differences between the observed and intended diameters point to a systematic error in the fabrication process. This seems to only affect the size of the disks and not to cause edge roughness, as the deviation $\frac{\Delta r}{\bar{r}}$ is below 1% for all disks. The systematic error furthermore does not impact the theoretical calculations in Section 5.1.2, as they are based on the values extracted from SEM images and do not depend on the diameters intended during processing.

The absolute values of Δr are displayed in Figure 5.12 as a function of the diameter. In this figure it is evident that Δr ranges from 9 to 13 nm for all disk sizes, no correlation between Δr and d can be found. This shows that $\frac{\Delta r}{\bar{r}}$ is reduced for larger diameters simply because the denominator grows, while the numerator does not change.

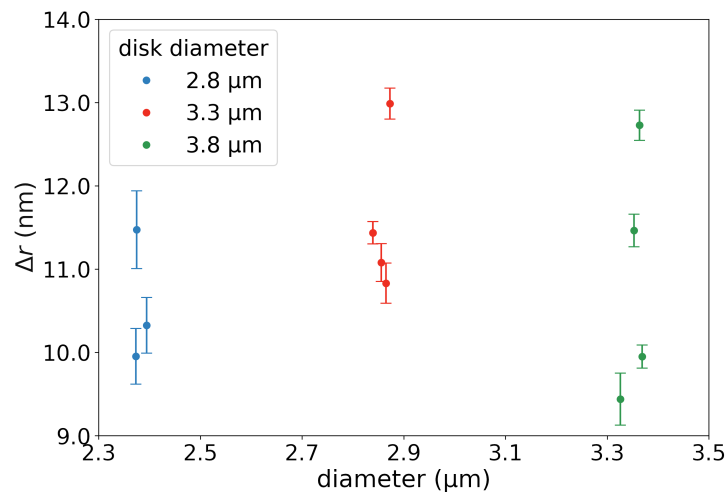


Figure 5.12: Absolute deviation of the disk edge from the ideal radius for several free-standing disks as a function of their average diameter.

Figure 5.12 shows that the fabrication process of the disks, especially the e-beam lithography and reactive ion etching that define the disk edges (see Section 4.1), has a finite accuracy, being the same for all disk sizes and governing the edge roughness of the free-standing resonators analyzed here. The Δr observed here appear relatively small in comparison to the diameters of the analyzed disks, but it has been reported that roughness on this order of magnitude can have a strong influence on the optical quality of the resonator [117], as will be seen in the following.

As explained above, the relative deviation $\frac{\Delta r}{r}$ can be used as a measure of how strongly a propagating mode is disturbed by the edge roughness. The optical quality of a microdisk resonator is measured by Q_{\max} , the maximum Q -factor observed in a series of μ PL spectra similar to Figures 5.1, 5.5 and 5.8. Therefore, Figure 5.13 shows a plot of Q_{\max} vs. $\frac{\Delta r}{r}$, correlating edge roughness and optical quality.

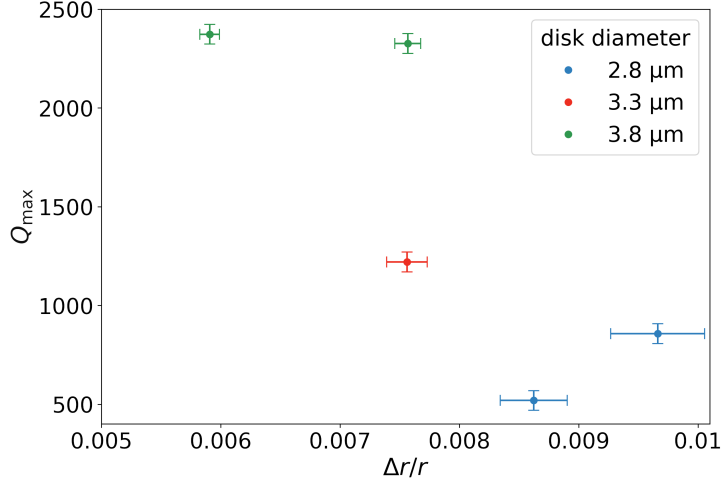


Figure 5.13: Highest experimentally observed Q -factor as a function of relative deviation from the ideal radius for free-standing disks of different diameters.

The image reveals that Q_{\max} is higher for disks with lower relative deviation. This inverse correlation is expected, because the edge roughness disturbs the propagating modes and reduces their lifetime and Q -factor. This has been previously observed experimentally when fabrication techniques that reduce edge roughness were compared to previous results [17, 18, 106, 118]. Here it is shown for disks with different roughnesses that were fabricated in the same process. FDTD simulations have shown that random edge roughness does not substantially reduce the Q -factor of the clockwise and anti-clockwise propagating mode individually [109]. Therefore, the increase of the experimentally observed Q_{\max} might be caused by the reduction of ‘ Q spoiling’ due to the splitting of clockwise and counter-clockwise propagating modes discussed above.

Given the dependence of $\frac{\Delta r}{r}$ on the disk diameter, Figure 5.13 also shows that higher Q_{\max} are observed for larger disks. Here the disk diameter could be a hidden variable, since the edge of a larger disk is curved less and the disk therefore supports modes with higher Q -factors. However, a theoretical study on InGaAsP/InP quantum dot microdisks came to the conclusion that the reduction of the Q -factor when the disk diameter is reduced from $2.5 \mu\text{m}$ to $1.0 \mu\text{m}$ is lower than 2%, assuming a wavelength of $1.55 \mu\text{m}$ [119]. The reduction of the Q -factor is even lower for larger diameters. In the experiment presented here, the wavelength is lower than the radius so it can be assumed that the disk size has an

even smaller influence on the Q -factor of the modes studied. In an experimental analysis of InGaN hexagonal wires it was found that above a diameter of $2.8 \mu\text{m}$ the Q -factors are not affected by resonator size [120]. Because of their hexagonal shape, these structures do not compare well to our microdisks, but the standing wave is contained in a resonator with dimensions just slightly larger than the wavelength in these structures as well.

5.2. Free-standing Microdisk Resonators with δ -type Halogen Impurities

In this subsection, results obtained from the optical characterization of microdisks on sample B are discussed. The density of the halogen impurities incorporated as dopants in the QW was reduced by about two orders of magnitude in the fabrication of sample B compared to sample A (for an overview of all samples used for measurements in this work see Table 4.1 on page 31). As dopants are only included in the center of the QW and not homogeneously along the z -axis, this results in a so-called δ -type doping. A F density of about $3 - 4 \cdot 10^{16} \text{ cm}^{-3}$ is reached in the $\text{Zn}_{0.85}\text{Cd}_{0.15}\text{Se:F}$ QW, embedded in 30 nm-thick $\text{Zn}_{0.82}\text{Mg}_{0.18}\text{Se}$ barriers. This sample was fabricated in order to test the suitability of free-standing microdisks for applications as single-photon emitters or in qubit storage as discussed in Section 2.2.4. Here, the influence of the low dopant concentration on the optical properties of the microdisk resonators will be analyzed.

At low excitation densities, modes are found on the low-energy side of the QW emission, which do not show signatures of stimulated emission. When the disks are excited with higher excitation densities, WGMs similar to those shown in the previous section are observed. The degradation of these modes under prolonged excitation is discussed in more detail at the end of this subsection.

5.2.1. Modes under Optical Excitation

The disks were excited for μPL experiments as in the experiments on sample A described in section 5.1.1. Smaller modes were observed at low excitation densities, Figure 5.14 gives an overview of the emission from a disk with a diameter of $3.8 \mu\text{m}$ at excitation densities significantly lower than those used in the previously described experiments for this disk size ($50 - 510 \frac{\text{W}}{\text{cm}^2}$).

It is obvious that the emission of the microdisks analyzed in this section is blue-shifted compared to the spectra of disks on sample A (Section 5.1). The emission is now found between 2.6 and 2.67 eV, compared to 2.53 – 2.59 eV; it still consists of a single broad band.

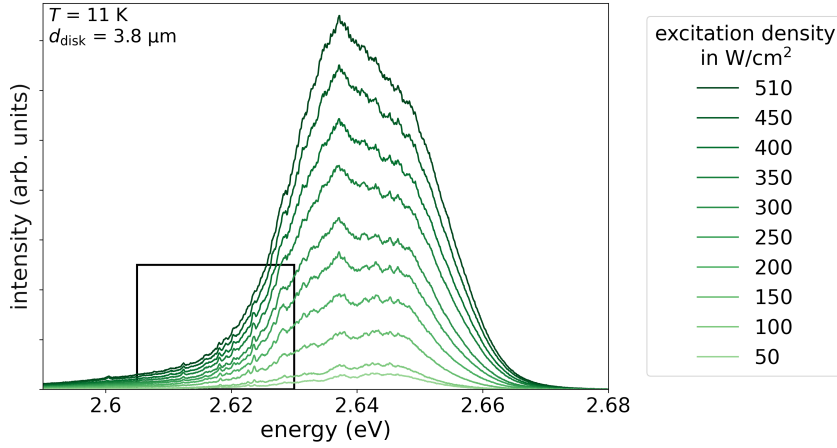


Figure 5.14: Series of μ PL spectra with rising excitation density of a free-standing microdisk with a diameter of $3.8 \mu\text{m}$. The black rectangle marks the part of the spectrum that is shown in detail in Figure 5.15.

The shift of the luminescence can be explained by the reduction of the Cd concentration in the QW, which leads to an increase of the bandgap.

The spectra exhibit small modes on the low-energy end of the spectrum in the region highlighted by the black rectangle, of which a zoom-in is shown in Figure 5.15 for a more detailed analysis. These modes might be resonances (WGMs) of the microdisks, whose intensity is limited due to the low gain at their spectral position. Alternatively, the maxima might be explained as emission from a single halogen impurity that is amplified in the microcavity due to the Purcell effect.

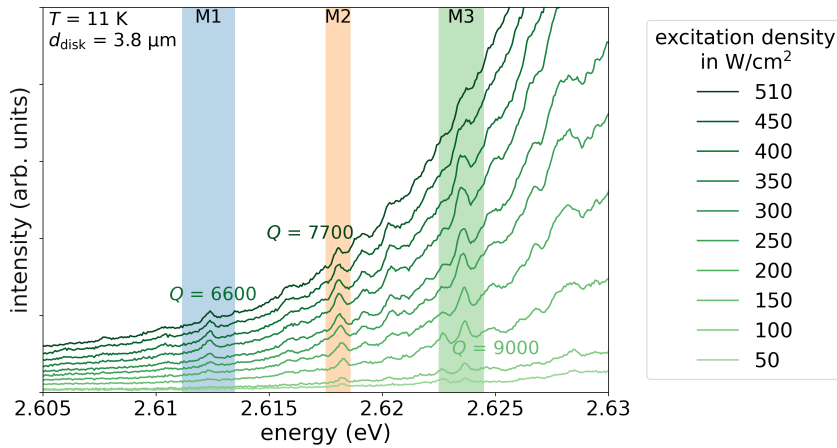


Figure 5.15: Zoom of the series of μ PL spectra with rising excitation density of a free-standing microdisk with a diameter of $3.8 \mu\text{m}$ shown in Figure 5.14. The maximum Q -factor for each of the observable modes is indicated in the figure.

Three small sharp modes appear on the background emission, labeled M1, M2, and M3. With rising excitation density, the modes become less visible and disappear in the

background, this can be seen most clearly for mode M3. The maximum Q -factors observed for each mode are given in the figure, high values (between 6600 and 9000) are recorded. For mode M3 it stands out that the spectrum with the highest Q -factor was measured under an excitation density of just $150 \frac{\text{W}}{\text{cm}^2}$. For modes M1 and M2, the highest Q -factor was found under significantly larger excitation densities.

The small modes can be explained by the emission of the QW being superimposed with resonances of the microdisk. The modes appear at the edge of the emission band (on the low-energy side), where the luminescence is not very intense at low excitation density. When the excitation density is increased, the background intensity increases and the gain of the active material is too low to sustain mode activity. The modes were fitted similarly to the modes discussed above; the results are displayed in Figures 5.16 and 5.17.

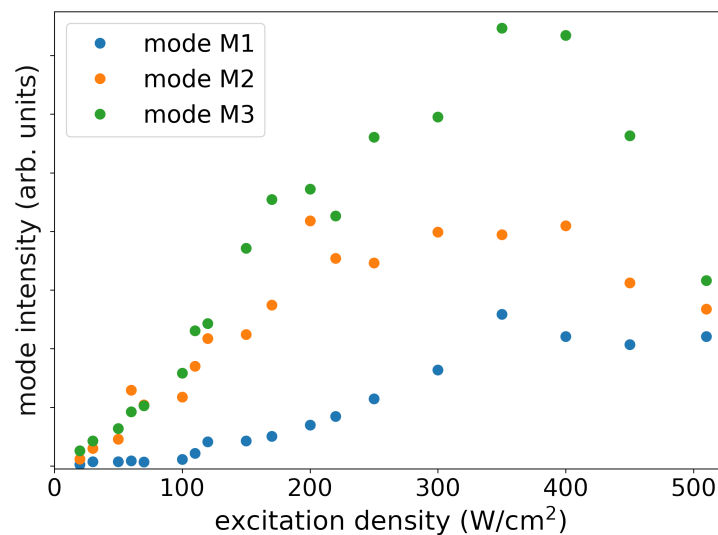


Figure 5.16: Integrated intensity of the modes observed in Figure 5.15 as a function of excitation density. The colors of the markers correspond to the colored columns marking the modes in Figure 5.15.

All modes have in common that their intensity, displayed in Figure 5.16, increases linearly after they appear in the measurement. For the highest excitation densities used here, the intensity saturates and starts to decrease (opposed to the background intensity which increases over the whole course of the measurement).

As the modes do not show a super-linear growth of intensity, and their intensity even starts to decrease at relatively low excitation densities compared to the modes in the previous sections, it can surely be assumed that no lasing is occurring in these experiments. The saturation of intensity is probably due to the low gain of the active material near the low-energy edge of the broad emission band. If the halogen impurities are the source of the emission forming these modes, their intensity might be limited by the low concentration of

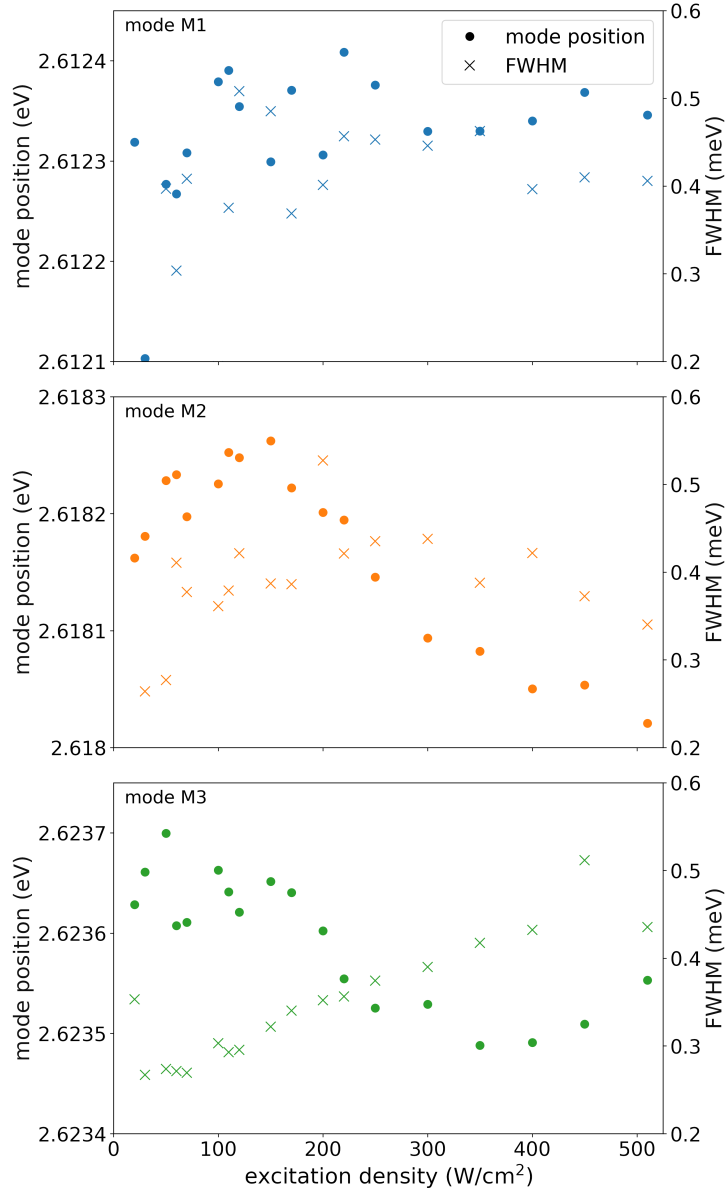


Figure 5.17: Spectral position (circles, left axis) and FWHM (crosses, right axis) of the modes observed in Figure 5.15 as a function of excitation density. The colors of the markers correspond to the colored columns marking the modes in Figure 5.15. Data for each mode was plotted in a separate subplot for better visibility.

emission centers.

Figure 5.17 shows the width and position of the three modes as a function of excitation density. No tendency for either quantity can be observed for all modes. Modes M2 and M3 exhibit a slight red-shift with rising excitation density (0.2 – 0.3 meV) while the position of mode M1 does not seem to change. The FWHM of mode M3 continuously increases with excitation density, the width of the other modes do not change.

The red-shift observed for modes M2 and M3 can be explained by an increase of the temperature in the microdisk due to the excitation. For mode M1 this change is masked by the overall scattering of the fit results due to the low mode intensity. The increase of the width of mode M3 recorded here is due to a spreading of the mode by an uneven increase of the background emission. The QW emission intensity increases more strongly on the high-energy side of the mode. Clearly, there are no indications of stimulated emission into or lasing of these modes.

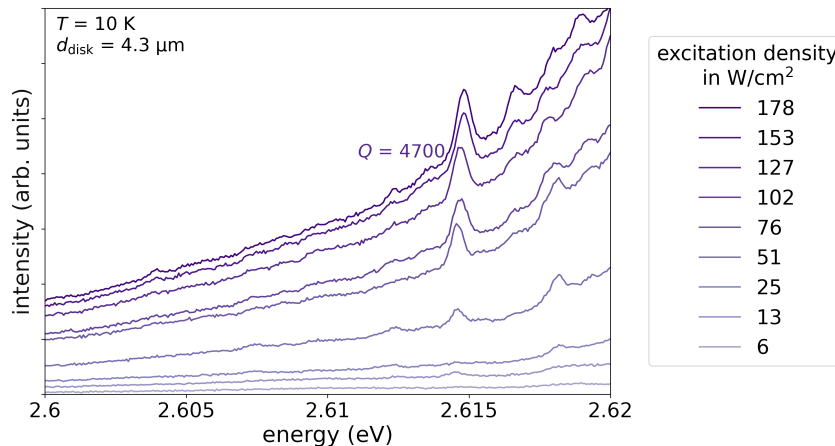


Figure 5.18: Zoom of a series of μ PL spectra with rising excitation density of a free-standing microdisk with a diameter of $4.3 \mu\text{m}$. The maximum Q -factor found is indicated in the figure.

Similar modes were observed for disks of other sizes. Figure 5.18 shows a series of spectra with rising excitation power taken on a disk with a diameter of $d_{\text{disk}} = 4.3 \mu\text{m}$. Similar to the measurement above ($d_{\text{disk}} = 3.8 \mu\text{m}$), a small mode appears on the low energy side of the emission at low excitation densities. Likewise, a high Q -factor (4700) is observed. The course of mode intensity with rising excitation density is similar to that of the small modes analyzed above, as this mode is eventually masked by the rising background intensity, too. No trend in either position or width of the mode was observed over the course of the measurement.

In order to analyze how the modes form, a μ PL map scan of a disk with a diameter of $4.3 \mu\text{m}$ was performed to provide spatial analysis. For this, the exciting laser was scanned across the disk and a μ PL spectrum was recorded at each point. The total integrated intensity as a function of excitation position is shown in Figure 5.19.

The map scan shows the highest intensity in the middle of the disk, which is located at a x position of $6.5 \mu\text{m}$ and a y position of $4.5 \mu\text{m}$. In the four central spectra recorded there, small modes can be observed, similar to those discussed above. These positions are marked by four differently colored rectangles in the map scan and will be discussed in

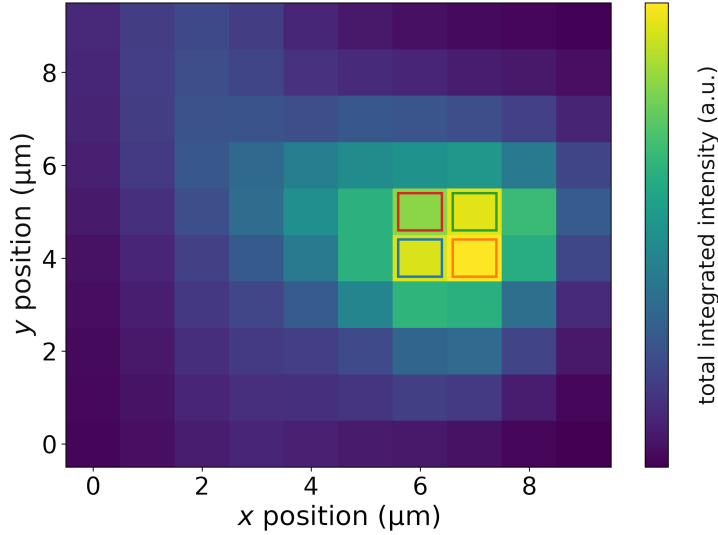


Figure 5.19: μ PL map scan of a free-standing microdisk with a diameter of $4.3\ \mu\text{m}$. Color coded is the total integrated intensity of the emission under excitation with $50\ \frac{\text{W}}{\text{cm}^2}$ at each spot. Emission from a waveguide fabricated near the disk can be seen in the top-left corner of the image. Colored rectangles indicate four spots measured near the center of the disk, the corresponding spectra are shown in Figure 5.20.

more detail later.

Since the laser spot has a diameter of about $3\ \mu\text{m}$, it will excite larger regions than the $1\ \mu\text{m} \times 1\ \mu\text{m}$ squares depicted in Figure 5.19. This can be seen in the apparent diameter of the disk of about $6 - 7\ \mu\text{m}$, compared to the actual diameter of the disk ($4.3\ \mu\text{m}$). This means that if the excitation is centered in the middle of the disk, it will find the most excitable active material. On the other hand, if the excitation spot is moved towards the edge of the resonator, part of the laser beam will miss it. That explains why the highest intensities can only be observed in a relatively small region in the center of the disk. Given that the modes are strongest in the spectra recorded near the center of the disk, it is apparent that the modes need the excitation of a large area of the microdisk to form. This contradicts the assumption that the small modes might be connected to a single or a small number of the halogen impurities. A detailed analysis of the spectra marked by colored rectangles in Figure 5.19 is given in Figure 5.20.

The four ‘central’ spectra from the map scan show that four small modes form in the spectral range from 2.617 to $2.623\ \text{eV}$. However, not all of these modes can be seen in all spectra; this is only true for the two ‘outer’ modes (i.e., the modes with highest and lowest energy). The other two modes appear in two spectra each, with the mode near $2.6195\ \text{eV}$ being visible in the spectra plotted in blue and yellow and the mode near $2.6205\ \text{eV}$ being visible in the red and green spectra. It is notable that the spectra in which the same

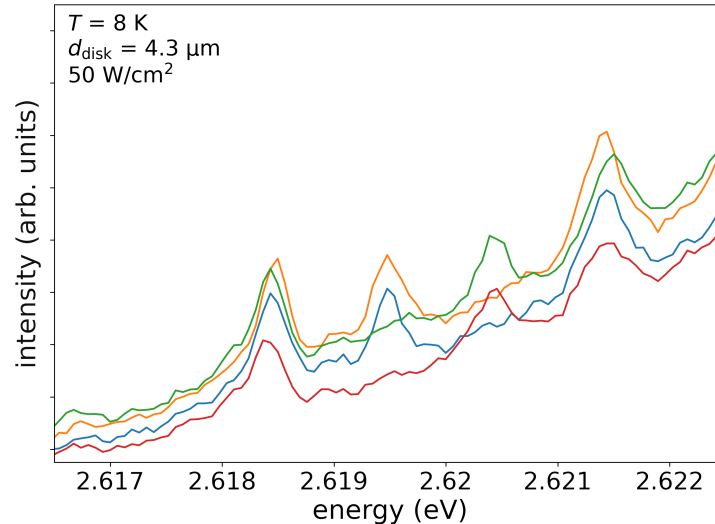


Figure 5.20: Zoom of μ PL spectra which are part of the map scan shown in Figure 5.19. The colors of the labels correspond to the rectangular markers in that plot.

modes appear are neighboring.

In Section 5.1.2 it was seen that each resonator mode corresponds to a different field in the microdisk. The images in that section show that these fields can differ significantly for different modes. Based on this, it is apparent that different excitation spots might not excite the same field distributions.

The modes analyzed in this section up to now do only occur under low excitation energies, since the active material does not provide enough gain for stimulated emission or lasing. Based on the results from the map scan in Figure 5.19, it is unlikely that these modes are caused by the δ -type fluorine dopants. They are resonances of the microdisks.

Modes at spectral positions closer to the center of the disk's emission band were observed at higher excitation densities. These resonances are similar to the WGMs found for sample A above and will be analyzed in the following.

In Figure 5.21, spectra recorded on the same disk that already showed small modes for low excitation densities (Figure 5.15) are shown. With rising excitation density, a central strong mode appears from the emission. This behavior is similar to modes observed in microdisks of the same diameter on sample A (higher dopant concentration, compare Section 5.1.1, Figure 5.1). This includes the maximum Q -factor observed being around 2000 (1800 for the measurement shown here, 2300 in Figure 5.1). Note that the small modes discussed above are not visible in this figure due to their low intensity in comparison to the main emission from the disk. In Figure 5.15 a zoom into the spectra was needed to visualize the spectra. The intensities found in the measurements displayed in Figure 5.21

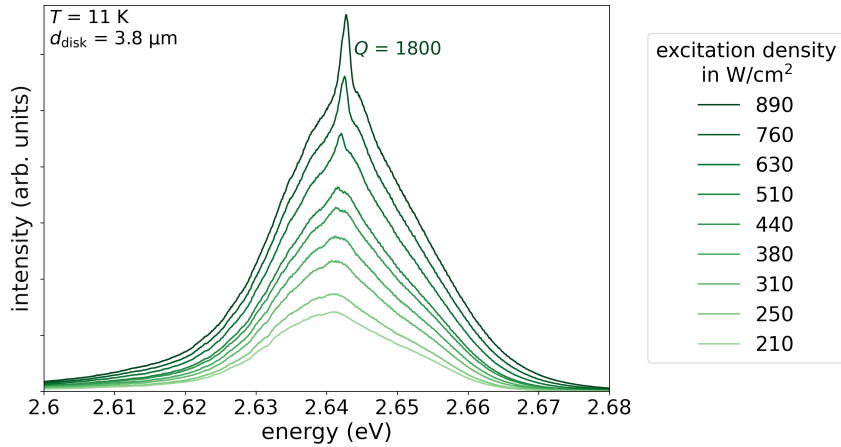


Figure 5.21: Series of μPL spectra with rising excitation density of a free-standing microdisk with a diameter of $3.8 \mu\text{m}$. The Q -factor of the mode with the highest Q is indicated in the figure.

are even higher, as this measurement was taken with a slightly different distance between microscope objective and sample, resulting in a different focus.

The observed mode will be analyzed similarly to previous modes. This means that the following figures show the intensity, width and position of the mode as a function of excitation density. The fit results displayed there will be used to analyze if lasing is occurring in the measurement.

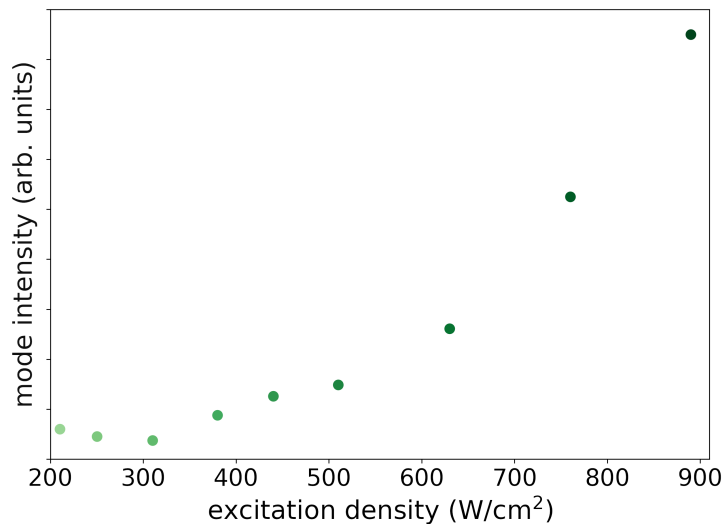


Figure 5.22: Integrated intensity of the mode observed in Figure 5.21 as a function of excitation density. The color scheme of the dots is identical to the scheme in Figure 5.21.

At very low excitation densities (below $300 \frac{\text{W}}{\text{cm}^2}$), the intensity of the mode slightly decreases with a rise in excitation density. This is likely due to the fact that a low mode intensity

will lead to a larger error in the fitting process. In fact, the mode is not observable above the background in Figure 5.21 at excitations below $300 \frac{\text{W}}{\text{cm}^2}$. The gradient with which the mode intensity grows as a function of excitation density in Figure 5.22 significantly changes at $500 \frac{\text{W}}{\text{cm}^2}$, similar to results observed from disks of the same size on sample A (compare Figure 5.2). The excitation density at which this change occurs is lower compared to results from disks with a larger halogen dopant concentration, where a threshold at $2800 \frac{\text{W}}{\text{cm}^2}$ was found.

The lower threshold excitation density is partly explained by fluctuations of the excitation spot and focus quality. This is supported by the observation that for a different excitation spot on the same disks other modes appeared only at an excitation density of about $2000 \frac{\text{W}}{\text{cm}^2}$. However, the reduced concentration of shallow donors might reduce the absorption of photons propagating in the microdisk, enabling a lower lasing threshold.

The changes in the gradient can be a sign for the onset of lasing if the width of the mode is reduced simultaneously. This will be analyzed based on the results shown in Figure 5.23.

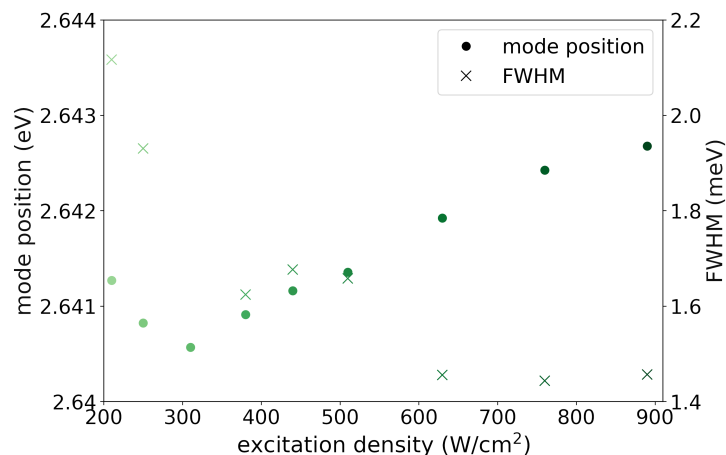


Figure 5.23: Spectral position (circles, left axis) and FWHM (crosses, right axis) of the mode observed in Figure 5.21 as a function of excitation density. The color scheme of the markers is identical to the scheme in Figure 5.21.

The FWHM of the observed mode is reduced over the course of the measurement in two steps corresponding to the changes in mode intensity discussed above (300 and $500 \frac{\text{W}}{\text{cm}^2}$). Above an excitation density of about $300 \frac{\text{W}}{\text{cm}^2}$, the mode position increases linearly up to a total shift of 2 meV at $900 \frac{\text{W}}{\text{cm}^2}$.

Similar to the results discussed from disks with higher dopant concentrations in the QW (sample A), lasing is not clearly observed in this measurement since the measurement had to be stopped at relatively low excitation densities due to degradation. This prevents the observation of the typical s-shape expected in Figure 5.22. However, the occurrence of stimulated emission can certainly be assumed based on the reduction of mode width

combined with the threshold behavior of its intensity.

The blue-shift of modes with rising excitation densities has been observed in measurements of sample A as well and was attributed to a carrier induced change of the refractive index. There, modes which shifted strongly also showed a strong intensity degradation, probably connected to the large number of carriers created by the strong optical excitation.

Further modes observed from different disks will be analyzed in order to gain more information about their formation and possible stimulated emission in the disks.

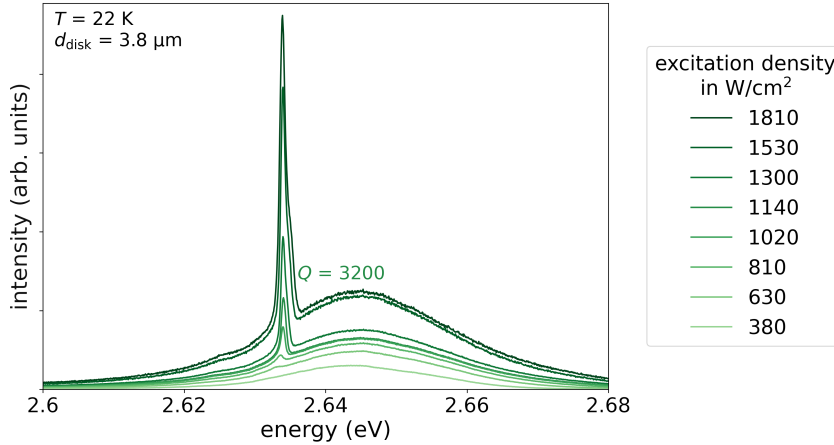


Figure 5.24: Series of μ PL spectra with rising excitation density of a free-standing microdisk with a diameter of $3.8 \mu\text{m}$. The Q -factor of the mode with the highest Q is indicated in the figure.

Figure 5.24 shows a series of spectra taken from a disk with a diameter of $3.8 \mu\text{m}$, which features a clear mode with a high Q -factor (3200) growing on the background. This is a measurement on a disk with the same size as that depicted in Figure 5.21, but the mode is clearly more intense compared to the background. Because of this, more information on the emission and degradation of the mode above threshold can be expected from the analysis of these spectra.

The integrated intensity of this mode is plotted as a function of excitation density in Figure 5.25. It increases strongly at excitation densities above $1200 \frac{\text{W}}{\text{cm}^2}$. This threshold corresponds well to the spectra shown in Figure 5.24, where the mode is starting to become visible at an excitation density of $810 \frac{\text{W}}{\text{cm}^2}$.

The width of this mode, shown in Figure 5.26, is reduced around the aforementioned threshold of $1200 \frac{\text{W}}{\text{cm}^2}$, but quickly starts to rise again at about $1300 \frac{\text{W}}{\text{cm}^2}$. The position of the mode shifts towards higher energies, but stabilizes after the threshold; in total the mode position changes by only 1 meV.

The results shown here are similar to previously analyzed modes of microdisks on both sample A and B, as a similar course of the FWHM has been observed in Figures 5.3 and

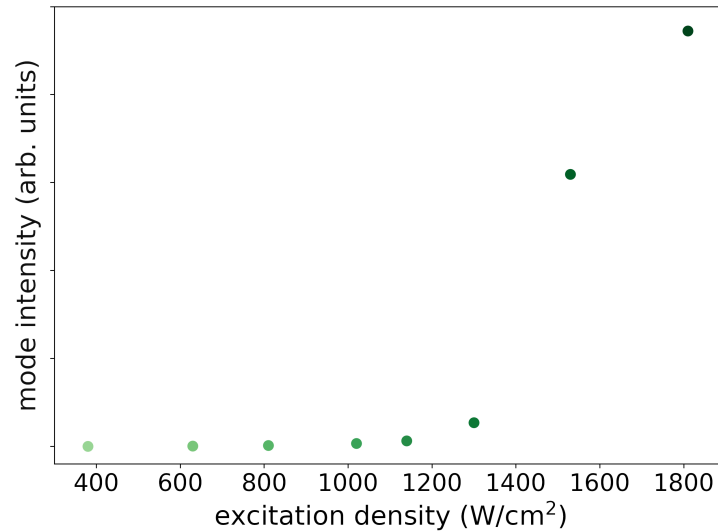


Figure 5.25: Integrated intensity of the mode observed in Figure 5.24 as a function of excitation density. The color scheme of the dots is identical to the scheme in Figure 5.24.

5.7 (sample A, $d_{\text{disk}} = 3.8 \mu\text{m}$ and $3.3 \mu\text{m}$, respectively). The changes observed in the intensity of the mode resemble the results shown in Figure 5.2 (sample A, $d_{\text{disk}} = 3.8 \mu\text{m}$). From that it can again be assumed that an onset of stimulated emission is observed, but the mode starts to degrade if the disk is excited above the threshold.

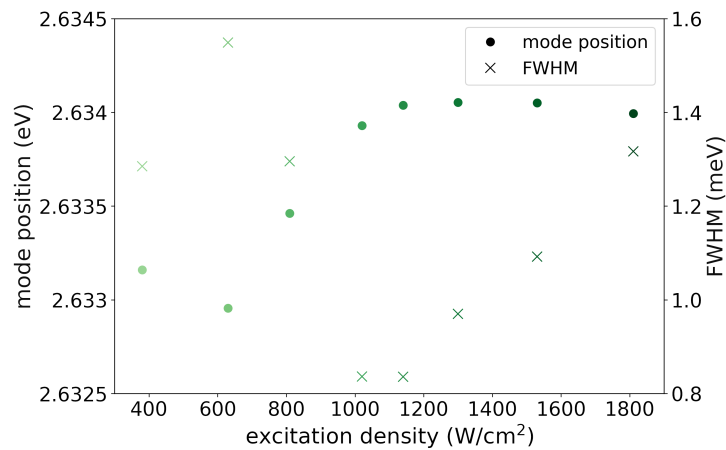


Figure 5.26: Spectral position (circles, left axis) and FWHM (crosses, right axis) of the mode observed in Figure 5.24 as a function of excitation density. The color scheme of the dots is identical to the scheme in Figure 5.24.

The measurements presented in this section seem to indicate that the shift of the mode position observed for large modes is smaller for disks with a lower dopant concentration. Additionally, the microdisks on sample B appear to degrade more quickly with rising excitation density compared to their counterparts with fluorine concentrations on the order

of $3 \cdot 10^{18} \text{ cm}^{-3}$ (sample A).

As was already discussed for sample A above, the blue-shift of the WGMs is likely explained by a change in refractive index of the microdisk. Calculations based on the boundary-element method (see Section 5.1.2) revealed that to cause these shifts a change of n by $2 \cdot 10^{-3}$ would be sufficient. This also explains the reduction of the blue shift for microdisks with a lower concentration of halogen impurities, as a lower dopant concentration leads to a reduction of the number of excited charge carriers.

A second explanation of the shift could be an increase of the disk diameter caused by heating of the sample due to the exciting laser or energy dissipated during mode propagation. However, an analysis in Section 5.2.2 will show that a temperature increase leads to a red-shift of the WGMs.

Publications on similar disks attribute a blue-shift of emission to strain relaxation in the QW via the formation of dislocations as the ZnSe QW is tensilely strained due to the larger lattice constant of the ZnMgSe barriers [14]. This cannot be applied to the microdisks analyzed in this work as the lattice constant of the ZnCdSe QWs are larger than those of the ZnMgSe barriers for both sample A and B.

A possible explanation of the observed degradation of WGMs is that the halogen impurities degrade and are transformed to nonradiative recombination centers. In disks with a lower number of impurities less emission centers can be converted, resulting in a faster degradation of the structures on sample B. Since the background QW emission of the microdisks does not change during the degradation, it is obvious that not all halogen impurities are affected by the degradation, but only a small fraction of them. These might be located in sites with a high electric field under mode propagation. This is in agreement with investigations of the degradation of ZnSe-based emitters, which concluded that the intensity reduction often starts at point defects [52].

As an interim conclusion of the optical characterization, free-standing microdisks with δ -type doping show modes with similar properties to the WGMs yielding stimulated emission that were observed from free-standing disks with a higher dopant concentration in the QW.

Additionally, modes with low intensity can be observed on the low-energy side of the emission at low excitation densities. These modes exhibit high quality factors (5000 – 9000), but occur at low excitation densities only, as they are masked by the background QW emission at higher excitation.

The degradation of intense modes in disks with a low halogen concentration will be analyzed in more detail in the following section in order to gain more insight into its cause and influence on the emission.

5.2.2. Degradation of Mode Intensity under Continuous Excitation

For a better analysis of the degradation observed in previous chapters, disks on sample B are excited continuously with a fixed excitation density and μ PL spectra are recorded in regular intervals. Two microdisks, with a diameter of $3.3 \mu\text{m}$ each, that displayed modes with a comparable threshold of about $750 \frac{\text{W}}{\text{cm}^2}$ were used for this experiment, their spectra can be seen in Figure 5.27. The experiment ran until the modes observed at the beginning were no longer visible on the background emission. One measurement was performed just slightly above the threshold at an excitation density of $780 \frac{\text{W}}{\text{cm}^2}$ (Figure 5.27a), for the second measurement the excitation density was doubled.

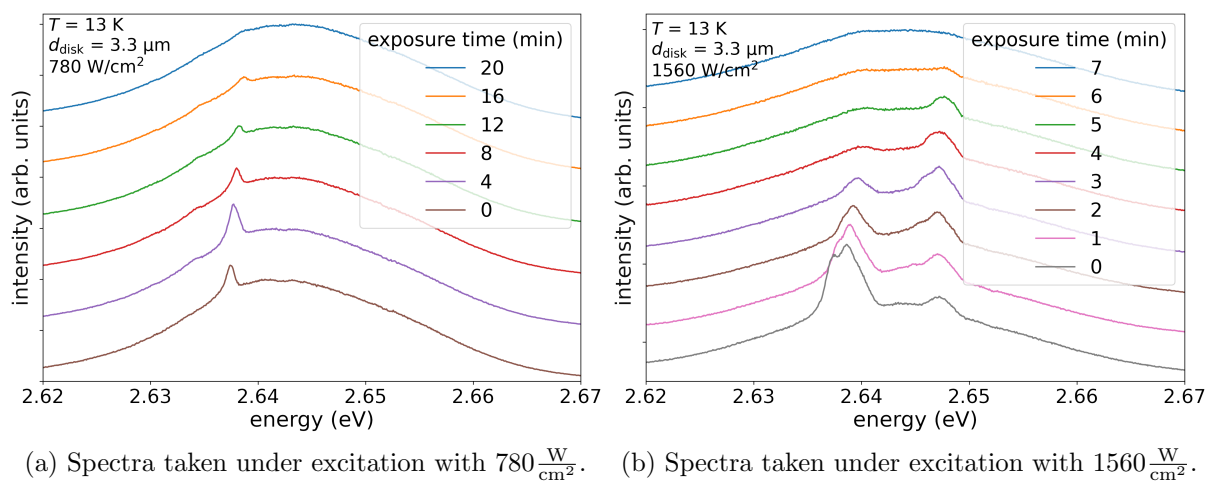


Figure 5.27: Two time series of μ PL spectra of free-standing microdisks with a diameter of $3.3 \mu\text{m}$ recorded under continuous excitation of the microdisks. The excitation intensity is given in the caption of the subfigures. Note the different timescales in the legends of (a) and (b).

In Figure 5.27a, a single mode can be seen at the beginning of the experiment (0 min). After 4 min of excitation, the intensity of the mode has increased. However, it decreases with each following step until the mode is no longer visible after 20 min. A blue-shift of the mode by 4 meV is observed over the course of this experiment.

The mode spectrum shown in Figure 5.27b is more complex at 0 min, as two overlapping modes can be observed near 2.638 eV and a third mode near 2.648 eV. Over the course of the measurement, the intensity of the overlapping modes is quickly reduced, after 4 min the modes are barely visible. It is notable that the higher-energy mode of the overlapping structure appears to be more resistant against degradation, as the structure of two peaks changes to a single mode in favor of it during the degradation. The behavior of the third mode near 2.648 eV is similar to the mode seen in Figure 5.27a, its intensity increases in the beginning of the experiment, a maximum is found at 3 min. After 7 min, all modes are

hardly visible in the spectrum. For both analyzed disks, no modes were observed after the measurements shown in Figure 5.27 concluded. This was also tested several days after the degradation occurred, which shows that the damage to the disks is not easily reversible. It is notable that the background emission intensity is not affected by the degradation and remains constant. Spontaneous emission is commonly still observed from ZnSe-based laser structures after modes degraded [121], this indicates that only a limited part of the microdisk resonator (and possibly only a limited number of halogen impurities) is affected by the degradation.

The comparison of the two experiments in Figure 5.27 shows that the starting mode intensity is higher in the measurement with doubled excitation density. However, the degradation of the modes also happens faster (by about a factor of 3) under increased excitation. A blue-shift of the modes is observed in both measurements, additionally Figure 5.27b indicates that modes with higher energies degrade more slowly.

The increase of the mode intensity at the beginning of the experiment can be explained by desorption of molecules from the disk edge. These have been adsorbed before the experiment, especially in the cooling process preceding measurements at cryogenic temperatures. Their desorption when the exciting laser heats the sample improves the optical quality of the resonator, thereby increasing its ability to form modes. This was previously described for III-nitride disks [122].

The shift of the modes can be explained by slight changes of the refractive index of the microdisk due to the excited carriers, as was discussed above. The shift observed in Figure 5.27a under excitation with $780 \frac{\text{W}}{\text{cm}^2}$ is comparable to the shift observed in Figure 5.5 where a microdisk on sample A ($d_{\text{disk}} = 3.3 \mu\text{m}$) was excited with up to $2420 \frac{\text{W}}{\text{cm}^2}$. In the latter measurement, the microdisk is not excited continuously, but only for a short time while the spectra are recorded. Due to this, the average concentration of excited carriers is lower at the same excitation density. This explains why the shift is comparable even though the excitation density is larger.

The ‘favoring’ of higher energy modes in the degradation process can be explained by a slight blue-shift of the QW emission due to the loss of some of the halogen impurities as they are converted to nonradiative recombination centers.

The effect of an increase of temperature on the modes can be seen in Figure 5.28. Here, a disk with a diameter of $4.3 \mu\text{m}$ was excited with the same excitation density at different temperatures. The experiment is confined to the temperature range from 11 to 36 K, because no modes were observed at higher temperatures.

The spectra show two modes at about 2.63 and 2.645 eV. With rising temperature, these modes shift to lower energies. The intensity of the mode at 2.63 eV increases, while the

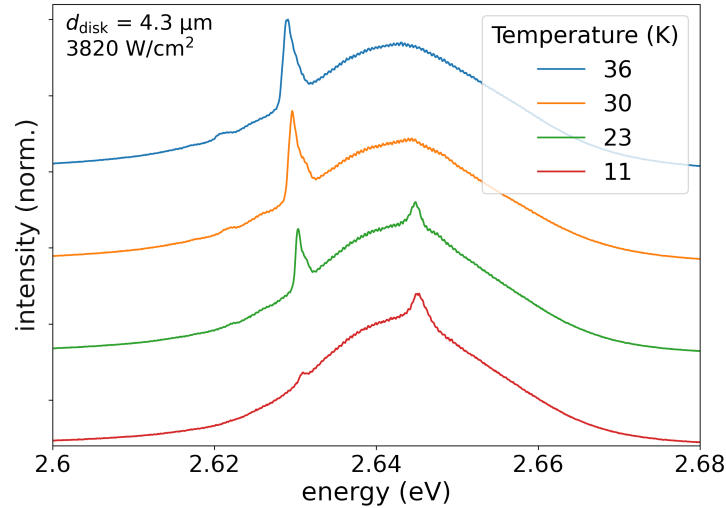


Figure 5.28: μ PL spectra of a free-standing microdisk with a diameter of $4.3 \mu\text{m}$ taken at different temperatures between 11 and 36 K. All measurements were recorded with the same excitation density of $3820 \frac{\text{W}}{\text{cm}^2}$. Spectra are normalized to their maximum and vertically shifted for better visibility.

intensity of the other mode decreases.

This is in stark contrast to the spectra recorded under continuous excitation shown in Figure 5.27, which showed a blue-shift of modes and a ‘favoring’ of higher energy modes. The red-shift of emission leading to said ‘favoring’ of low energy modes in Figure 5.28 is expected for rising temperatures, as the increased movement of the atoms leads to a larger average lattice constant, which decreases the bonding strength.

Due to the described differences, the results in Figure 5.28 show that the observed blue-shift of mode positions under continuous excitation cannot be explained by a change of the disk diameter due to heating. From that, it can be concluded that the degradation of disks discussed in this section cannot be explained by a general increase of their temperature. The conversion of halogen impurities into nonradiative recombination centers, as discussed above, better explains this phenomenon.

In conclusion, this section provided a more in-depth analysis of the degradation of intensity that is observed for WGMs growing on the QW emission of free-standing microdisks due to stimulated emission. It is plausible that the intensity loss is caused by the formation of local defects at sites where the mode propagation leads to strong fields in the resonator. The different degradation times observed for strongly doped and δ -doped ZnCdSe QWs suggest that the formation of these defects is connected to the halogen impurities. The observed blue-shift of the modes can be explained by a change of the refractive index of the sample induced by excited charge carriers.

The direct contact to the substrate of the supported microdisks analyzed in the following section should lead to a better mechanical stability and thermal contact. This could reduce the degradation, due to an improved dissipation of heat generated at the disk boundary and a uniform strain of the QW across the microdisk.

5.3. Supported Microdisk Resonators with δ -type Halogen Impurities

In this section, microdisks in the supported geometry on sample C (for an overview of all samples used for measurements in this work see Table 4.1 on page 31) are introduced. A ZnSe:Cl QW with a thickness of 4 nm and a dopant concentration of $3 - 4 \cdot 10^{16} \text{ cm}^{-3}$ was fabricated embedded in 36 nm-thick $\text{Zn}_{0.91}\text{Mg}_{0.09}\text{Se}$ barriers. This structure was grown on a layer of AlAs which was later oxidized to Al_2O_3 , as described in Section 4.1. This process has not been applied to ZnSe-based materials before.

The fabrication parameters and details important to the analysis discussed here are recounted in the next section. In the following analysis of these disks, the optical characterization via μPL will play a large role. At first, an analysis of the emission near the band edge at low temperatures will allow for a comparison with the measurements of free-standing disks described above. This is followed by a broader analysis of the luminescence at room temperature, which reveals that WGMs can be observed on the defect emission. The analysis of these disks ends with an assessment of their structural quality based on their deformation functions that are extracted from SEM images.

5.3.1. Advantages and Drawbacks of the Supported Geometry

The enhanced contact of the supported microdisks to their substrate could reduce thermal problems, which are often observed in free-standing microdisks [19, 40, 97] and thus lead to a lower degradation of the resonators under excitation. A possible downside of this resonator structure is the reduced refractive index contrast at the bottom of the microdisk, as the refractive index of bulk Al_2O_3 is about 1.78 at 2.7 eV [123], although it can be lower for Al_2O_3 at lower densities, e.g., after ALD growth [124]. This is significantly closer to the refractive index of the ZnSe-based material (about 2.5, based on the simulations in Section 5.1.2) than the vacuum that is found under the edge of the free-standing disks ($n = 1$). This will lead to a higher leakage of modes into the substrate and higher losses which will reduce the observable Q -factors. Previous works estimate a reduction of the Q -factor between 20 % [91] and 33 % [19], depending on the refractive index contrast. However, the increased mechanical stability of the resonators could counteract these losses in optical quality and lead to an increase of the Q -factor by preventing bending of the microdisk out

of plane and providing a more uniform strain across the disk.

For a better orientation on the sample so-called ‘markers’ are fabricated along with the microdisks in the processing of the MBE grown layers as described in Section 4.1. These markers are typically oval with a width of about $40\ \mu\text{m}$ and $20\ \mu\text{m}$ along the symmetry axes. These (for the purpose of μPL measurements) large and non-round (i.e., not easily supporting WGMs) areas of the ZnSe-based material can be used to characterize the emission from the QW without the influence of the resonator structure.

Because of their size, the markers are not fully underoxidized, which allows for a comparison between the emission of the QW on an AlAs and an Al_2O_3 substrate. This incomplete underoxidation can be confirmed by SEM images which show a change in contrast at a distance of about $10\ \mu\text{m}$ from the edge of the marker.

5.3.2. Near Band Edge Emission at Low Temperatures

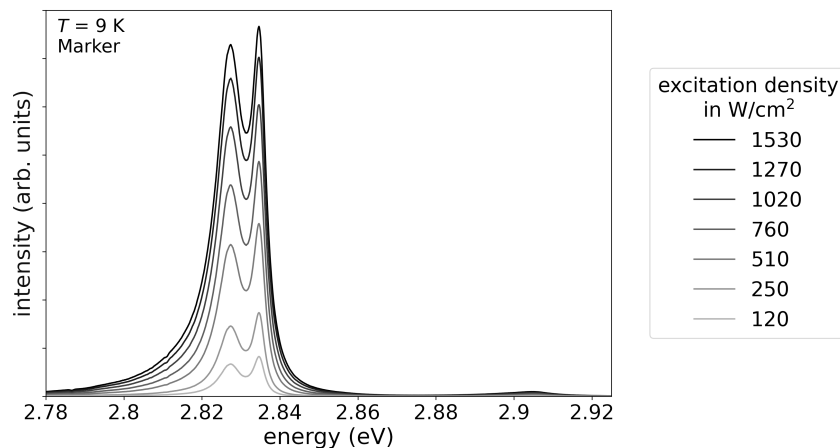


Figure 5.29: Series of μPL spectra with rising excitation density of a ZnSe:Cl QW in $\text{Zn}_{0.89}\text{Mg}_{0.09}\text{Se}$ barriers on an AlAs substrate.

Figure 5.29 shows a series of spectra recorded at different excitation densities in the middle of a marker, i.e., on an AlAs substrate that was not affected by the oxidation process. Two clear maxima can be observed between 2.82 eV and 2.84 eV, a comparably faint maximum is seen near 2.91 eV. The emission does not seem to change with the change in excitation density, except for a general increase of intensity. Specifically, the ratio of intensity of the two intense maxima does not change over the course of this measurement.

The main emission maxima correspond to the recombination of free excitons (FX, 2.84 eV) and excitons trapped at the Cl impurities (D^0X , 2.82 eV) in the QW [14]. The fact that their intensity ratio does not change, although the amount of Cl impurities trapping excitons is limited, reveals that the emission at these defects must be very efficient, i.e., the excitons recombine quickly after being trapped. The emission at 2.91 eV corresponds

to recombination in the $\text{Zn}_{0.89}\text{Mg}_{0.09}\text{Se}$ barriers [125]. The emission is significantly weaker compared to the QW emission, since many excited charge carriers move to the energetically favorable QW before recombination.

Additionally, the layer below the ZnSe-based structure has an influence on the emission, as is demonstrated by a line scan measurement over the longer symmetry axis of a marker.

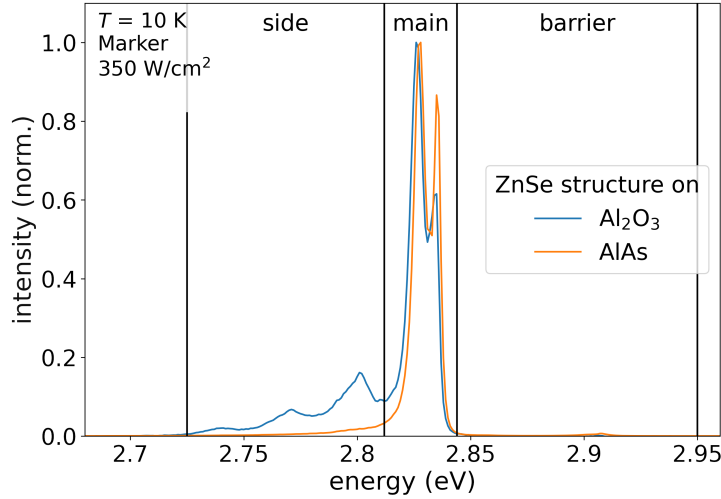


Figure 5.30: Two μPL spectra recorded by exciting different positions on a marker with an excitation density of $350 \frac{\text{W}}{\text{cm}^2}$, normalized to the intensity of the D^0X emission line. The spectra are separated into three sections for analysis, marked by the vertical black lines.

Figure 5.30 shows two spectra which are part of this line scan measurement. The blue spectrum was recorded while exciting near the edge of the marker, for the orange spectrum its center was excited. As the marker is not completely underoxidized, the orange spectrum corresponds to the emission of the ZnSe-based QW structure on an AlAs layer while the blue spectrum stems from a QW on Al_2O_3 . Both spectra are normalized to the maximum of their intensity for better comparison, as the spectrum from the center of the marker is more intense. The spectrum recorded on AlAs is similar to the spectra observed in Figure 5.29.

The emission can be separated into three spectral areas marked by black lines in the figure: Emission from the ZnMgSe barriers ($2.95 - 2.84 \text{ eV}$), emission from the QW ($2.84 - 2.81 \text{ eV}$), and side band emission ($2.81 - 2.725 \text{ eV}$) of the QW. The side bands can only be observed in the spectrum recorded for QWs on Al_2O_3 .

This means that these side bands either occur because of the Al_2O_3 underlayer, or their intensity saturates at a low values and is eclipsed by the QW emission in the more intense spectrum in Figure 5.30. Figure 5.31 illustrates the integrated intensity of the three areas for all spectra recorded in the line scan as a function of position. Because of the differences

in intensity between the three regions, they were normalized to their respective maximum.

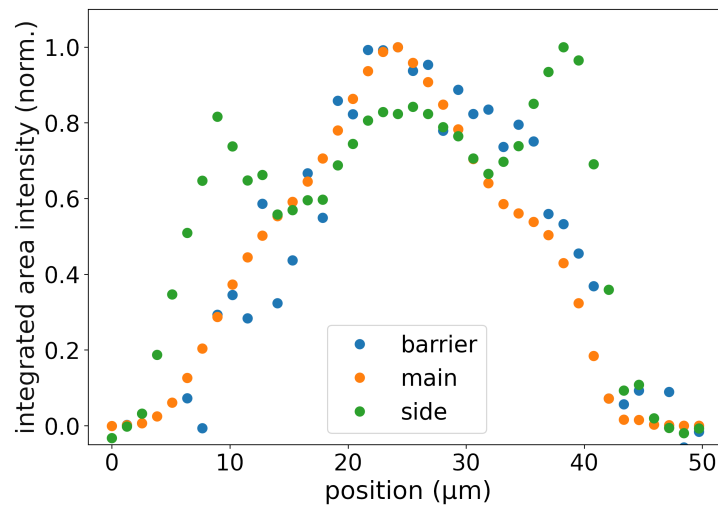


Figure 5.31: Integrated intensity of the three areas of the μPL spectra defined in Figure 5.30 as a function of the position of the excitation spot on the analyzed marker. Data for each section is normalized to the respective maximum.

The barrier and the main emission intensity show a similar trend over the whole measurement with a maximum at the center of the line scan. The slope of this intensity growth is reduced about halfway between the center and edge of the marker which can be seen well near $35\ \mu\text{m}$. The side band emission intensity is low at the edge of the marker as well, but then shows stronger increase compared to the other areas. It drops at the position at which the slope of the main and barrier emission intensities is reduced and then grows again, as it follows their trend in the central $10\ \mu\text{m}$ of the marker.

The barrier and main emission intensities are mostly dependent on how much material can be excited by the laser, which is maximal in the center of the marker. Their reduced intensity growth coincides with the border between the unoxidized AlAs and the Al_2O_3 in the layer below the ZnSe-based material, the intensity loss might therefore be due to nonradiative recombination at defects that occur at this interface.

The side band emission is only visible in areas where the QW structure is on Al_2O_3 . On AlAs (in the central region of the marker), only the tail of the main QW emission is measured in the spectral region labeled ‘side bands’, which is why the intensities correlate. This can be better seen in Figure 5.32 where the ratio of the side band to the ‘main’ emission intensity is plotted as a function of position in the line scan.

For spectra recorded very close to the edge of the marker no meaningful ratios could be computed due to the low intensity of the emission.

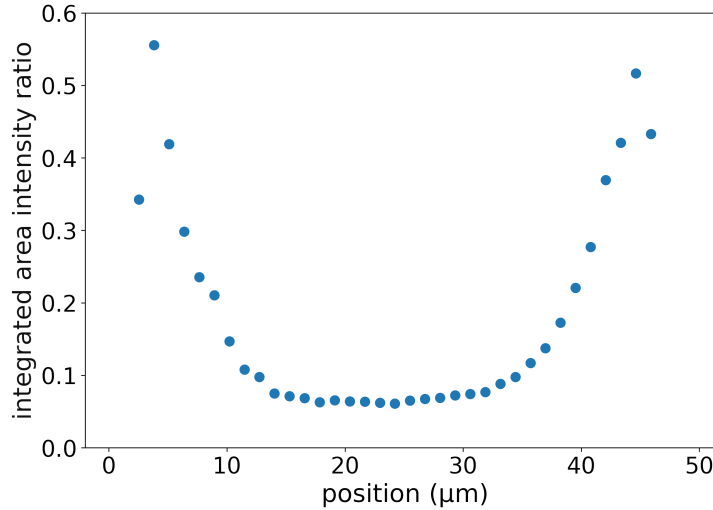


Figure 5.32: Ratio of the integrated intensity of the side bands to the ‘main’ QW emission as a function of the position of the excitation spot on the analyzed marker.

Near the boundary of the marker the ratio grows to > 0.5 and then quickly drops to about 0.06, which is reached at the positions where the main intensity grows with a smaller slope (compare Figure 5.31). The ratio is constant in the middle of the marker.

This data shows that the side bands are visible only on Al_2O_3 , their visibility reduces when the QW emission increases, since the tail of the QW emission on its low energy side masks the side bands. Based on this, the side bands might be explained as a multilayer interference effect that occurs on Al_2O_3 because of the different refractive index compared to AlAs. However, maxima occurring due to such an interference effect would usually be more symmetric in the spectrum. Another possible source of this side band emission could be the occurrence of phonon replica. In this effect, the excess energy in the recombination process is emitted not only as a photon, but one or more phonons are created as well. Accordingly, the energy of the emitted photon is reduced by one or multiple phonon energies of the material. The spacing of the side bands observed here (about 30 meV) fits well to the energy of the LO phonon of ZnSe at the Γ -point [126], emphasizing that these bands might be phonon replica. A further characterization of this side band emission based on the spectra of microdisks with different diameters and measurements at various temperatures will be given at the end of this section.

In SEM images of microdisks, it can be noticed that they are fully underoxidized for all sizes. Therefore, the QW structure is on top of Al_2O_3 and side band emission is observed for all disks, as will be seen in the following.

Figure 5.33 depicts an overview spectrum of a disk with a diameter of $4.5 \mu\text{m}$ at different excitation densities, comparable to the spectra from the center of a marker given in Figure

5.29.

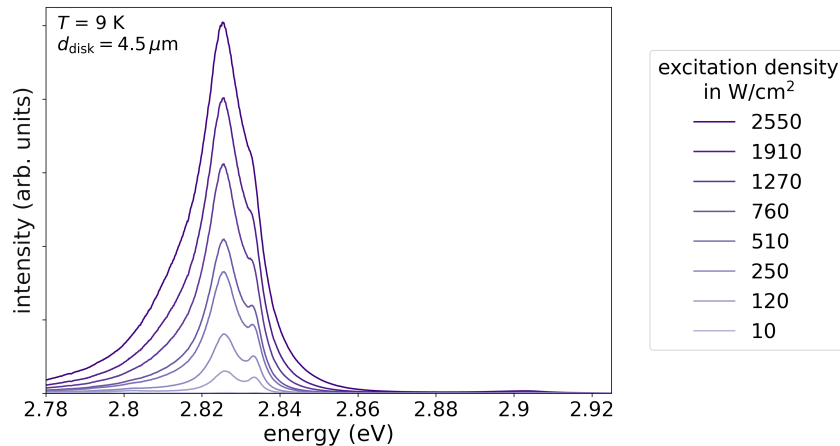


Figure 5.33: Series of μ PL spectra with rising excitation density of a supported microdisk with a diameter of $4.5 \mu\text{m}$, similar to the measurement of the emission from a marker in Figure 5.29.

In the spectra recorded on disks, the same features can be found that were discussed for the spectra of the ZnSe-based marker, namely the two QW emission maxima between 2.82 (D^0X) and 2.84 eV (FX) and the faint barrier emission near 2.91 eV. Concerning the changes of the spectra with rising excitation density, the D^0X emission maximum exhibits a clearly stronger growth than the FX emission. From that it is obvious that (non-radiative) surface recombination of the free excitons occurs in the microdisks [14]. This was not observed on the center of the marker, due to the large distance between the excitation spot and any edges (i.e., exposed side facets of the QW) of the ZnSe-material. As discussed above, side band emission can be observed on the low-energy side of the QW emission of microdisks.

Figure 5.34 shows spectra taken by exciting the same disk as for Figure 5.33, but here lower excitation densities were used and a slightly different part of the spectrum was measured in order to analyze the low-energy side of the QW emission. The broad side emission bands are found around 2.77 and 2.8 eV. This emission is more clearly visible when the disk is excited with lower excitation densities. Additionally, two small modes can be observed in this emission region, only little growth on the background emission is registered from them. Figure 5.35 shows a zoom of the spectra with emphasis on these modes.

Two modes can be seen on the low-energy side of the 2.80 eV side emission band at about 2.79 eV (MI) and 2.798 eV (MII); these names were assigned to them for a better distinction. This appears to be similar to the free-standing disks with δ -type impurities (sample B) that showed modes occurring on the low-energy side of the emission at low

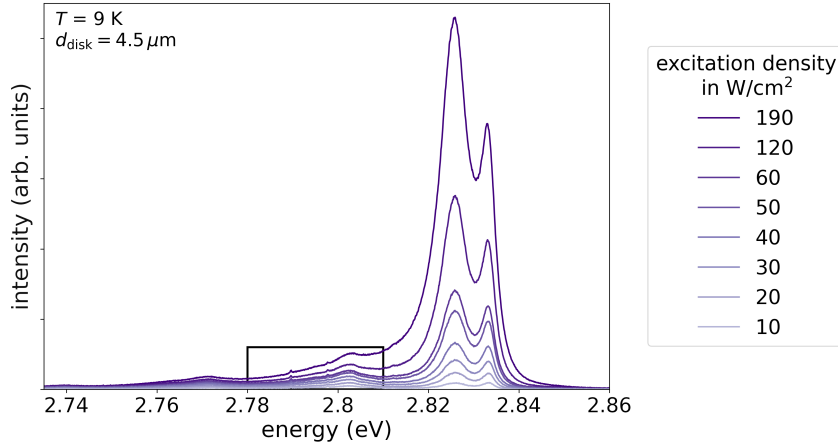


Figure 5.34: Series of μPL spectra with rising excitation density of a supported microdisk with a diameter of $4.5 \mu\text{m}$. These spectra were taken on the same disk as the spectra in Figure 5.33, but with significantly lower excitation density. A slightly different part of the spectrum is given. The black rectangle marks the part of the spectrum that is shown in detail in Figure 5.35.

excitation densities in the previous section. The maximum Q -factors observed for the modes are very high (≥ 7900). This is slightly higher than the Q observed for modes at comparable positions in free-standing disks on sample B (Figure 5.15). This proves that resonances with low losses are possible in the supported disks, although the refractive index contrast at the bottom of the disk is reduced.

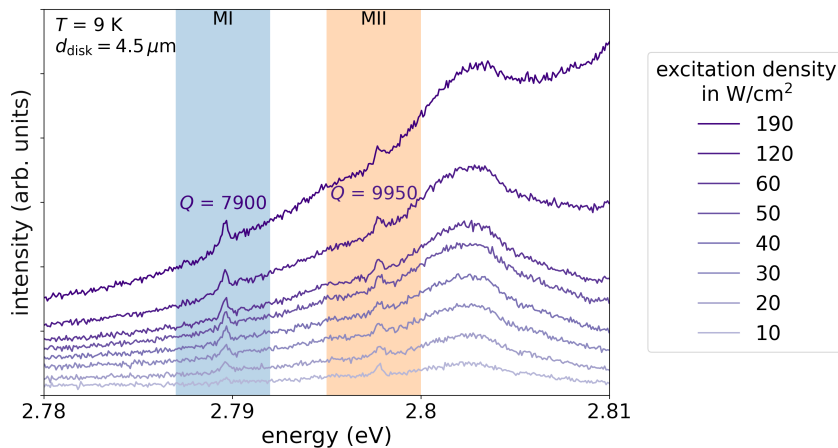


Figure 5.35: Zoom of the series of μPL spectra with rising excitation density of a supported microdisk with a diameter of $4.5 \mu\text{m}$ given in Figure 5.34. The maximum Q -factor for each of the observable modes is indicated in the figure.

Figure 5.36 shows the intensity of the two modes as a function of excitation density. For both the intensity grows linearly at low excitation followed by saturation. This saturation sets in at about $60 \frac{\text{W}}{\text{cm}^2}$ for MI and $20 \frac{\text{W}}{\text{cm}^2}$ for MII.

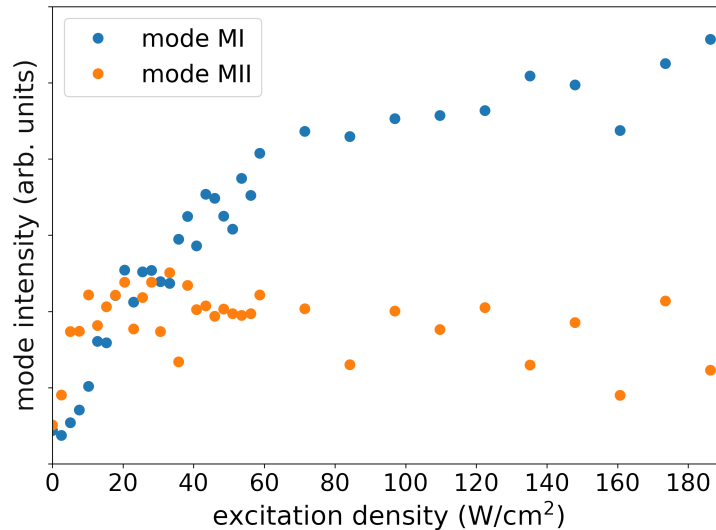


Figure 5.36: Integrated intensity of the modes observed in Figure 5.35 as a function of excitation density. The color of the markers corresponds to the colored columns marking the modes in Figure 5.35.

This is again similar to the modes observed for free-standing disks. The reduction of the mode intensity when the background emission starts to grow faster than the mode is likely not observed here, because it occurs at higher excitation densities. This assumption is supported by the observation that the modes seen in this measurement do not occur at high excitation densities, compare Figure 5.33.

No stimulated emission is found for these modes due to the low gain of the active region of the microdisk resonator at their spectral position, but the presence of the modes demonstrates that it is possible for WGMs to form in the supported microdisks.

Figure 5.37 plots the spectral position and width of the modes as a function of excitation density. Both the position and FWHM of MI are stable after the initial phase of low intensity, where the parameters scatter strongly. MII shows a scattering of both parameters in the beginning as well, towards higher excitation densities both the position and width of this mode decrease slightly.

These plots reveal the limitations of the detection and subsequent fit of the modes, which yields inconsistent results at very low intensities. This is why the parameters extracted for excitation densities just above the value at which the modes appear on the background emission cannot be used for further analysis. Mode MI is more intense compared to the background in the spectra in Figure 5.35 which is why the fitting results scatter less.

In conclusion, probable WGMs were detected for this disk, similar to the small modes observed for δ -type doped free-standing disks on sample B in Section 5.2.1. Their high Q -factors show the good optical quality of the resonator.

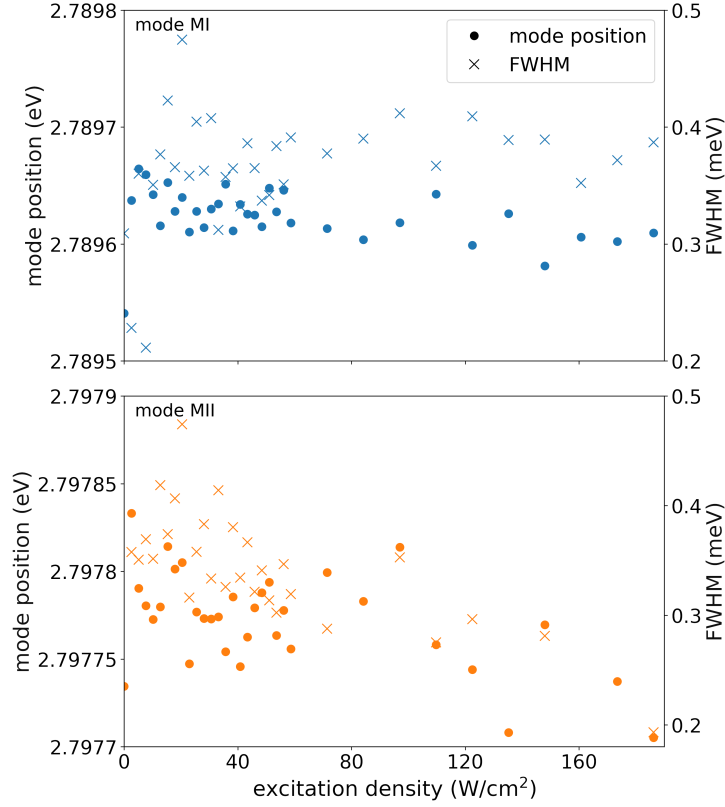


Figure 5.37: Spectral position (circles, left axis) and FWHM (crosses, right axis) of the modes observed in Figure 5.35 as a function of excitation density. The color of the markers corresponds to the colored columns marking the modes in Figure 5.35. Data for each mode was plotted in a separate subplot for better visibility.

A different disk of the same size ($d_{\text{Disk}} = 4.5 \mu\text{m}$) was analyzed to confirm the detection of the modes shown above. For this measurement, the exciting laser system producing 100 fs pulses (see Section 4.3) was exchanged for a 409 nm laser diode in cw operation. This reduces the maximal energy that excites the microdisk at the same excitation density, because it eliminates the intense laser pulses. However, the time between the exciting pulses, which could lead to the diffusion of accumulated heat, is no longer present under cw excitation. This might be less important for the supported disks due to their improved thermal contact to the substrate. Excitation with a cw laser source is tested in order to see if this influences the spectra of the microdisks. This is especially important here, because the setup used to measure the overview spectra of these supported disks seen in Section 5.3.3 is limited to excitation with a cw source.

A series of μPL spectra of a microdisk, with the same diameter that was analyzed under pulsed excitation in Figure 5.33, was recorded under cw excitation. The resulting spectra

are very similar to those under pulsed excitation, although the excitation density needed to record the spectra is higher for cw excitation. The FX and D⁰X emission lines can be observed as well as the side bands. Modes are found below the QW emission, especially on the low-energy side of the first side band. A zoom into the region where modes are observed is depicted in Figure 5.38. Seven probable modes can be seen in the spectra at about 2.790 eV (two close modes), 2.798 eV, 2.801 eV, 2.806 eV, 2.812 eV, and 2.817 eV. The two most intense modes show a significant growth on the background. They are labeled MI' (2.790 eV) and MII' (2.798 eV), analogous to modes MI and MII observed in the emission spectra of a microdisk with the same diameter under pulsed excitation.

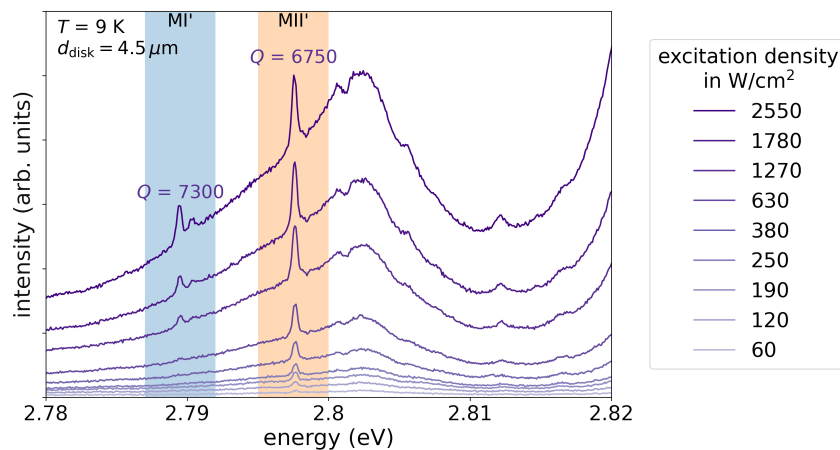


Figure 5.38: Zoom of a series of μ PL spectra with rising excitation density of a supported microdisk with a diameter of $4.5 \mu\text{m}$ under cw excitation. A disk with the same diameter was investigated under pulsed excitation in Figure 5.35. The maximum Q -factor for the two most intense modes is indicated in the figure.

The intensity, position and width of these modes will be analyzed more closely in the following, analogous to previous modes. For this, it is important to note that while MII' is visible in all measurements, MI' only occurs at excitation densities above $300 \frac{\text{W}}{\text{cm}^2}$ and is harder to fit because of its proximity to the neighboring mode. Again, high Q -factors are observed, which are, however, lower than the Q -factors of the disk under pulsed excitation (compare Figure 5.35).

The intensity of both modes is displayed as a function of excitation density in Figure 5.39. Mode MI' shows a slow growth with rising excitation density and two 'jumps' near $1300 \frac{\text{W}}{\text{cm}^2}$ and $2000 \frac{\text{W}}{\text{cm}^2}$. For MII', the intensity demonstrates a linear growth over a large range up to about $1400 \frac{\text{W}}{\text{cm}^2}$ and a tendency towards saturation at the highest excitation densities in this measurement.

These results are comparable to the integrated intensity of similar modes observed under pulsed excitation. The spectral position of these modes does not support lasing due to the

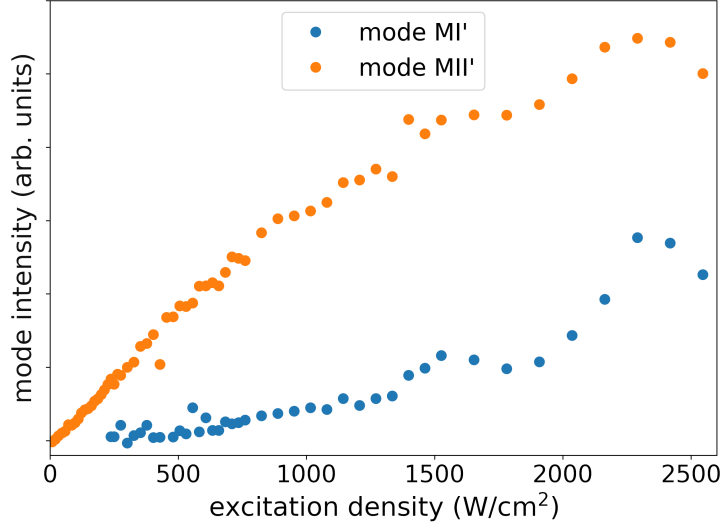


Figure 5.39: Integrated intensity of the modes observed in Figure 5.38 as a function of excitation density. The color of the markers corresponds to the colored columns marking the modes in Figure 5.38.

low gain, but the low intensity of the side band emission allows them to become visible.

Regarding their position and width (Figure 5.40), both modes show an initial scattering of both parameters as seen for other modes above, followed by stabilization with a slight red-shift of the mode position (< 0.1 meV in both cases).

The modes appear to be stable, the slight red-shift might be due to heating of the sample, which is better observable in this measurement because of the higher excitation density and continuous excitation as described above. Given that excitation densities above $2500 \frac{\text{W}}{\text{cm}^2}$ are used in this measurement, it is notable that no blue-shift of the modes is seen, as was the case for WGMs on samples A and B. This could be a hint towards an increased stability of the resonators in the supported geometry. However, the excitation for free-standing disks was pulsed and the analyzed modes showed significant growth via stimulated emission, which makes a comparison between these measurements difficult.

The spectral positions of the modes are similar to the positions of the modes MI and MII in Figure 5.35, where a disk of the same size is analyzed. This shows the high quality of the fabrication process of the disks, as modes can be reproduced between different disks, which was not the case for free-standing resonators (compare Figure 5.9). This reproducibility will be further analyzed with regard to resonances on the defect luminescence in Section 5.3.3.

The stability of the modes against continuous excitation with a pulsed or cw laser source is analyzed in measurements on the same disk with a diameter of $3.5 \mu\text{m}$. Figure 5.41 shows a series of μPL spectra taken at different excitation densities while exciting the disk

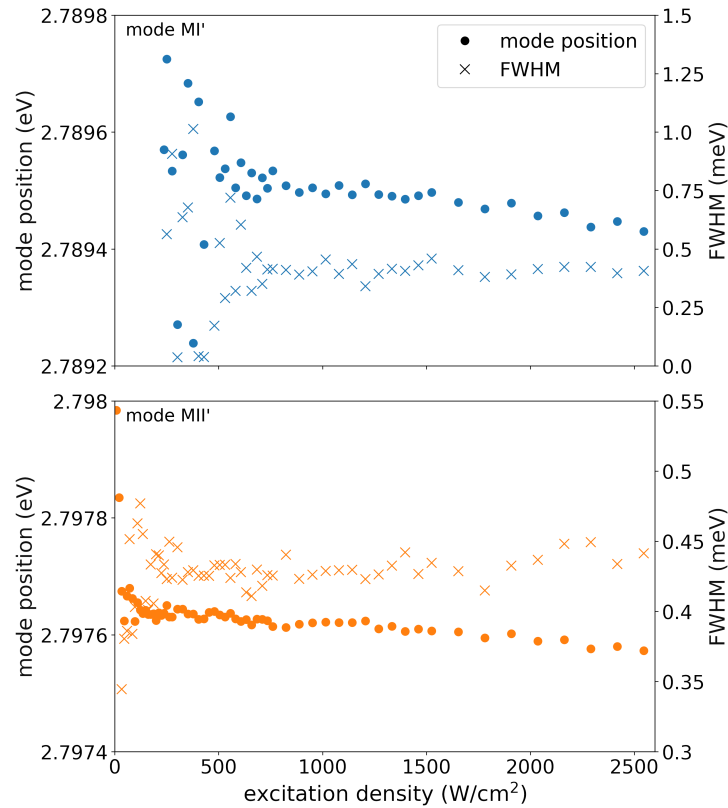


Figure 5.40: Spectral position (circles, left axis) and FWHM (crosses, right axis) of the modes observed in Figure 5.38 as a function of excitation density. The color of the markers corresponds to the colored columns marking the modes in Figure 5.38. Data for each mode was plotted in a separate subplot for better visibility.

with a pulsed laser source. Two small modes can be observed at 2.80 eV and 2.81 eV.

These spectra reveal that the mode positions, which could previously be reproduced for two disks with $d_{\text{disk}} = 4.5 \mu\text{m}$, change with the disk's radius. This is a clear sign that these modes might be WGMs. The stability of the mode in the minimum between the D^0X emission and the first side band near $2.81 \mu\text{m}$ is analyzed in the measurement shown in Figure 5.42.

The spectra look fairly unchanged over the whole 20 min measurement, no decrease of intensity or shifts of modes can be observed. It should be noted that the excitation density used for this measurement is lower than the excitation density in the same experiment on sample B (Figure 5.27), as the small mode analyzed here occurs at lower excitation. A more detailed analysis of the parameters of the observed mode was performed by fitting it with a Gaussian and extracting its intensity, position and width.

No changes of these parameters are observed over the 20 min measurement, they appear to be stable. The average Q -factor of the mode in all recorded spectra is 5400. As discussed

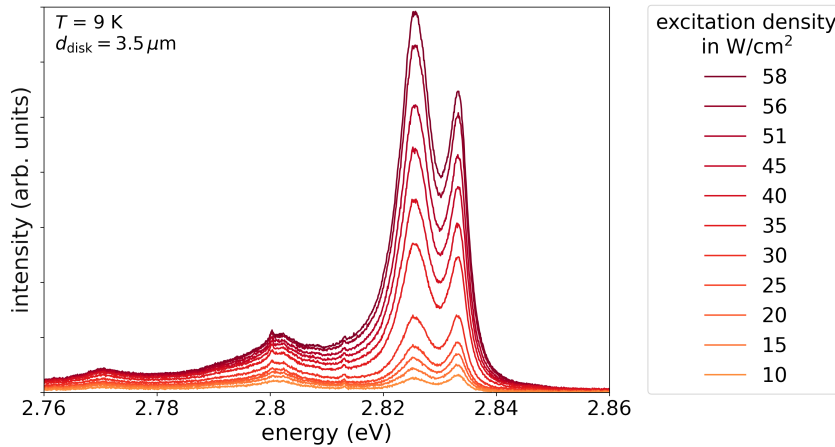


Figure 5.41: Series of μ PL spectra with rising excitation density of a supported microdisk with a diameter of $3.5 \mu\text{m}$.

before, the disk shows no sign of degradation, this stability might be aided by the low excitation density.

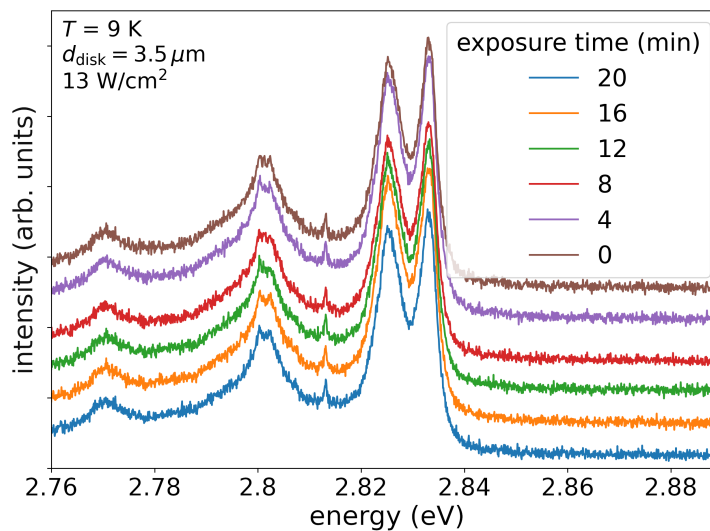


Figure 5.42: Series of μ PL spectra of the supported microdisk with a diameter of $3.5 \mu\text{m}$ analyzed in Figure 5.41. The spectra were taken at different times while continuously exciting the microdisk with an excitation density of $13 \frac{\text{W}}{\text{cm}^2}$.

For a further analysis of stability, the sample was warmed up to room temperature and cooled down to cryogenic temperatures for a second measurement under continuous excitation. In this second stability assessment a 409 nm cw laser diode was run as exciting light source.

As observed for the measurements of disks with a diameter of $4.5 \mu\text{m}$ above, the spectra under cw excitation (of which a zoom can be seen in Figure 5.43) are similar to the spectra observed under pulsed excitation (Figure 5.41). The same modes can be seen, one in

the minimum near 2.81 eV (labeled $M\beta$) and an additional mode at 2.80 eV ($M\alpha$) that was visible in the previous experiment, but is more intense here. As the modes are more pronounced under cw excitation, their properties are determined by a fit with a Gaussian to allow for a comparison to the modes MI' and MII' , which were observed from a disk with a larger diameter.

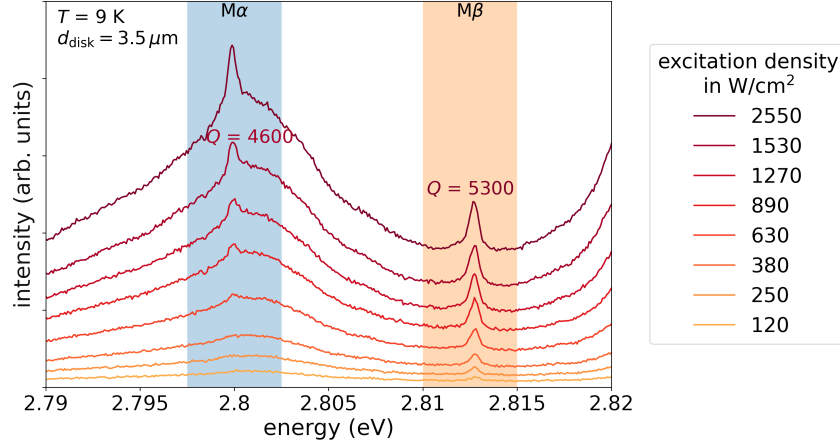


Figure 5.43: Zoom of a series of μ PL spectra with rising cw excitation density of the supported microdisk with a diameter of $3.5 \mu\text{m}$ analyzed in Figure 5.41 under pulsed excitation. The maximum Q -factor for each of the observable modes is indicated in the figure.

Both modes show a high Q -factor (around 5000) that is lower than the Q -factors observed from supported microdisks with a diameter of $4.5 \mu\text{m}$. The quality factors are comparable to the Q of 5400 that was observed from a mode at the same spectral position as $M\beta$ for the measurement under continuous pulsed excitation on the same disk. The mode's intensities are plotted as a function of excitation density in Figure 5.44. Mode $M\alpha$ is only included in this analysis after it appears in the measurement and can be fitted by a Gaussian at excitation densities above $1000 \frac{\text{W}}{\text{cm}^2}$.

In Figure 5.44, both modes show a linear growth of their intensity with rising excitation density, $M\beta$ saturates at high excitation.

This disk ($d_{\text{disk}} = 3.5 \mu\text{m}$) shows the same behavior of the small modes as was previously observed for larger disks, this can also be seen in Figure 5.45, where the position and FWHM of $M\alpha$ and $M\beta$ are plotted as a function of excitation density.

The position and width of mode $M\alpha$ scatter at lower excitation densities, where the mode starts to appear on the background band, at higher excitation densities the mode's parameters stabilize. Mode $M\beta$ shows a slight red-shift of its position with a stable FWHM.

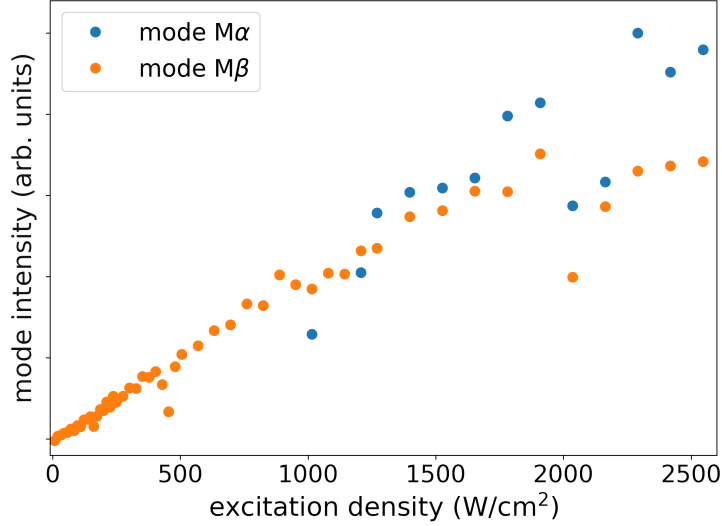


Figure 5.44: Integrated intensity of the modes observed in Figure 5.43 as a function of excitation density. The color of the markers corresponds to the colored columns marking the modes in Figure 5.43.

As mentioned above and observed for disks with a diameter of $4.5\mu\text{m}$, the cw excitation does not seem to affect the small modes observed in the spectra except for a slight red-shift that can be explained with the heating of the sample by the exciting laser. No signs of degradation can be observed in this measurement, the stability of the mode $M\beta$ under continuous cw excitation for 20 min is analyzed in the measurement shown in Figure 5.46.

This measurement is comparable to Figure 5.42. Here the same disk was analyzed, but excited with a cw laser diode at $130 \frac{\text{W}}{\text{cm}^2}$, the higher excitation density is needed because of the cw excitation. The spectra and especially the mode in the minimum near 2.81 eV appear to be stable, as no shifts or changes in intensity, width, or position of the mode can be observed over the course of the 20 min measurement. This shows that the mode is stable over a second measurement with continuous excitation, however, the excitation density that was used here is still relatively low compared to the excitation densities used for the measurement under continuous excitation on sample B (Figure 5.27). No stimulated emission occurs here.

The average Q -factor in this measurement is 4900, is slightly lower compared to the stability test of this resonator with pulsed excitation, which showed an average Q -factor of 5400 over 20 min. This appears to be consistent with the observation that the small modes have a slightly higher Q -factor under pulsed excitation compared to cw excitation, but it should be noted that the disk was subject to heating to room temperature and cooling as well as several measurements between the two stability evaluations.

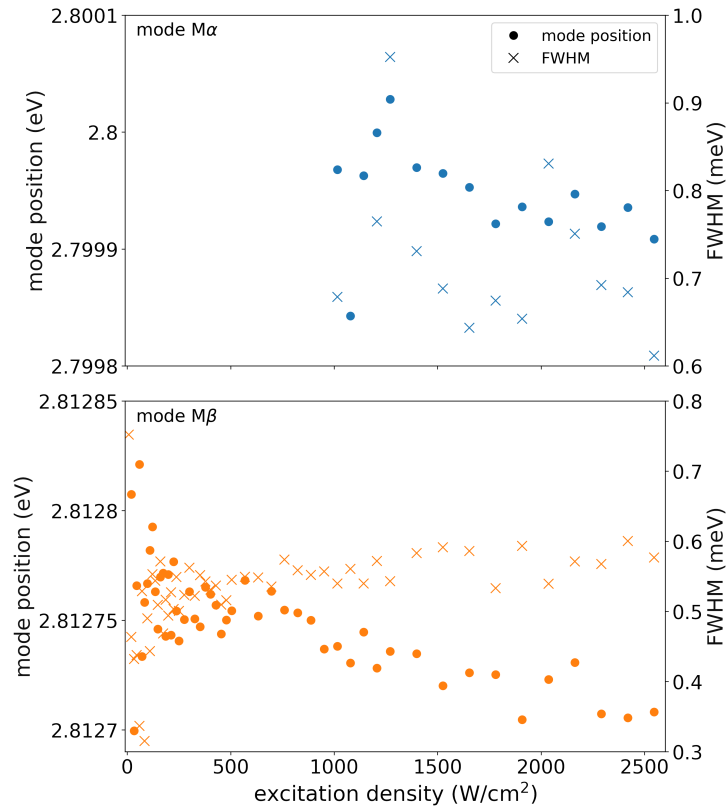


Figure 5.45: Spectral position (circles, left axis) and FWHM (crosses, right axis) of the modes observed in Figure 5.43 as a function of excitation density. The color of the markers corresponds to the colored columns marking the modes in Figure 5.43. Data for each mode was plotted in a separate subplot for better visibility.

As an interim conclusion, exciting the microdisk resonators with a cw laser diode does not seem to significantly alter the observed μ PL spectra compared to pulsed excitation. The same modes with similar stability and properties can be observed. However, the cw excitation requires higher excitation densities (averaged over time) and slightly reduces the Q -factors observed in the measurement, which might be connected to a stronger heating of the sample when the excitation is continuous. This reveals that μ PL spectra recorded under pulsed and cw excitation can be compared for these structures, which is especially important for the room temperature analysis presented in Section 5.3.3, as the setup used there is limited to cw excitation.

Changes of the QW (measured on a marker) and disk emission with temperature will be analyzed next, before overview spectra of the emission measured at room temperature are presented. The measurements discussed below were recorded with cw excitation of the material, since this reduces the experimental complexity and, as described above, the

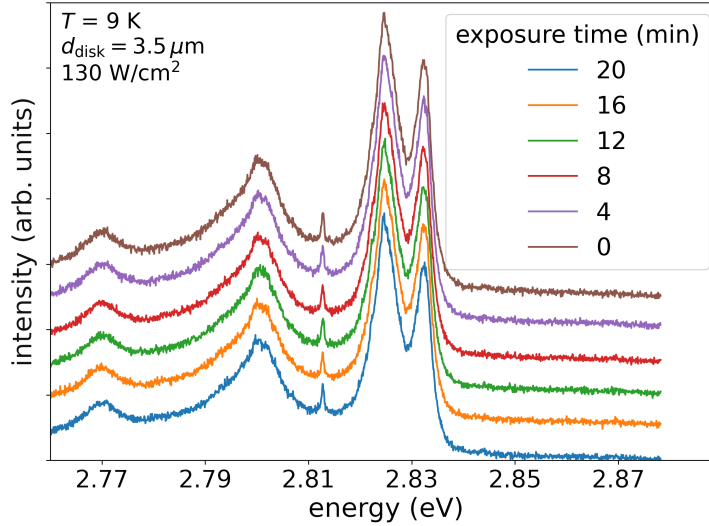


Figure 5.46: Series of μ PL spectra of the supported microdisk with a diameter of $3.5 \mu\text{m}$ analyzed in Figure 5.42, here excited with a cw laser diode. The spectra were taken at different times while continuously exciting the microdisk with an excitation density of $130 \frac{\text{W}}{\text{cm}^2}$.

overview spectra at room temperature need to be recorded with cw excitation due to limitations of the setup.

Figure 5.47 shows spectra of the near-band-edge emission of the QW at the center of a marker, i.e., on AlAs, at different temperatures from cryogenic (10 K) to room temperature (300 K). A clear red-shift of the emission can be observed. This is expected, the bandgaps of the materials shrink due to the increase of the average interatomic distances, which decreases the Coulomb interaction of the lattice atoms.

Some oscillations can be observed on the two emission lines of the quantum well, most prominently in the FX emission line in the measurements at 25 and 50 K. These artifacts occur because more than one spectrum had to be recorded in the μ PL setup described in Section 4.3 in order to record the whole spectral region displayed in Figure 5.47. The averaging of overlapping spectra introduces these oscillations.

At temperatures above 50 K, only one emission line of the QW emission can be seen, because the intensity of the D^0X emission line is reduced. This reduction develops when the thermal energy of the excitons is higher than the binding energy. At 200 K and above, another maximum at higher energy than the QW emission is found. This is the bandgap emission from the barrier, which is more prominent at room temperature since carrier mobility is reduced and less excitons reach the QW before recombination.

An artifact near 2.85 eV stems from the exciting laser diode and not the sample and can be neglected.

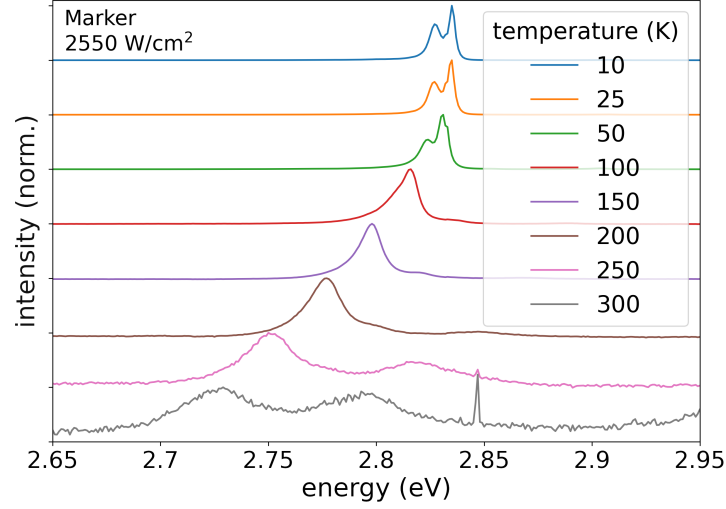


Figure 5.47: μ PL spectra of the center of a marker taken at different temperatures between 10 and 300 K. All measurements were recorded under the same excitation density of $2250 \frac{\text{W}}{\text{cm}^2}$. The spectra are normalized to their maximum and vertically shifted for better visibility.

In Figure 5.48 μ PL spectra of a supported microdisk with a diameter of $4.5 \mu\text{m}$ are plotted, similar to the spectra recorded while exciting a marker in Figure 5.47. Here the measurement was performed only up to a temperature of 250 K, because the emission intensity is very low at 300 K. The side emission bands can be observed in the measurement at 50 K, but no longer at 100 K and beyond, they will be analyzed in more detail in Figure 5.50. In accordance with the spectra recorded on the marker, the D^0X emission line is not visible at temperatures above 50 K. Barrier emission can be observed at higher temperatures. This emission band is less pronounced in these spectra, since no measurement at 300 K is plotted.

Increasing temperature seems to have the same effect on the QW emission bands of both the marker and microdisk. The width of the bandgap energy E_g as a function of temperature T can be modeled with the so-called Varshni equation [29], as discussed in Section 2.1.2:

$$E_g(T) = E_g(T = 0) - \alpha \frac{T^2}{T + \beta}. \quad (5.2)$$

α and β are fit parameters, β correlates with the Debye temperature. The emission line of the FX, which is the only QW emission line visible at higher temperatures, was fitted with Equation 5.2 for both measurements. The datapoints and fit can be seen in Figure 5.49, the extracted values for α , β , and $E_g(T = 0)$ are given in Table 5.2. There literature values for a relaxed ZnSe layer grown on GaAs [127] are given for comparison.

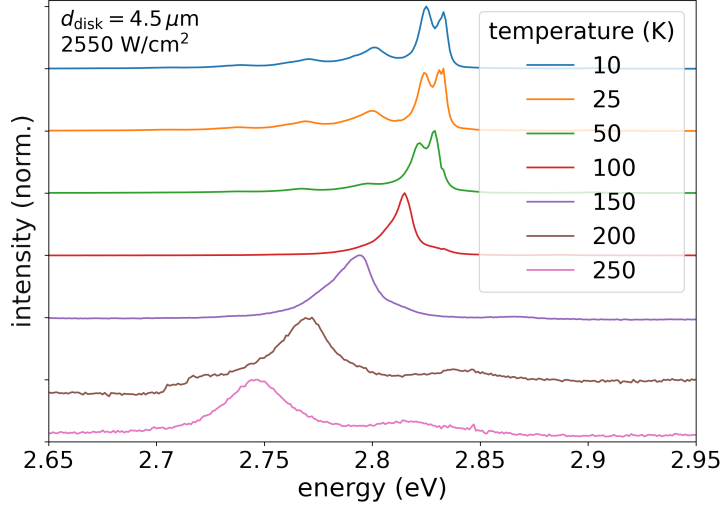


Figure 5.48: μ PL spectra of a supported microdisk with a diameter of $4.5 \mu\text{m}$ taken at different temperatures between 10 and 250 K. All measurements were recorded under the same excitation density of $2250 \frac{\text{W}}{\text{cm}^2}$. The spectra are normalized to their maximum and vertically shifted for better visibility.

	$E_g(T = 0)$ (eV)	α ($\frac{\text{meV}}{\text{K}}$)	β (K)
marker	2.836 ± 0.002	0.61 ± 0.08	199 ± 64
$4.5 \mu\text{m}$ disk	2.8337 ± 0.0005	0.89 ± 0.10	372 ± 68
bulk ZnSe [127]	2.800 ± 0.005	0.73 ± 0.04	295 ± 35

Table 5.2: Parameters estimated from the fits of the FX emission line position on AlAs (marker) and Al_2O_3 (disk) with Equation 5.2 shown in Figure 5.49 and comparison with literature values for bulk ZnSe.

Compared to the reference, the emission at $T = 0$ is blue-shifted in the spectra presented here. This increase of $E_g(T = 0)$ in comparison to the literature values is explained by the confinement effect. This increases the energy of an exciton that is confined to a small space in one or more dimensions, as is the case for excitons in the QWs in the analyzed structures. α and β are different for both measurements, the given literature values are between the two results from the marker and disk presented here.

The differences observed between the marker (ZnSe-based material on AlAs) and the disk (ZnSe-based material on Al_2O_3) might be explained by strain induced by the underlayer having an effect on the lattice parameters and especially their change with temperature.

In order to better understand the source of this part of the luminescence, the side emission bands on a supported disk with a diameter of $5 \mu\text{m}$ are depicted for different temperatures in Figure 5.50. The side bands are visible up to a temperature of about 60 K. As is observed for the QW emission lines, a slight red-shift of the side band position can be

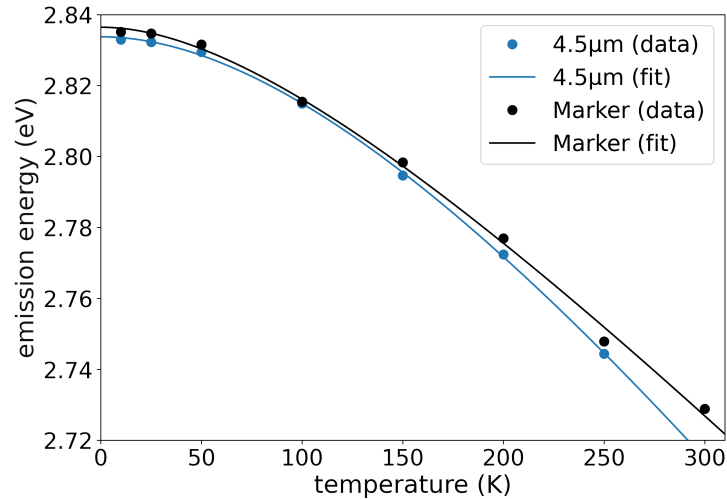


Figure 5.49: Varshni plot (spectral position of emission lines as a function of temperature) of the measurements shown in Figures 5.47 and 5.48. For low temperatures the position of the FX emission line was used, as the D^0X emission band is not observable at elevated temperatures. Points show the data extracted from measurements, lines show fits with the Varshni Equation 5.2.

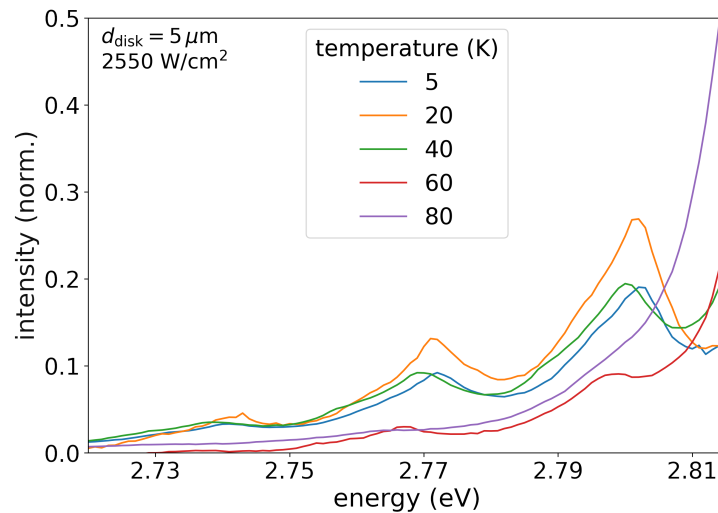


Figure 5.50: μ PL spectra of the side emission bands observed from a supported microdisk with a diameter of $5.0 \mu\text{m}$ at different temperatures between 5 and 80 K. The spectra were recorded with an excitation density of $2250 \frac{\text{W}}{\text{cm}^2}$.

observed with rising temperature.

This red-shift shows a connection of this emission to the bandgap and therefore makes a phonon replica effect more plausible compared to the multilayer interference effect mentioned earlier. The latter would not be dependent on temperature apart from the expansion of the material, which is too small to cause the shifts observed here. Additionally, the side bands seem to originate from some interaction between the material and the

excitons that cannot exist beyond 60 K.

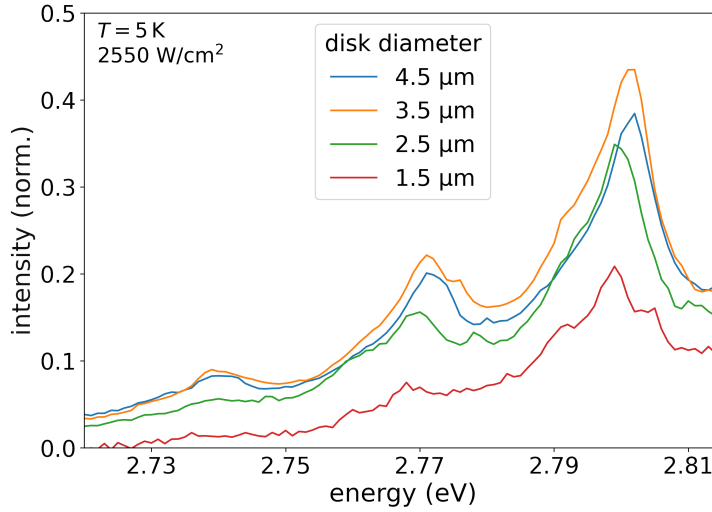


Figure 5.51: μ PL spectra of the side emission bands observed from supported microdisks with varying diameters at 5 K. The spectra were recorded with an excitation density of $2250 \frac{\text{W}}{\text{cm}^2}$.

In order to illustrate that the side bands are not connected to the disk size, they are analyzed for disks of different diameters in Figure 5.51. This plot includes the three most intense side bands for four different disk sizes, their position is similar for all diameters. The side band intensity is lower for smaller disks, because less material can be excited, which leads to a reduction of the overall emission intensity. This is especially pronounced for side bands at a lower energy, which generally show a lower intensity. Because of this, smaller disks might show fewer bands. A more detailed analysis of this can be seen in Figure 5.52, a plot of the spectral position of the side band as a function of the disk diameter for the four most intense side bands. The figure displays measurements from disks with diameters between 1.5 and 5.0 μm in steps of 0.25 μm .

The position of the side bands appears to be approximately constant for all analyzed disk diameters, showing that the occurrence of side bands is a material property not connected to the size of the microdisks or resonances that can form in them. Again, a spacing of the bands of approximately 30 meV (between 30.4 and 31.9 meV) can be observed, in agreement with the energy of the LO phonon of ZnSe at the Γ -point [126].

In conclusion, this section showed the formation of small modes on the low-energy side of the QW emission in the supported disks. This is comparable to the small resonances observed for free-standing microdisks with δ -type doping of the QW (sample B), as described in Section 5.2.1. The spectral position of these modes could be reproduced for

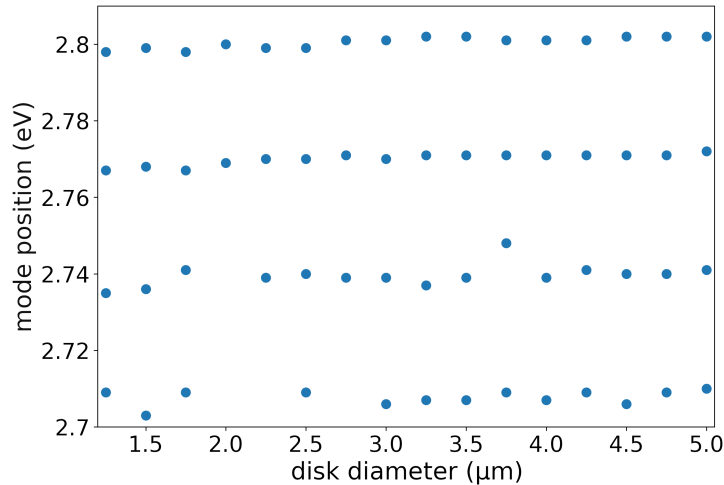


Figure 5.52: Overview of the spectral positions of the side emission bands observed from supported microdisks at 5 K under excitation with $2250 \frac{\text{W}}{\text{cm}^2}$. The positions are plotted as a function of the disk diameter.

measurements on different disks of the same diameter and was observed under both pulsed and cw excitation. The spectral position of these resonances is dependent on the disk size, which is an indication that these modes could be WGM resonances. The Q -factors of the modes were at least as high as those of comparable modes in free-standing disks, showing that resonances with low losses can form in supported microdisks.

In general, the material can be optically excited by pulsed as well as cw lasers. Cw operation requires a higher excitation density and leads to a stronger warming of the samples, which slightly reduces the obtained Q -factors.

Side emission bands were observed on the low-energy side of the QW emission in areas where the AIAs layer below the ZnSe-based material was oxidized to Al_2O_3 . The spectral position of these side bands is not dependent on disk size but changes along with the excitonic emission when T is varied. They are most likely phonon-replica based on the LO phonon of ZnSe.

The fact that resonances (likely WGMs) with low intensities can be observed on the low-energy side of the near-band-edge (NBE) emission, but no stimulated emission occurs, can be explained by reabsorption of photons propagating in the microdisk. As absorption is reduced at photon energies below the bandgap, this effect might not occur for the deep level emission (DLE) of the material, which might therefore exhibit modes with higher intensities. This will be analyzed in the following section, based on spectra of the complete emission spectrum of the supported microdisks.

5.3.3. Defect Emission Whispering Gallery Modes at Room Temperature

For the investigation of their DLE, the microdisks were analyzed at room temperature and ambient pressure using the setup described in Section 4.3. This allowed the recording and analysis of their whole emission spectrum.

Figure 5.53 shows spectra recorded when disks of different diameters were excited with an excitation density of $70 \frac{\text{W}}{\text{cm}^2}$.

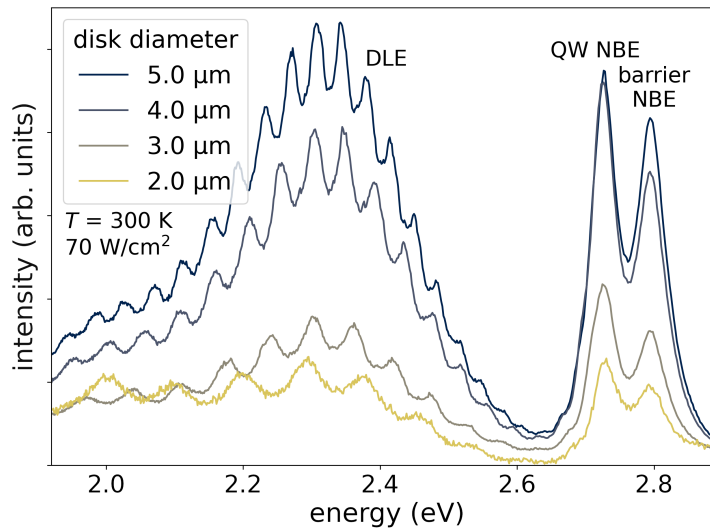


Figure 5.53: μ PL spectra observed from supported microdisks with varying diameters at room temperature. The spectra exhibit WGMs on the DLE which is further analyzed in Figure 5.56.

The emission observed from the disks consists of two maxima between 2.7 and 2.85 eV, which appear at the same spectral position for each disk size, and a broad emission band with a clear mode structure between 1.9 and 2.6 eV. For the latter, the mode spacing changes with the disk diameter, small disks show a larger mode spacing.

The NBE emission, consisting of QW and barrier emission, was already described in the temperature dependent spectra above (Figures 5.47 and 5.50). The broad emission band is the DLE of the ZnSe-based material, and is related to defects in the material forming states deep in the bandgap. Recombination across these states results in the emission of photons with a significantly reduced energy compared to the NBE emission (for a more detailed explanation see Section 2.1.2). The modes observed on the DLE are WGMs, similar to those reported on the defect emission of a ZnO disk in [128], this will be proven by a theoretical calculation below.

In Figure 5.54, the μ PL spectra of a supported microdisk with a diameter of $4.0 \mu\text{m}$ can be seen for different excitation densities. In order to show the strong influence of the

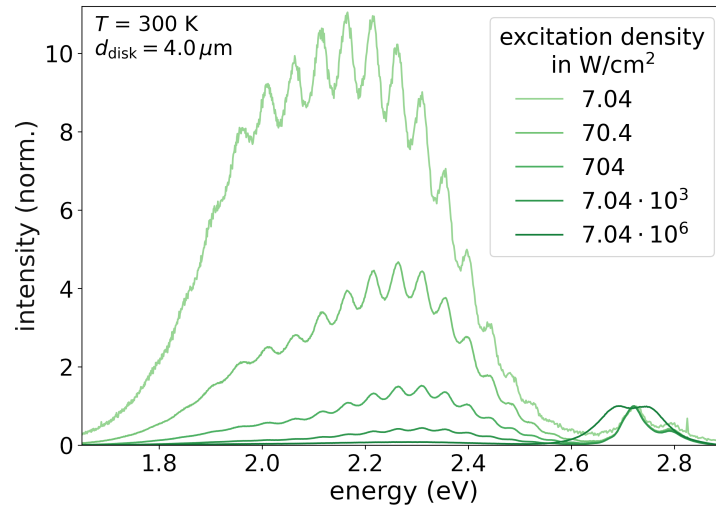


Figure 5.54: Series of μ PL spectra with rising excitation density of a supported microdisk with a diameter of $4.0 \mu\text{m}$ at room temperature. The spectra are normalized to the maximum of their NBE emission.

excitation density on the intensity of the DLE and especially the ratio of NBE emission intensity to DLE intensity, all spectra are normalized to the maximum intensity of the former.

The DLE is clearly more intense compared to the NBE emission for lower excitation densities. This is the case, because the emitting defects (Zn-vacancy related complexes [129]) have a very low density, but are very efficient at capturing charge carriers. Therefore, the transitions via these defects are bright at low excitation densities, when only a small number of charge carriers are excited in the system. However, a quick saturation of the intensity is observed if more carriers are excited that cannot all be trapped at defects. Compared to the measurements shown up to now, the excitation density needed to see intense DLE here ($< 100 \frac{\text{W}}{\text{cm}^2}$) is low, especially considering that excitation is in cw. The WGMs that can be observed on the DLE are more clearly visible for spectra with high relative DLE intensity, which is why an excitation density of $70 \frac{\text{W}}{\text{cm}^2}$ was used to further analyze the mode structure.

The WGMs forming on the DLE could be reproduced very well, this is evident in Figure 5.55, where spectra of 18 supported microdisks with the same diameter ($4.0 \mu\text{m}$) are analyzed. The spectral positions of the most intense mode and the three modes next to it on the lower-energy side are used for this analysis. These modes were chosen, because they were most clearly visible in the measurement, this is probably due to self-absorption in the high-energy part of the DLE. The measured mode positions are plotted as a function of the average mode position over all 18 measurements.

This leads to a spread of the results in a vertical line (blue dots in Figure 5.55). In addition

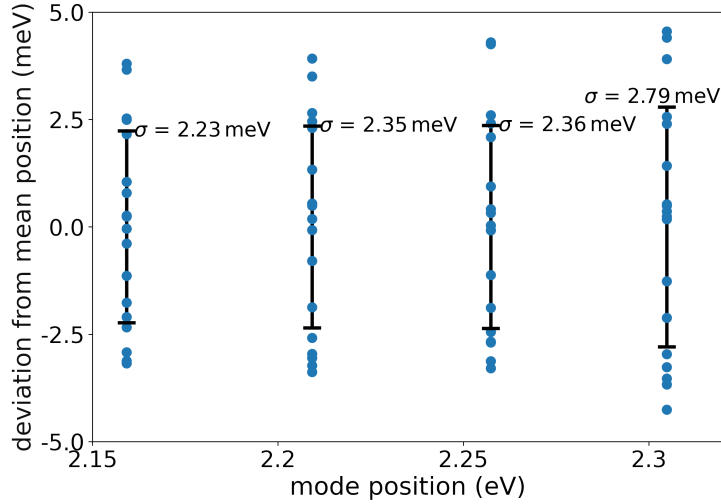


Figure 5.55: Variation of the spectral position of four modes observed from 18 different supported disks with a diameter of $4.0\ \mu\text{m}$. Data for each individual measurement is marked by blue dots. The standard deviation (error bar and annotation) is given to quantify the observed variation.

to that, the standard deviation of the positions is indicated (black error bar).

The standard deviation is between 2.23 and 2.79 meV for all modes. The mode spacing for this disk size is about 40 meV. This shows that the modes are well reproduced. Together with the fact that all 18 analyzed microdisks exhibited modes on the DLE, this proves that the fabrication process described in Section 4.1 yields highly reproducible resonators.

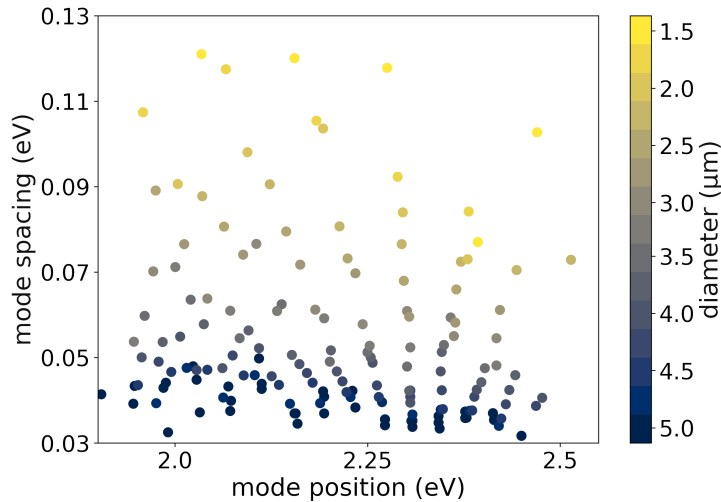


Figure 5.56: Spacing of WGMs observed from supported microdisks with diameters (color coded) between 1.5 and $5.0\ \mu\text{m}$ as a function of the spectral mode position.

Figure 5.56 presents the mode spacing observed in spectra of disks with different diameters (shown in Figure 5.53) as a function of the mode position. The resulting structure resembles

a hand-held fan, as the spacing is larger for smaller disks. At one position near 2.28 eV, a mode can be observed for many different disk sizes. These modes are not of the same order, but have different azimuthal mode numbers, as will be seen in the calculation of mode positions below.

This structure can be theoretically reproduced using a plane wave model commonly used to differentiate between WGMs and other resonances (e.g., Fabry-Pérot) in microdisks [128]: A group index n_g with a small dispersion n' is defined

$$n(\lambda) = n_g + n'\lambda. \quad (5.3)$$

The ansatz that the circumference of the disk, multiplied by the refractive index, must be equal to a multiple of the wavelength for a resonant mode is employed:

$$\pi d_{\text{disk}} \cdot n(\lambda_m) = m\lambda_m. \quad (5.4)$$

This assumes a radial quantum number of 1. The wavelength of a WGM with azimuthal quantum number m is then given by

$$\lambda_m = \frac{n_g \pi d_{\text{disk}}}{m - n' \pi d_{\text{disk}}}. \quad (5.5)$$

The λ_m calculated from Equation 5.5 with $n_g = 2.5$ and $n' = 10^{-4}$ and their spacing are shown in Figure 5.57. The values of the azimuthal quantum number m of the modes shown in this figure are between 21 and 90.

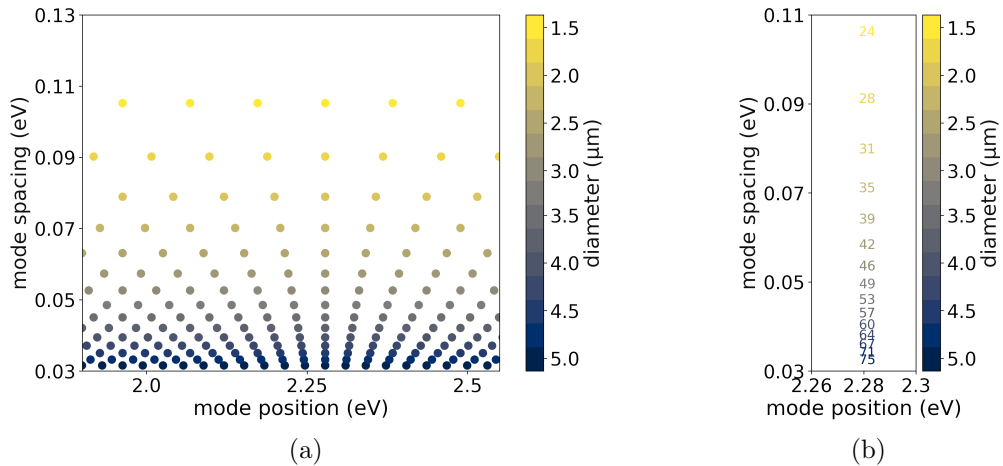


Figure 5.57: (a) Theoretical reproduction of the structure of the experimentally observed mode spacing for supported disks seen in Figure 5.56. (b) Excerpt from (a) showing the azimuthal mode numbers m of the WGMs appearing at the approximately same spectral position near 2.28 eV for all analyzed disk sizes.

The theoretical reproduction of Figure 5.56 in Figure 5.57a exhibits the same hand-held fan structure. The group index n_g and dispersion n' are fitting parameters, which will move the fan structure along the energy axis (additionally n' has a minor effect on the mode spacing as a function of energy). They can therefore be approximated from the position at which a mode appears at a fairly constant energy position for each disk size (in this case near 2.28 eV), which of course moves with the structure.

Figure 5.57b shows this ‘column’ of modes in more detail, as the dots marking a datapoint were replaced by annotations of the azimuthal quantum number m of the mode corresponding to this datapoint. From this it is obvious that it is not the same mode that appears at 2.28 eV for each disk size, the azimuthal quantum number m changes by 3 or 4 with each step of d_{disk} . This is an aliasing effect due to the ‘sampling’ of d_{disk} with a rate of $0.25 \mu\text{m}$, the size steps in which disks were fabricated.

The qualitative agreement between this simple theoretical model and the experimental results shows that the observed mode structure on the DLE of the microdisk emission is caused by WGM resonances.

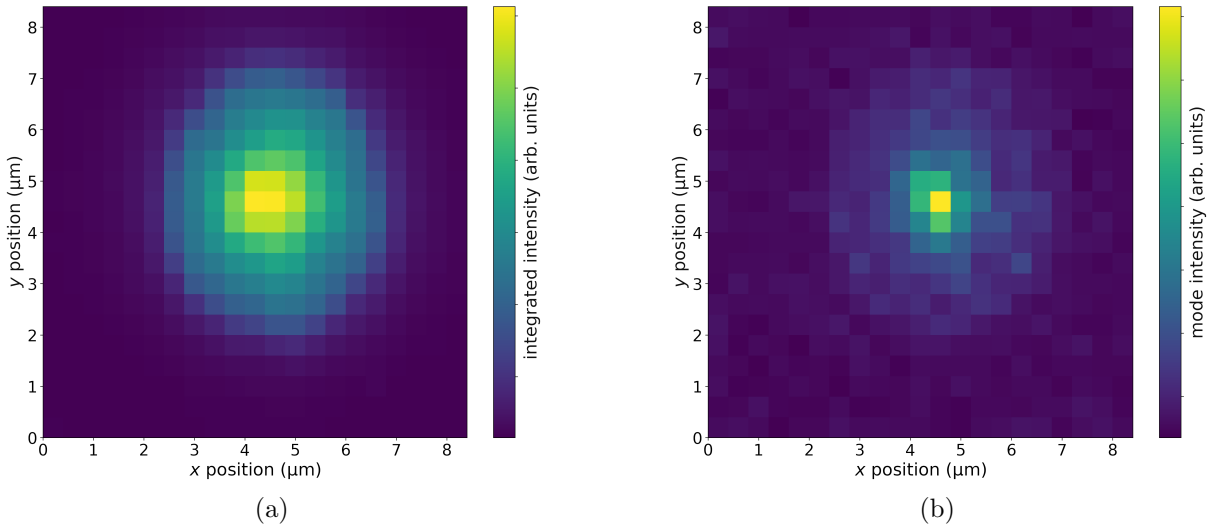


Figure 5.58: μPL map scans of a supported microdisk with a diameter of $4.0 \mu\text{m}$ measured at room temperature. Intensities are plotted as a function of the excitation position. (a) Map of the total integrated μPL intensity. (b) Map of the intensity of the WGMs observed on the DLE.

A map scan (i.e., a series of μPL spectra taken with varying excitation position) of a supported microdisk with a diameter of $4.0 \mu\text{m}$ was performed in order to see where the WGMs can be excited. As they travel around the border of the disk, excitation in these places might be favorable for mode formation. The results of the map scan measurement are presented in Figure 5.58.

Figure 5.58a displays the μ PL intensity (color coded) as a function of the excitation spot. The intensity is high in the center of the disk and drops uniformly in all directions. A similar behavior was already observed from the line scan of a marker at cryogenic temperatures (compare Figure 5.31). The largest amount of material can be excited in the middle of the disk, this drops uniformly in all directions, as the disk is round and the emission intensity is directly proportional to the amount of material being excited.

Figure 5.58b shows the intensity of the WGMs (color coded) as a function of the excitation spot. The WGM intensity was calculated as the ratio of the intensity of the most intense DLE mode observed to the minimum of intensity in the neighboring dip. This yields a measure of how well modes can be observed against the DLE background in the spectra. The mode intensity is highest where total intensity is highest and exhibits the same uniform drop of intensity.

This correlation of the total and mode intensity can be observed, because the modes can only form if there is sufficient emission. At least at the low excitation densities/-light intensities used in this experiment, this is only given if the center of the disk is excited.

In conclusion, the room temperature DLE of supported microdisks exhibits a broad mode spectrum, these modes are confirmed to be WGMs by a simple model. The spectral positions of the WGMs are highly reproducible, highlighting the consistency of the fabrication process described in Section 4.1. The intensity of the DLE is strongly dependent on the excitation density, experiments and applications based on the mode structure found on this emission band can therefore only be realized in the low excitation regime. Because of this, lasing is not possible on the DLE due to the low relative gain at higher excitation. The WGM intensity is found to be highest when the total intensity emitted from the disk is highest, i.e., if the center of the microdisk is excited.

5.3.4. Deformation of the Resonators

For sample A, it was already seen in Section 5.1.3 that the deformation of the resonators has an impact on their optical quality. For the analysis of supported microdisks, their deformation functions were extracted from SEM images as described in Section 4.2.2. As shown there, the extraction process is different for supported disks compared to their free-standing counterparts. The calculated roughness Δr is expected to be smaller, since only a single row of pixels is used for the calculation of this standard deviation of the disk edge from an ideal circle.

Figure 5.59 shows the relative deviation of the disks from their ideal radii for supported disks (sample C, blue points) and the free-standing disks (sample A, orange points), whose

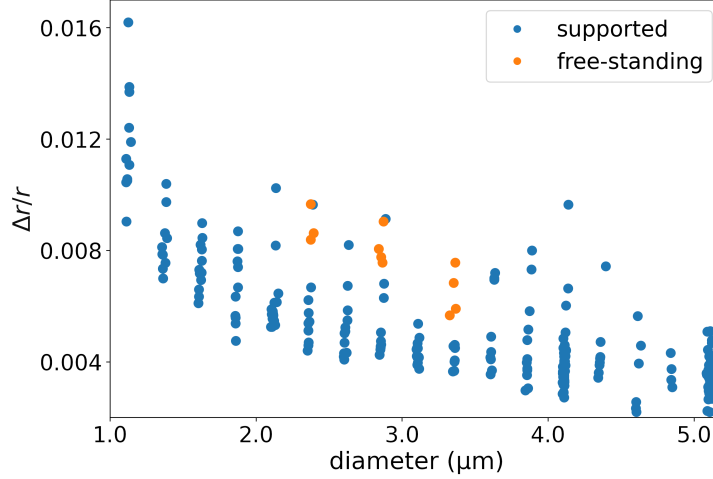


Figure 5.59: Relative deviation of the disk edge from the ideal radius for free-standing (sample A) and supported (sample C) microdisks as a function of their average diameter.

data is shown in Figure 5.11, being added for comparison. It can be noted that a large number of supported disks was analyzed with diameters between 1.0 and 5.0 μm . These disks can be fabricated in close proximity to other resonators, as they do not need to be underetched. This leads to an increase of the number of disks per unit of sample space. Many resonators can therefore be fabricated and analyzed.

A larger $\frac{\Delta r}{\bar{r}}$ is observed for disks with smaller diameters. The supported disks show a lower relative deviation from the ideal radius than free-standing disks of comparable diameters, the difference is close to a factor of 2. A comparison of the values found for $\frac{\Delta r}{\bar{r}}$ for supported and free-standing disks is nontrivial, due to the differences in the extraction techniques discussed in Section 4.2.2. However, the Q -factors observed from the small modes on the low energy side of the NBE emission were comparable for supported and free-standing disks. Given that a reduction of Q is expected for supported disks due to leakage into the substrate, a better structural quality of the supported disks appears likely. The increase of $\frac{\Delta r}{\bar{r}}$ for small \bar{r} could be caused by a finite fabrication accuracy, as was seen for free-standing disks in Section 5.1.3. For an analysis of this, Figure 5.60 shows the absolute values for Δr as a function of d_{disk} for all datapoints (supported and free-standing microdisks) seen in Figure 5.59.

The absolute values for Δr show a very small increase with the disk diameter, the values found for $d_{\text{disk}} = 1.0 \mu\text{m}$ scatter around 6 nm and the average Δr of disks with a diameter of 5.0 μm is about 9 nm. This was not observed for free-standing disks, but from the data plotted in Figure 5.60 it seems plausible that this could be due to the low number of disks and radii analyzed.

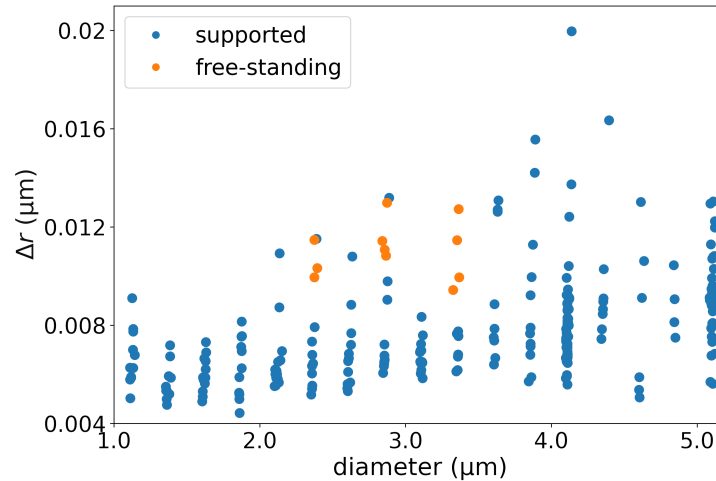


Figure 5.60: Absolute deviation of the disk edge from the ideal radius for free-standing (sample A) and supported (sample C) microdisks as a function of their average diameter.

The e-beam lithography process defining the supported microdisks seems to yield a high structural quality. The slight increase of Δr with a rise in d_{disk} might be explained by a larger area of the mask material being inadvertently illuminated, as the illumination of a larger disk area needs more time. An advantage of the supported disks over their free-standing counterparts might be that they cannot bend out of plane, as observed for the latter [63], reducing the optical quality of the free-standing resonators and increasing the Δr extracted from top-view SEM images.

In conclusion, supported microdisk resonators exhibit a high structural quality, as was expected because of the high Q -factors that were observed in Section 5.3.2. The meaningfulness of a comparison of the values for Δr presented here to the free-standing disks is limited due to the different extraction methods. However, in conjunction with the comparison of Q -factors between the disk types, a higher structural quality of the supported disks can be assumed.

6. Conclusion and Outlook

In the first part of ‘Results and Discussion’, Section 5.1, free-standing microdisks with a $\text{Zn}_{0.79}\text{Cd}_{0.21}\text{Se}$ QW doped with fluorine embedded in $\text{Zn}_{0.84}\text{Mg}_{0.16}\text{Se}$ barriers were discussed. Strong WGMs were observed from disks of different sizes (between $2.8\ \mu\text{m}$ and $3.8\ \mu\text{m}$ in diameter), the analysis of their intensity as a function of excitation density showed that the intensity of these modes was enhanced by stimulated emission. However, lasing could not be observed from these disks, since a degradation of the mode intensity was observed at excitation densities above the threshold. This degradation is marked by an increase of the FWHM of the mode (lowering the Q -factor) and accompanied by a blue-shift of its spectral position, which is likely caused by a change in refractive index.

Modes observed in the emission of disks with different diameters allowed for a comparison of their spacing with a variation in disk size. From this, no clear trend was observed, because the WGM spectra are non trivial, as the modes show different radial quantum numbers. This is known from the results of a theoretical calculation of the WGM resonances in the disks based on the boundary element method which used the deformation function $r(\varphi)$, that was extracted from SEM images for each analyzed disk, as an input parameter. This calculations were performed by Jan Wiersig at the Universität Magdeburg and mark the first time that such simulations were performed based on the complete deformation data of actual resonators that could be analyzed experimentally and not based on statistical information on their roughness or numerical models which were deformed by a random variable. Both the spectral mode position and the observed Q -factors were in good agreement between experiment and theory. A FDTD simulation of ideal circular disks yielded similar results for the spectral position and field distribution of the modes and therefore shows that the influence of edge roughness on the modes that form and propagate in the resonators is low.

However, an influence on the optical quality can be seen from a correlation between the experimentally observed Q -factors and the relative deviation of the microdisks extracted from SEM images that showed smaller Q for disks with higher values of $\frac{\Delta r}{r}$. The process of obtaining this deformation data was developed in this work and is extensively described in Section 4.2.2. The analysis of the data shows that the absolute roughness of the resonators does not change in the range of radii analyzed for free-standing disks in this work, the roughness of the microdisks is therefore limited by the accuracy of their production process.

In Section 5.2, results obtained from free-standing microdisks with a $\text{Zn}_{0.85}\text{Cd}_{0.15}\text{Se}:\text{F}$ QW (δ -doped with fluorine) embedded in $\text{Zn}_{0.82}\text{Mg}_{0.18}\text{Se}$ barriers are presented. Small modes were observed on the low-energy side of the emission at low temperatures and low

excitation densities, however, the gain of the material was not sufficient at these spectral positions to support stimulated emission. A scan of the excitation spot over the disk revealed that the excited modes change as a function of the position at which the disk is excited, as the modes correspond to different field distributions in the microdisk. Since some modes occur at a large range of excitation positions, it can be concluded that they are not the result of the emission of a single halogen impurity but rather resonances of the microdisk.

At higher excitation densities, the resonators exhibited modes growing by stimulated emission, comparable to those described above. The aforementioned degradation and FWHM increase were strong in these disks, they are accompanied by a smaller blue-shift of the emission. This leads to the conclusion that the degradation is due to a change of the halogen impurities to nonradiative recombination centers at points that show a high field intensity when the modes propagate in the disk. The blue-shift is reduced due to the lower concentration of free charge carriers in structures with a low dopant concentration. A measurement of modes enhanced by stimulated emission at varying temperatures shows that the resonances red-shift with rising temperatures, proving that heating of the structure is not the cause of the blue-shift or degradation.

In the third section of the discussion of the results (5.3), microdisks in the novel supported geometry are introduced, based on experimental results obtained from microdisks with a ZnSe:Cl QW (δ -doped with chlorine) embedded in $\text{Zn}_{0.91}\text{Mg}_{0.09}\text{Se}$ barriers. Similar to those observed from the δ -doped free-standing microdisks in Section 5.2, small modes can be found on the low-energy side of the QW emission for microdisks. The Q -factors of the modes are comparable for both structures, despite the fact that the supported geometry will result in leakage of the mode into the substrate. The position of these modes could be reproduced in measurements of two different disks with the same nominal size. They are not influenced by degradation and stable under continuous excitation. A comparison of μPL measurements under excitation with pulsed and cw laser sources provides similar results with slightly lower Q -factors of the modes under cw excitation. This shows that supported microdisks can be used in applications with cw excitation.

Side bands of the QW emission were found for ZnSe-based material on the Al_2O_3 , these are likely phonon replica caused by the LO phonon of ZnSe, as this fits the spacing of those bands. Additionally, their spectral position is independent of disk size and shifts with the excitonic emission lines for rising temperatures.

A characterization of the defect emission band of the supported microdisks at room temperature reveals a large number of WGMs which too could be well reproduced in measurements of different disks with the same nominal size. Their mode spacing can

be theoretically reproduced with a simple model assuming a radial quantum number of 1; this shows that the mode spectrum is less complex than the ones observed on the QW emission for free-standing disks. The intensity of the defect emission was found to be strongly dependent on the excitation density, it saturates at low excitation densities, since the number of defects in the QW is limited. Because of this limitation of gain, the modes on the DLE cannot show stimulated emission or lasing. A μ PL map scan showed that the modes were most prominent in the spectrum when the overall intensity of the defect emission was high, the resonances of the microdisks require a sufficient background intensity to become visible. The deformation of these resonators was extracted from SEM images, as for the free-standing disks in Section 5.1. As described in Section 4.2.2, the process that was developed for supported disks in order to extract their deformation functions $r(\varphi)$ is slightly different from the process for free-standing disks. Because of this, a comparison of the results obtained for the different disk types is nontrivial. It was found that the relative deviation $\frac{\Delta r}{r}$ is lower for supported disks by about a factor of 2. Despite the unclear comparability of the two values, the similar optical quality, regardless of the leakage into the substrate mentioned above, makes a better structural quality of the supported disks seem reasonable. Notably, the edge roughness Δr was found to rise slightly with the disk diameter for the supported disks.

The first introduction of ZnSe-based microdisks in the supported geometry in this work looks promising, as their optical quality appears to be comparable to that of free-standing disks, and it was shown that the resonators support the formation of WGMs. In future experiments, the effect of the oxidation on the microdisks needs to be better understood, as it could lead to nonradiative recombination as seen in the analysis of markers in Section 5.3.3. Raman scattering measurements can provide an insight into the strain of the ZnSe-based material at different positions and could be used to see changes of the lattice constant between the AlAs and Al₂O₃ regions. Furthermore, it could be analyzed if the strain in the microdisk is uniform at all positions due to the homogeneous underlayer or if the underoxidation causes a strain gradient in radial direction.

In order to quantify the increase of the thermal contact of the microdisk to the substrate in the supported geometry, a two laser Raman thermometry study of both free-standing and supported microdisks could be used. In this experiment, a Raman signal of the structure is recorded as a function of position while a heating laser is focused on the structure. The shift of the Raman lines shows the local lattice temperature and can therefore be used to quantify how much heat is accumulated in the microdisk at a given excitation. Such experiments would enable a comparison between the free-standing and supported microdisks analyzed in this work without requiring further processing steps. If

the supported microdisks still exhibit thermal problems, a thin layer of ZnSe (similar to the ‘wetting layer’ found for Stranski-Krastanov grown quantum dots) connecting them might lead to a significant increase of thermal dissipation while not reducing resonator quality [97]. Additionally, an analysis of oxidized and non-oxidized parts of the material could lead to further insights into the structure after the oxidation process.

Lasing can be expected from ZnSe-based microdisks in supported geometries if self- and reabsorption in the structure are reduced [65]. This is why lasing or stimulated emission near the band edge emission could likely be observed from a microdisk processed from a ZnCdSe QW embedded in ZnMgSe barriers, as the bandgap difference between the two materials is higher. This would also increase the comparability of the measurements on supported microdisks to the results obtained from free-standing disks in this work. An additional improvement of the emission properties might be achieved if the top ZnMgSe barrier is slightly thicker than the bottom barrier. This would place the QW in the middle of the ZnSe-based structure, taking the ZnSe buffer layer into account, resulting in a stronger overlap between the field of the resonating mode and the emitting region. In future experiments analyzing lasing from supported microdisks, the reduced edge roughness of these disks might play an important role, as a strong correlation between the sidewall roughness and lasing threshold of microdisks has been reported recently [41].

A. References

- [1] T. Yasuda, I. Mitsuishi, and H. Kukimoto. Metalorganic vapor phase epitaxy of low-resistivity p-type ZnSe. *Applied Physics Letters*, 52(1):57–59, jan 1988.
- [2] M. A. Haase, J. Qiu, J. M. DePuydt, and H. Cheng. Blue-green laser diodes. *Applied Physics Letters*, 59(11):1272–1274, sep 1991.
- [3] S. Guha, J. M. DePuydt, M. A. Haase, J. Qiu, and H. Cheng. Degradation of II-VI based blue-green light emitters. *Applied Physics Letters*, 63(23):3107–3109, dec 1993.
- [4] Nobel Lectures in Physics. New light illuminating the world. *UFN*, 186(5):503–503, 2014.
- [5] C. Weisbuch, M. Nishioka, A. Ishikawa, and Y. Arakawa. Observation of the coupled exciton-photon mode splitting in a semiconductor quantum microcavity. *Physical Review Letters*, 69(23):3314–3317, dec 1992.
- [6] Charles H. Bennett and Gilles Brassard. Quantum cryptography: Public key distribution and coin tossing. *Theoretical Computer Science*, 560:7–11, dec 2014.
- [7] J. I. Cirac, P. Zoller, H. J. Kimble, and H. Mabuchi. Quantum state transfer and entanglement distribution among distant nodes in a quantum network. *Physical Review Letters*, 78(16):3221–3224, apr 1997.
- [8] Johannes Renner, Lukas Worschech, Alfred Forchel, Suddhasatta Mahapatra, and Karl Brunner. Glass supported ZnSe microring strongly coupled to a single CdSe quantum dot. *Applied Physics Letters*, 93(15):151109, oct 2008.
- [9] E. M. Purcell, H. C. Torrey, and R. V. Pound. Resonance absorption by nuclear magnetic moments in a solid. *Physical Review*, 69(1-2):37–38, jan 1946.
- [10] S. Mariani, A. Andronico, A. Lemaître, I. Favero, S. Ducci, and G. Leo. Second-harmonic generation in AlGaAs microdisks in the telecom range. *Optics Letters*, 39(10):3062, may 2014.
- [11] Rui Luo, Haowei Jiang, Steven Rogers, Hanxiao Liang, Yang He, and Qiang Lin. On-chip second-harmonic generation and broadband parametric down-conversion in a lithium niobate microresonator. *Optics Express*, 25(20):24531, sep 2017.
- [12] K. Sebald, C. Kruse, and J. Wiersig. Properties and prospects of blue-green emitting II-VI-based monolithic microcavities. *physica status solidi (b)*, 246(2):255–271, feb 2009.

- [13] S. Enoch, J.-J. Simon, L. Escoubas, Z. Elalmy, F. Lemarquis, P. Torchio, and G. Albrand. Simple layer-by-layer photonic crystal for the control of thermal emission. *Applied Physics Letters*, 86(26):261101, jun 2005.
- [14] A. Pawlis, M. Panfilova, D. J. As, K. Lischka, K. Sanaka, T. D. Ladd, and Y. Yamamoto. Lasing of donor-bound excitons in ZnSe microdisks. *Physical Review B*, 77(15), apr 2008.
- [15] S. Strauf, P. Michler, M. Klude, D. Hommel, G. Bacher, and A. Forchel. Quantum optical studies on individual acceptor bound excitons in a semiconductor. *Physical Review Letters*, 89(17), oct 2002.
- [16] Darin J. Sleiter, Kaoru Sanaka, Y. M. Kim, Klaus Lischka, Alexander Pawlis, and Yoshihisa Yamamoto. Optical pumping of a single electron spin bound to a fluorine donor in a ZnSe nanostructure. *Nano Letters*, 13(1):116–120, dec 2012.
- [17] Matthew Borselli, Kartik Srinivasan, Paul E. Barclay, and Oskar Painter. Rayleigh scattering, mode coupling, and optical loss in silicon microdisks. *Applied Physics Letters*, 85(17):3693–3695, oct 2004.
- [18] Matthew Borselli, Thomas J. Johnson, and Oskar Painter. Beyond the rayleigh scattering limit in high-q silicon microdisks: theory and experiment. *Optics Express*, 13(5):1515, 2005.
- [19] Mohammad Soltani, Siva Yegnanarayanan, and Ali Adibi. Ultra-high Q planar silicon microdisk resonators for chip-scale silicon photonics. *Optics Express*, 15(8):4694, 2007.
- [20] M.P. Kulakov and I.V. Balyakina. Solid state wurtzite-sphalerite transformation and phase boundaries in ZnSe-CdSe. *Journal of Crystal Growth*, 113(3-4):653–658, sep 1991.
- [21] B. Vögele, C. Morhain, B. Urbaszek, S.A. Telfer, K.A. Prior, and B.C. Cavenett. The influence of magnesium on p-type doping and optoelectronic properties of $\text{Zn}_{1-x}\text{Mg}_x\text{Se}$ -based heterostructures. *Journal of Crystal Growth*, 201-202:950–953, may 1999.
- [22] Nobuo Matsumura, Jun Ueda, and Junji Saraie. Molecular beam epitaxial growth of hexagonal CdSe and ZnCdSe on cubic GaAs(111)b substrates. *Japanese Journal of Applied Physics*, 39(Part 2, No. 10B):L1026–L1028, oct 2000.
- [23] L. Vegard. Die Konstitution der Mischkristalle und die Raumfüllung der Atome. *Zeitschrift für Physik*, 5(1):17–26, jan 1921.

-
- [24] S. Tan, A. Ghazali, and J.C.S. Lévy. Simulated growth of layers on a substrate with mismatch: structural studies. *Surface Science*, 369(1-3):360–366, dec 1996.
- [25] C. Kruse, S. M. Ulrich, G. Alexe, E. Roventa, R. Kröger, B. Brendemühl, P. Michler, J. Gutowski, and D. Hommel. Green monolithic II–VI vertical-cavity surface-emitting laser operating at room temperature. *physica status solidi (b)*, 241(3):731–738, mar 2004.
- [26] B. Jobst, D. Hommel, U. Lunz, T. Gerhard, and G. Landwehr. E_0 band-gap energy and lattice constant of ternary $\text{Zn}_{1-x}\text{Mg}_x\text{Se}$ as functions of composition. *Applied Physics Letters*, 69(1):97–99, jul 1996.
- [27] U. Lunz, J. Kuhn, F. Goschenhofer, U. Schüssler, S. Einfeldt, C. R. Becker, and G. Landwehr. Temperature dependence of the energy gap of zinc-blende CdSe and $\text{Cd}_{(1-x)}\text{Zn}_x\text{Se}$ epitaxial layers. *Journal of Applied Physics*, 80(12):6861–6863, dec 1996.
- [28] M. Schulz O. Madelung, U. Rössler. Zinc selenide (ZnSe) exciton energies. In *Landolt-Börnstein - Group III Condensed Matter 41B (II-VI and I-VII Compounds; Semimagnetic Compounds)*, pages 1–7. Springer-Verlag, 1999.
- [29] Y.P. Varshni. Temperature dependence of the energy gap in semiconductors. *Physica*, 34(1):149–154, jan 1967.
- [30] L. Esaki and R. Tsu. Superlattice and negative differential conductivity in semiconductors. *IBM Journal of Research and Development*, 14(1):61–65, jan 1970.
- [31] Andrea Sacchetti. Electrical current in nanoelectronic devices. *Physics Letters A*, 374(39):4057–4060, aug 2010.
- [32] A. Finke, M. Ruth, S. Scholz, A. Ludwig, A. D. Wieck, D. Reuter, and A. Pawlis. Extending the spectral range of CdSe/ZnSe quantum wells by strain engineering. *Physical Review B*, 91(3), jan 2015.
- [33] Lord Rayleigh. CXII. The problem of the whispering gallery. *The London, Edinburgh, and Dublin Philosophical Magazine and Journal of Science*, 20(120):1001–1004, dec 1910.
- [34] C. V. Raman and G. A. Sutherland. Whispering-Gallery Phenomena at St. Paul’s Cathedral. *Nature*, 108(2706):42–42, sep 1921.
- [35] C. G. B. Garrett, W. Kaiser, and W. L. Bond. Stimulated emission into optical whispering modes of spheres. *Physical Review*, 124(6):1807–1809, dec 1961.
-

- [36] S. L. McCall, A. F. J. Levi, R. E. Slusher, S. J. Pearton, and R. A. Logan. Whispering-gallery mode microdisk lasers. *Applied Physics Letters*, 60(3):289–291, jan 1992.
- [37] T. Krauss, P.J.R. Laybourn, and J. Roberts. CW operation of semiconductor ring lasers. *Electronics Letters*, 26(25):2095, 1990.
- [38] V. Zwiller, S. Fälth, J. Persson, W. Seifert, L. Samuelson, and G. Björk. Fabrication and time-resolved studies of visible microdisk lasers. *Journal of Applied Physics*, 93(4):2307–2309, feb 2003.
- [39] A. M. Mintairov, Y. Chu, Y. He, S. Blokhin, A. Nadochy, M. Maximov, V. Tokranov, S. Oktyabrsky, and J. L. Merz. High-spatial-resolution near-field photoluminescence and imaging of whispering-gallery modes in semiconductor microdisks with embedded quantum dots. *Physical Review B*, 77(19), may 2008.
- [40] Yiyun Zhang, Xuhui Zhang, Kwai Hei Li, Yuk Fai Cheung, Cong Feng, and Hoi Wai Choi. Advances in III-nitride semiconductor microdisk lasers. *physica status solidi (a)*, 212(5):960–973, mar 2015.
- [41] Chunyu Zhao, Chak Wah Tang, Jiannong Wang, and Kei May Lau. Ultra-low threshold green InGaN quantum dot microdisk lasers grown on silicon. *Applied Physics Letters*, 117(3):031104, jul 2020.
- [42] Jan Wiersig and Julius Kullig. Optical microdisk cavities with rough sidewalls: A perturbative approach based on weak boundary deformations. *Physical Review A*, 95(5):053815, may 2017.
- [43] Ardavan F. Oskooi, David Roundy, Mihai Ibanescu, Peter Bermel, J.D. Joannopoulos, and Steven G. Johnson. Meep: A flexible free-software package for electromagnetic simulations by the FDTD method. *Computer Physics Communications*, 181(3):687–702, mar 2010.
- [44] Kane Yee. Numerical solution of initial boundary value problems involving Maxwell’s equations in isotropic media. *IEEE Transactions on Antennas and Propagation*, 14(3):302–307, may 1966.
- [45] Jan Wiersig. Boundary element method for resonances in dielectric microcavities. *Journal of Optics A: Pure and Applied Optics*, 5(1):53–60, dec 2002.
- [46] P. A. Knipp and T. L. Reinecke. Boundary-element method for the calculation of electronic states in semiconductor nanostructures. *Physical Review B*, 54(3):1880–1891, jul 1996.
- [47] Alexander I. Nosich, Elena I. Smotrova, Svetlana V. Boriskina, Trevor M. Benson,

- and Phillip Sewell. Trends in microdisk laser research and linear optical modelling. *Optical and Quantum Electronics*, 39(15):1253–1272, dec 2007.
- [48] Donald R. Wilton. Review of current status and trends in the use of integral equations in computational electromagnetics. *Electromagnetics*, 12(3-4):287–341, jul 1992.
- [49] R. M. Park, M. B. Troffer, C. M. Rouleau, J. M. DePuydt, and M. A. Haase. p-type ZnSe by nitrogen atom beam doping during molecular beam epitaxial growth. *Applied Physics Letters*, 57(20):2127–2129, nov 1990.
- [50] Isamu Akasaki, Hiroshi Amano, Masahiro Kito, and Kazumasa Hiramatsu. Photoluminescence of Mg-doped p-type GaN and electroluminescence of GaN p-n junction LED. *Journal of Luminescence*, 48-49:666–670, jan 1991.
- [51] G. C. Hua, N. Otsuka, D. C. Grillo, Y. Fan, J. Han, M. D. Ringle, R. L. Gunshor, M. Hovinen, and A. V. Nurmikko. Microstructure study of a degraded pseudomorphic separate confinement heterostructure blue-green laser diode. *Applied Physics Letters*, 65(11):1331–1333, sep 1994.
- [52] M. Hovinen, J. Ding, A. Salokatve, A. V. Nurmikko, G. C. Hua, D. C. Grillo, Li He, J. Han, M. Ringle, and R. L. Gunshor. On degradation of ZnSe-based blue-green diode lasers. *Journal of Applied Physics*, 77(8):4150–4152, apr 1995.
- [53] Y.M. Kim, D. Sleiter, K. Sanaka, D. Reuter, K. Lischka, Y. Yamamoto, and A. Pawlis. Optically controlled initialization and read-out of an electron spin bound to a fluorine donor in ZnSe. *Current Applied Physics*, 14(9):1234–1239, sep 2014.
- [54] Kaoru Sanaka, Alexander Pawlis, Thaddeus D. Ladd, Klaus Lischka, and Yoshihisa Yamamoto. Indistinguishable photons from independent semiconductor nanostructures. *Physical Review Letters*, 103(5):053601, jul 2009.
- [55] Kaoru Sanaka, Alexander Pawlis, Thaddeus D. Ladd, Darin J. Sleiter, Klaus Lischka, and Yoshihisa Yamamoto. Entangling single photons from independently tuned semiconductor nanoemitters. *Nano Letters*, 12(9):4611–4616, aug 2012.
- [56] F. Heisterkamp, E. A. Zhukov, A. Greilich, D. R. Yakovlev, V. L. Korenev, A. Pawlis, and M. Bayer. Longitudinal and transverse spin dynamics of donor-bound electrons in fluorine-doped ZnSe: Spin inertia versus Hanle effect. *Physical Review B*, 91(23):235432, jun 2015.
- [57] M. Hovinen, J. Ding, A. V. Nurmikko, D. C. Grillo, J. Han, L. He, and R. L. Gunshor.

- Blue-green laser emission from ZnSe quantum well microresonators. *Applied Physics Letters*, 63(23):3128–3130, dec 1993.
- [58] A. Pawlis, M. Panfilova, K. Sanaka, T.D. Ladd, D.J. As, K. Lischka, and Y. Yamamoto. Low-threshold ZnSe microdisk laser based on fluorine impurity bound-exciton transitions. *Microelectronics Journal*, 40(2):256–258, feb 2009.
- [59] M. Panfilova, A. Pawlis, C. Arens, S. Michaelis de Vasconcellos, G. Berth, K.P. Hüsck, V. Wiedemeier, A. Zrenner, and K. Lischka. Micro-raman imaging and micro-photoluminescence measurements of strain in ZnMgSe/ZnSe microdiscs. *Microelectronics Journal*, 40(2):221–223, feb 2009.
- [60] Marina Panfilova, Alexander Pawlis, Alexey Shchekin, Sergey Lemeshko, and Klaus Lischka. Investigations of strain in ZnMgSe/ZnSe microdisks by means of the micro-raman imaging. *physica status solidi (c)*, 7(6):1675–1677, mar 2010.
- [61] M. Ruth, A. Finke, G. Schmidt, D. Reuter, S. Scholz, A. Ludwig, A. D. Wieck, and A. Pawlis. Optical properties of strain-compensated CdSe/ZnSe/(Zn,Mg)Se quantum well microdisks. *Optics Express*, 23(22):29079, oct 2015.
- [62] G. Schmidt, T. Rieger, S. Trellenkamp, D. Grützmacher, and A. Pawlis. Photon guiding characteristics of waveguide membranes coupled to a microdisk of ZnSe/(Zn,Mg)Se quantum well structures. *Semiconductor Science and Technology*, 32(7):075015, jun 2017.
- [63] J. Renner, L. Worschech, A. Forchel, S. Mahapatra, and K. Brunner. Whispering gallery modes in high quality ZnSe/ZnMgSSe microdisks with CdSe quantum dots studied at room temperature. *Applied Physics Letters*, 89(9):091105, aug 2006.
- [64] Johannes Renner, Lukas Worschech, Suddhasatta Mahapatra, Karl Brunner, and Alfred Forchel. Optical characterization of ZnSe/ZnMgSSe microdisks with embedded CdSe quantum dots. *physica status solidi (c)*, 4(9):3289–3296, sep 2007.
- [65] Johannes Renner, Lukas Worschech, Alfred Forchel, Suddhasatta Mahapatra, and Karl Brunner. CdSe quantum dot microdisk laser. *Applied Physics Letters*, 89(23):231104, dec 2006.
- [66] Chun Hao Lin, Qingji Zeng, Evan Lafalce, Marcus J. Smith, Sidney T. Malak, Jaehan Jung, Young Jun Yoon, Zhiqun Lin, Zeev Valy Vardeny, and Vladimir V. Tsukruk. Large-scale robust quantum dot microdisk lasers with controlled high quality cavity modes. *Advanced Optical Materials*, 5(9):1700011, mar 2017.
- [67] E. D. Haberer, R. Sharma, C. Meier, A. R. Stonas, S. Nakamura, S. P. DenBaars, and

- E. L. Hu. Free-standing, optically pumped, GaN/InGaN microdisk lasers fabricated by photoelectrochemical etching. *Applied Physics Letters*, 85(22):5179–5181, nov 2004.
- [68] R. A. Mair, K. C. Zeng, J. Y. Lin, H. X. Jiang, B. Zhang, L. Dai, A. Botchkarev, W. Kim, H. Morkoç, and M. A. Khan. Optical modes within III-nitride multiple quantum well microdisk cavities. *Applied Physics Letters*, 72(13):1530–1532, mar 1998.
- [69] Adele C. Tamboli, Elaine D. Haberer, Rajat Sharma, Kwan H. Lee, Shuji Nakamura, and Evelyn L. Hu. Room-temperature continuous-wave lasing in GaN/InGaN microdisks. *nature photonics*, 1(1):61–64, dec 2006.
- [70] H. W. Choi, K. N. Hui, P. T. Lai, P. Chen, X. H. Zhang, S. Tripathy, J. H. Teng, and S. J. Chua. Lasing in GaN microdisks pivoted on Si. *Applied Physics Letters*, 89(21):211101, nov 2006.
- [71] Yiyun Zhang, Zetao Ma, Xuhui Zhang, T. Wang, and H. W. Choi. Optically pumped whispering-gallery mode lasing from 2- μm GaN micro-disks pivoted on Si. *Applied Physics Letters*, 104(22):221106, jun 2014.
- [72] M. Athanasiou, R. Smith, B. Liu, and T. Wang. Room temperature continuous-wave green lasing from an InGaN microdisk on silicon. *Scientific Reports*, 4(1), nov 2014.
- [73] Igor Aharonovich, Alexander Woolf, Kasey J. Russell, Tongtong Zhu, Nan Niu, Menno J. Kappers, Rachel A. Oliver, and Evelyn L. Hu. Low threshold, room-temperature microdisk lasers in the blue spectral range. *Applied Physics Letters*, 103(2):021112, jul 2013.
- [74] M. Mexis, S. Sergent, T. Guillet, C. Brimont, T. Bretagnon, B. Gil, F. Semond, M. Leroux, D. Néel, S. David, X. Chécoury, and P. Boucaud. High quality factor nitride-based optical cavities: microdisks with embedded GaN/Al(Ga)N quantum dots. *Optics Letters*, 36(12):2203, jun 2011.
- [75] Tetsuya Kouno, Katsumi Kishino, and Masaru Sakai. Lasing action on whispering gallery mode of self-organized GaN hexagonal microdisk crystal fabricated by RF-plasma-assisted molecular beam epitaxy. *IEEE Journal of Quantum Electronics*, 47(12):1565–1570, dec 2011.
- [76] Christian Tessarek, Robert Röder, Tom Michalsky, Sebastian Geburt, Helena Franke, Rüdiger Schmidt-Grund, Martin Heilmann, Björn Hoffmann, Carsten Ronning, Marius Grundmann, and Silke Christiansen. Improving the optical properties of

- self-catalyzed GaN microrods toward whispering gallery mode lasing. *ACS Photonics*, 1(10):990–997, sep 2014.
- [77] Christian Tessarek, Martin Heilmann, and Silke Christiansen. Whispering gallery modes in GaN microdisks, microrods and nanorods grown by MOVPE. *physica status solidi (c)*, 11(3-4):794–797, jan 2014.
- [78] Kartik Srinivasan, Matthew Borselli, Thomas J. Johnson, Paul E. Barclay, Oskar Painter, Andreas Stintz, and Sanjay Krishna. Optical loss and lasing characteristics of high-quality-factor AlGaAs microdisk resonators with embedded quantum dots. *Applied Physics Letters*, 86(15):151106, apr 2005.
- [79] Z. Xie, S. Götzinger, W. Fang, H. Cao, and G. Solomon. Influence of a single quantum dot state on the characteristics of a microdisk laser. *Physical Review Letters*, 98(11), mar 2007.
- [80] Bei Shi, Si Zhu, Qiang Li, Yating Wan, Evelyn L. Hu, and Kei May Lau. Continuous-wave optically pumped 1.55 μm InAs/InAlGaAs quantum dot microdisk lasers epitaxially grown on silicon. *ACS Photonics*, 4(2):204–210, jan 2017.
- [81] Kartik Srinivasan, Matthew Borselli, Oskar Painter, Andreas Stintz, and Sanjay Krishna. Cavity Q , mode volume, and lasing threshold in small diameter AlGaAs microdisks with embedded quantum dots. *Optics Express*, 14(3):1094, 2006.
- [82] Natalia Kryzhanovskaya, Alexey Zhukov, Eduard Moiseev, and Mikhail Maximov. III-V microdisk/microring resonators and injection microlasers. *Journal of Physics D: Applied Physics*, 54(45):453001, aug 2021.
- [83] David Parrain, Christophe Baker, Guillaume Wang, Biswarup Guha, Eduardo Gil Santos, Aristide Lemaitre, Pascale Senellart, Giuseppe Leo, Sara Ducci, and Ivan Favero. Origin of optical losses in gallium arsenide disk whispering gallery resonators. *Optics Express*, 23(15):19656, jul 2015.
- [84] Hongxing Dong, Beier Zhou, Jingzhou Li, Jingxin Zhan, and Long Zhang. Ultraviolet lasing behavior in ZnO optical microcavities. *Journal of Materiomics*, 3(4):255–266, dec 2017.
- [85] M. Mehta and C. Meier. Controlled etching behavior of o-polar and zn-polar ZnO single crystals. *Journal of The Electrochemical Society*, 158(2):H119, 2011.
- [86] K. Nomenyo, A.-S. Gadallah, S. Kostcheev, D. J. Rogers, and G. Léron del. Enhanced stimulated emission in ZnO thin films using microdisk top-down structuring. *Applied Physics Letters*, 104(18):181104, may 2014.

- [87] X. Liu, W. Fang, Y. Huang, X. H. Wu, S. T. Ho, H. Cao, and R. P. H. Chang. Optically pumped ultraviolet microdisk laser on a silicon substrate. *Applied Physics Letters*, 84(14):2488–2490, apr 2004.
- [88] Christina A. Bader, Franziska Zeuner, Manuel H. W. Bader, Thomas Zentgraf, and Cedrik Meier. Nonlinear optical sub-bandgap excitation of ZnO-based photonic resonators. *Journal of Applied Physics*, 118(21):213105, dec 2015.
- [89] Marcel Ruth, Thomas Zentgraf, and Cedrik Meier. Blue-green emitting microdisks using low-temperature-grown ZnO on patterned silicon substrates. *Optics Express*, 21(21):25517, oct 2013.
- [90] Chunfeng Zhang, Fan Zhang, Xiao Wei Sun, Yi Yang, Jian Wang, and Jian Xu. Frequency-upconverted whispering-gallery-mode lasing in ZnO hexagonal nanodisks. *Optics Letters*, 34(21):3349, oct 2009.
- [91] Daniel J. Gargas, Michael C. Moore, Adrian Ni, Shu-Wei Chang, Zhaoyu Zhang, Shun-Lien Chuang, and Peidong Yang. Whispering gallery mode lasing from zinc oxide hexagonal nanodisks. *ACS Nano*, 4(6):3270–3276, apr 2010.
- [92] Rui Chen, Bo Ling, Xiao Wei Sun, and Han Dong Sun. Room temperature excitonic whispering gallery mode lasing from high-quality hexagonal ZnO microdisks. *Advanced Materials*, 23(19):2199–2204, apr 2011.
- [93] J. Dai, C. X. Xu, X. Y. Xu, J. T. Li, J. Y. Guo, and Y. Lin. Controllable fabrication and optical properties of Sn-doped ZnO hexagonal microdisk for whispering gallery mode microlaser. *APL Materials*, 1(3):032105, sep 2013.
- [94] Zuxin Chen, Xuechen Chen, Sheng Chu, and Rufang Peng. Ultraviolet to violet lasing from $\text{Cd}_x\text{Zn}_{(1-x)}\text{O}$ microdisks produced by chemical vapor deposition. *Optical Materials*, 72:459–463, oct 2017.
- [95] Jun Dai, Chunxiang Xu, Jitao Li, Yi Lin, Jiyuan Guo, and Gangyi Zhu. Photoluminescence and two-photon lasing of ZnO:Sn microdisks. *The Journal of Physical Chemistry C*, 118(26):14542–14547, jun 2014.
- [96] Weifeng Zhang and Jianping Yao. Silicon-based single-mode on-chip ultracompact microdisk resonators with standard silicon photonics foundry process. *Journal of Lightwave Technology*, 35(20):4418–4424, oct 2017.
- [97] Mohammad Soltani, Qing Li, Siva Yegnanarayanan, and Ali Adibi. Improvement of thermal properties of ultra-high Q silicon microdisk resonators. *Optics Express*, 15(25):17305, 2007.

- [98] D. E. Aspnes and A. A. Studna. Dielectric functions and optical parameters of si, ge, GaP, GaAs, GaSb, InP, InAs, and InSb from 1.5 to 6.0 eV. *Physical Review B*, 27(2):985–1009, jan 1983.
- [99] I. H. Malitson. Interspecimen comparison of the refractive index of fused silica. *Journal of the Optical Society of America*, 55(10):1205, oct 1965.
- [100] Paul E. Barclay, Kartik Srinivasan, Oskar Painter, Benjamin Lev, and Hideo Mabuchi. Integration of fiber-coupled high- Q SiN_x microdisks with atom chips. *Applied Physics Letters*, 89(13):131108, sep 2006.
- [101] Ehsan Shah Hosseini, Siva Yegnanarayanan, Amir H. Atabaki, Mohammad Soltani, and Ali Adibi. High quality planar silicon nitride microdisk resonators for integrated photonics in the visible wavelength range. *Optics Express*, 17(17):14543, aug 2009.
- [102] Bram De Geyter, Katarzyna Komorowska, Edouard Brainis, Philippe Emplit, Pieter Geiregat, Antti Hassinen, Zeger Hens, and Dries Van Thourhout. From fabrication to mode mapping in silicon nitride microdisks with embedded colloidal quantum dots. *Applied Physics Letters*, 101(16):161101, oct 2012.
- [103] Weiqiang Xie, Yunpeng Zhu, Tangi Aubert, Zeger Hens, Edouard Brainis, and Dries Van Thourhout. Fabrication and characterization of on-chip silicon nitride microdisk integrated with colloidal quantum dots. *Optics Express*, 24(2):A114, dec 2015.
- [104] Weiqiang Xie, Thilo Stöferle, Gabriele Rainò, Tangi Aubert, Suzanne Bisschop, Yunpeng Zhu, Rainer F. Mahrt, Pieter Geiregat, Edouard Brainis, Zeger Hens, and Dries Van Thourhout. On-chip integrated quantum-dot-silicon-nitride microdisk lasers. *Advanced Materials*, 29(16):1604866, feb 2017.
- [105] Hao-Che Chien, Chih-Yi Cheng, and Ming-Hua Mao. Continuous wave operation of SiO₂ sandwiched colloidal CdSe/ZnS quantum-dot microdisk lasers. *IEEE Journal of Selected Topics in Quantum Electronics*, 23(5):1–5, sep 2017.
- [106] B. Gayral, J. M. Gérard, A. Lemaître, C. Dupuis, L. Manin, and J. L. Pelouard. High- Q wet-etched GaAs microdisks containing InAs quantum boxes. *Applied Physics Letters*, 75(13):1908–1910, sep 1999.
- [107] Biswarup Guha, Felix Marsault, Fabian Cadiz, Laurence Morgenroth, Vladimir Ulin, Vladimir Berkovitz, Aristide Lemaître, Carmen Gomez, Alberto Amo, Sylvain Combrié, Bruno Gérard, Giuseppe Leo, and Ivan Favero. Surface-enhanced gallium arsenide photonic resonator with quality factor of $6 \cdot 10^6$. *Optica*, 4(2):218, feb 2017.

-
- [108] Jan Wiersig and Martina Hentschel. Unidirectional light emission from high- Q modes in optical microcavities. *Physical Review A*, 73(3), mar 2006.
- [109] Bing-Jing Li and Pao-Lo Liu. Numerical analysis of microdisk lasers with rough boundaries. *IEEE Journal of Quantum Electronics*, 33(5):791–795, may 1997.
- [110] Qing Li, Ali A. Eftekhar, Zhixuan Xia, and Ali Adibi. Azimuthal-order variations of surface-roughness-induced mode splitting and scattering loss in high- Q microdisk resonators. *Optics Letters*, 37(9):1586, may 2012.
- [111] Svetlana V. Boriskina, Trevor M. Benson, Phillip Sewell, and Alexander I. Nosich. Spectral shift and Q change of circular and square-shaped optical microcavity modes due to periodic sidewall surface roughness. *Journal of the Optical Society of America B - Optical Physics*, 21(10):1792, oct 2004.
- [112] K.D. Choquette, K.M. Geib, C.I.H. Ashby, R.D. Twisten, O. Blum, H.Q. Hou, D.M. Follstaedt, B.E. Hammons, D. Mathes, and R. Hull. Advances in selective wet oxidation of AlGaAs alloys. *IEEE Journal of Selected Topics in Quantum Electronics*, 3(3):916–926, jun 1997.
- [113] Ge Yuan, Cheng Zhang, Kanglin Xiong, and Jung Han. InGaN/GaN microdisks enabled by nanoporous GaN cladding. *Optics Letters*, 43(22):5567, nov 2018.
- [114] A. Strittmatter, A. Schliwa, J.-H. Schulze, T. D. Germann, A. Dreismann, O. Hitze-
mann, E. Stock, I. A. Ostapenko, S. Rodt, W. Unrau, U. W. Pohl, A. Hoffmann,
D. Bimberg, and V. Haisler. Lateral positioning of InGaAs quantum dots using a
buried stressor. *Applied Physics Letters*, 100(9):093111, feb 2012.
- [115] E. V. Lutsenko, G. P. Yablonskii, V. N. Pavlovskii, V. Z. Zubialevich, A. L. Gurskii,
H. Kalisch, K. Heime, R. H. Jansen, T. Walther, B. Schineller, and M. Heuken.
Influence of pumping and inherent laser light on properties and degradation of
ZnMgSSe/ZnSe quantum well heterostructures. *physica status solidi (a)*, 195(1):188–
193, jan 2003.
- [116] U. T. Schwarz, E. Sturm, W. Wegscheider, V. Kümmler, A. Lell, and V. Härle.
Optical gain, carrier-induced phase shift, and linewidth enhancement factor in InGaN
quantum well lasers. *Applied Physics Letters*, 83(20):4095–4097, nov 2003.
- [117] A. I. Rahachou and I. V. Zozoulenko. Effects of boundary roughness on a Q factor
of whispering-gallery-mode lasing microdisk cavities. *Journal of Applied Physics*,
94(12):7929, 2003.
- [118] R. E. Slusher, A. F. J. Levi, U. Mohideen, S. L. McCall, S. J. Pearton, and R. A.
-

- Logan. Threshold characteristics of semiconductor microdisk lasers. *Applied Physics Letters*, 63(10):1310–1312, sep 1993.
- [119] K. Solis-Trapala, R.W. Smink, J. Molina-Vazquez, B.P. de Hon, A.G. Tjihuis, and H.J.S. Dorren. Quasi-three-dimensional frequency-domain modeling to study size limitations of quantum-dot microdisk lasers. *Optics Communications*, 283(20):4046–4053, oct 2010.
- [120] C. Tessarek, G. Sarau, M. Kiometzis, and S. Christiansen. High quality factor whispering gallery modes from self-assembled hexagonal GaN rods grown by metal-organic vapor phase epitaxy. *Optics Express*, 21(3):2733, jan 2013.
- [121] Matthias Klude. Znse-based laser diodes with quaternary cdznsse quantum wells as active region: - chances and limitations, 2002.
- [122] Ian Rousseau, Gordon Callsen, Gwénolé Jacopin, Jean-François Carlin, Raphaël Butté, and Nicolas Grandjean. Optical absorption and oxygen passivation of surface states in III-nitride photonic devices. *Journal of Applied Physics*, 123(11):113103, mar 2018.
- [123] Irving H. Malitson. Refraction and dispersion of synthetic sapphire. *Journal of the Optical Society of America*, 52(12):1377, dec 1962.
- [124] M. D. Groner, F. H. Fabreguette, J. W. Elam, and S. M. George. Low-temperature Al_2O_3 atomic layer deposition. *Chemistry of Materials*, 16(4):639–645, jan 2004.
- [125] M.C. Tamargo, M.J.S.P. Brasil, R.E. Nahory, R.J. Martin, A.L. Weaver, and H.L. Gilchrist. MBE growth of the (Zn,Cd)(Se,Te) system for wide-bandgap heterostructure lasers. *Semiconductor Science and Technology*, 6(9A):A8–A13, sep 1991.
- [126] M. Schulz O. Madelung, U. Rössler. Zinc selenide (ZnSe) phonon energies. In *Landolt-Börnstein - Group III Condensed Matter 41B (II-VI and I-VII Compounds; Semimagnetic Compounds)*, pages 1–8. Springer-Verlag, 1999.
- [127] L. Malikova, Wojciech Krystek, Fred H. Pollak, N. Dai, A. Cavus, and M. C. Tamargo. Temperature dependence of the direct gaps of ZnSe and $\text{Zn}_{0.56}\text{Cd}_{0.44}\text{Se}$. *Physical Review B*, 54(3):1819–1824, jul 1996.
- [128] Sumin Choi, Cuong Ton-That, Matthew R. Phillips, and Igor Aharonovich. Observation of whispering gallery modes from hexagonal ZnO microdisks using cathodoluminescence spectroscopy. *Applied Physics Letters*, 103(17):171102, oct 2013.
- [129] J. T. Ku, M. C. Kuo, J. L. Shen, K. C. Chiu, T. H. Yang, G. L. Luo, C. Y. Chang, Y. C. Lin, C. P. Fu, D. S. Chuu, C. H. Chia, and W. C. Chou. Op-

tical characterization of ZnSe epilayers and ZnCdSe/ZnSe quantum wells grown on Ge/Ge_{0.95}Si_{0.05}/Ge_{0.9}Si_{0.1}/Si virtual substrates. *Journal of Applied Physics*, 99(6):063506, mar 2006.

B. List of Publications

Publications in Peer-Reviewed Journals

- [I] W. Seemann, A. Kothe, C. Tessarek, G. Schmidt, S. Qiao, N. von den Driesch, J. Wiersig, A. Pawlis, G. Callsen, J. Gutowski: **Free-Standing ZnSe-Based Microdisk Resonators: Influence of Edge Roughness on the Optical Quality and Reducing Degradation with Supported Geometry.** *physica status solidi B* 258 (2021), 2100249.

Contributions to Conferences

- [C1] W. Seemann, A. Kothe, C. Tessarek, G. Schmidt, S. Qiao, N. von den Driesch, J. Wiersig, A. Pawlis, G. Callsen, J. Gutowski: **Free-Standing ZnSe-Based Microdisk Resonators: Influence of Edge Roughness on the Optical Quality and Reducing Degradation with Supported Geometry.** *virtual DPG Spring Meeting*, talk (2021).
- [C2] W. Seemann, A. Kothe, G. Schmidt, J. Wiersig, A. Pawlis, J. Gutowski: **Influence of edge roughness on the optical properties of ZnSe-based microdisks.** *International Conference on the Physics of Light-Matter Coupling in Nanostructures*, poster (2020).
- [C3] W. Seemann, A. Kothe, G. Schmidt, A. Pawlis, J. Gutowski: **Optical properties of ZnSe-based microdisks.** *International School on Nanophotonics, Metamaterials and Photovoltaics*, poster (2019).
- [C4] W. Seemann, A. Kothe, G. Schmidt, A. Pawlis, J. Gutowski: **Optical properties of ZnSe-based microdisks.** *DPG Spring Meeting*, talk (2019).
- [C5] S. Bley, A. Castro-Carranza, E. Tansey, W. Seemann, J. Gutowski: **Impact of a polystyrene-based passivating interlayer on hybrid polymer/ZnO nanowire heterojunctions.** *33rd International Conference on the Physics of Semiconductors*, talk (2017).

Seminar and Other Talks

- [S1] W. Seemann, A. Kothe, C. Tessarek, G. Schmidt, S. Qiao, N. von den Driesch, J. Wiersig, A. Pawlis, G. Callsen, J. Gutowski: **Free-Standing ZnSe-Based Microdisk Resonators: Influence of Edge Roughness on the Optical Quality and Reducing Degradation with Supported Geometry.** *Seminar of the Institute of Solid State Physics, University of Bremen* (2021).
- [S2] W. Seemann, A. Kothe, G. Schmidt, J. Wiersig, A. Pawlis, J. Gutowski: **Optical properties of ZnSe-based microdisk resonators.** *Forschungsseminar: Aktuelle Fragen der Festkörperphysik und Optik, University of Magdeburg* (2020).
- [S3] W. Seemann, A. Kothe, G. Schmidt, A. Pawlis, J. Gutowski: **Optical properties of ZnSe-based microdisks.** *Solid State Physics Seminar, University of Bremen* (2019).
- [S4] W. Seemann, A. Kothe, G. Schmidt, A. Pawlis, J. Gutowski: **Optical properties of ZnSe-based microdisks.** *MAPEX Symposium* (2019).

C. Acknowledgements

This thesis, and all the work that it represents, would not have been possible without the various contributions of many people. Here, I want to attempt to express my gratitude towards all of them:

First off all, I want to thank professor Jürgen Gutowski for the opportunity to work on this topic in his group. During my time as PhD student he gave me enough space to develop and test my own ideas, but his guidance through many discussions significantly improved my work.

PD Dr. Alexander Pawlis from the Forschungszentrum Jülich not only provided the microdisk resonators that I analyzed and was always available if I had questions regarding them. He additionally agreed to review my thesis, I am very thankful for that.

I also would like to thank professor Jan Wiersig from the University of Magdeburg whose name I mentioned a few times already, because his theoretical calculations of resonances in deformed microdisks greatly contributed to my work. With him too I had some interesting discussions about the experimental and theoretical results presented in this work.

Christian Tessarek, from the working group of professor Martin Eickhoff, deserves thanks for his support in the optical characterization of supported microdisks.

Professor Frank Jahnke and professor Annette Ladstätter-Weißenmayer as well as Oleg Gridenco and Genrietta Steingelb kindly agreed to let me suggest them as part of the examining committee in my thesis defense. I am thankful for that.

Special thanks to professor Gordon Callsen, who acted as my supervisor in the final stages of this work. I am looking forward to continuing my career in his group, together with Mahmoud Elhajhasan and Isabell Hüllen, all of whom have already become great colleagues over a short period of time.

Regarding great colleagues, professor Kathrin Sebald, Dr. Alexander Kothe and Oleg Gridenco definitely deserve a mention in that category. They helped me numerous times in the last three years when we worked together in the lab, discussed results, or just had a relaxed conversation in the lunch break.

Many of the results I present in this work would have been at least a lot harder to obtain if it weren't for Daniel Vaske. I am sure he holds his position as 'technician' of the group only because 'guy who keeps all the equipment running' would sound less professional on the website.

On a similar note, I want to thank Annegret Ebert, who knows the answer to just about any question regarding administrative processes at the University of Bremen and was

always a great help.

Last, but most certainly not least, I want to thank my family. This includes my parents, who helped me develop into the person I am today, as well as my fiancée, as without her continued support this thesis would be significantly shorter at the time of writing these lines.

To everybody I mentioned in this paragraphs, but also everybody I forgot:

Thank you!

D. Curriculum Vitae

Personal Information

Date of Birth: 28th August 1995
Place of Birth: Walsrode

Professional Experience and Education

since 07/2018	PhD Student Institute of Solid State Physics Semiconductor Optics Group University of Bremen
10/2015 - 06/2018	Master's degree in Physics University of Bremen
10/2013 - 09/2015	Bachelor's degree in Physics University of Bremen
08/2005 - 05/2013	Gymnasium Albert-Schweitzer-Schule Nienburg/Weser
08/2001 - 07/2005	Primary School Grundschule Heemsen